2010-07-13

Influence of Material and Geometric Parameters on the Flow-Induced Vibration of Vocal Folds Models

Brian A. Pickup
Brigham Young University - Provo

Influence of Material and Geometric Parameters on the Flow-Induced Vibration of Vocal Fold Models

Brian A. Pickup

A thesis submitted to the faculty of
Brigham Young University
in partial fulfillment of the requirements for the degree of

Master of Science

Scott L. Thomson, Chair
Steven E. Gorrell
Julie C. Vanderhoff

Department of Mechanical Engineering

Brigham Young University

August 2010

ABSTRACT

Influence of Material and Geometric Parameters

on the Flow-Induced Vibration of

Vocal Fold Models

Brian A. Pickup

Department of Mechanical Engineering

Master of Science

The vocal folds are an essential component of human speech production and communication. Advancements in voice research allow for improved voice disorder treatments. Since *in vivo* analysis of vocal fold function is limited, models have been developed to simulate vocal fold motion. In this research, synthetic and computational vocal fold models were used to investigate various aspects of vocal fold vibratory characteristics. A series of tests were performed to quantify the effect of varying material and geometric parameters on the models' flow-induced responses. First, the influence of asymmetric vocal fold stiffness on voice production was evaluated using life-sized, self-oscillating vocal fold models with idealized vocal fold geometry. Asymmetry significantly influenced glottal jet flow, glottal area, and vibration frequency. Second, flow-induced responses of simplified and MRI-based synthetic models were compared. The MRI-based models showed remarkable improvements, including less vertical motion, alternating convergent-divergent glottal profile patterns, and mucosal wave-like movement. Third, a simplified model was parametrically investigated via computational modeling techniques to determine which geometric features influenced model motion. This parametric study led to identification and ranking of key geometric parameters based on their effects on various measures of vocal fold motion (e.g., mucosal wave-like movement). Incorporation of the results of these studies into the definition of future models could lead to models with more life-like motion.

Keywords: vocal folds, vocal fold modeling, asymmetry, mucosal wave, high-speed imaging, particle image velocimetry, PIV, MRI, parameterization, videokymography, VKG, Brian A. Pickup

ACKNOWLEDGMENTS

I originally came to BYU as an undergraduate with intentions of gaining a degree in mechanical engineering and becoming a heart surgeon. Fortunately while taking an instrumentation course, I was exposed to voice research by my professor, Dr. Scott Thomson, and soon thereafter began working with him and the vocal fold modeling research group. Subsequent experiences with voice research opened my eyes to the power of applying mechanical engineering fundamentals toward biomedical problems, and I quickly decided to forego medical school and pursue a masters degree in engineering.

Over the past 4 years I have attempted to absorb the intellect and wisdom that Dr. Thomson has provided as a mentor and friend, enabling me to become successful at voice research; to a large degree, it is thanks to Dr. Thomson that this work was presented at various conferences, culminating in the publishing of 2 major articles, with 1 in review, in vocal fold research journals, and the compilation of this thesis. My academic accomplishments were made possible in great degree thanks to his hard work, patience, and criticisms, of which I will ever be grateful. His assistance in writing this thesis is also gratefully acknowledged. Most importantly, however, has been his guidance and testimony that have taught me that there are more important things in life than research.

I would like to express deep gratitude to the BYU Mechanical Engineering Department and the National Institute on Deafness and Other Communicative Disorders for providing funding and allowing me to focus on my research full-time.

I would also like to acknowledge the assistance of Dr. Steve Gorrell and Dr. Julie Vanderhoff, both of whom assisted in editing the content of this thesis.

I am indebted to the assistance of the many who worked with me in the vocal fold modeling research group. Their knowledge, camaraderie, and friendship made working a joy. The assistance of Paul Gollnick in fabricating physical models, Jesse Daily in verifying the computational model, and Simeon Smith in post-processing computational model data is gratefully acknowledged.

I am very grateful to my Father in Heaven who blessed me the guidance and peace that only He can offer. My testimony of His existence has grown considerably over the past 2 years.

Finally, I dedicate this work to my wife, Samantha, and our son, Simon, who have never ceased to provide support and love throughout this entire experience. Their love sustains me.

TABLE OF CONTENTS

LIST OF TABLES

LIST OF FIGURES

CHAPTER 1. INTRODUCTION

For most people, the voice plays an integral role in affecting their quality of life. In particular, several careers critically depend on the ability to use one's voice (i.e., singers, actors, coaches, teachers, etc.) Unfortunately, according to the National Institute on Deafness and other Communication Disorders (NIDCD), millions of Americans suffer from voice disorders [1]. Diseased or damaged vocal folds can have a life-long adverse effect on an individual's voice. While treatments are good relative to the complexity of the voice production system, they are nonetheless limited in part by the underlying physics as well as the complex system itself. In order to help advance the state-of-the-art in voice disorder treatment, engineering principles are applied to increase knowledge of voice production characteristics with the overall goal of improving prevention, diagnosis, and surgical and other clinical interventions, thereby improving the quality of life for individuals who suffer from voice disorders. In particular, this thesis aims to advance the knowledge of voice production through an investigation of material and geometric properties commonly used to define vocal fold models.

1.1 Background and motivation

1.1.1 Anatomy

A basic overview of the relevant anatomical features within the vocal tract is given. An illustration of the larynx and vocal tract is provided in Fig. 1.1. The larynx connects the lungs

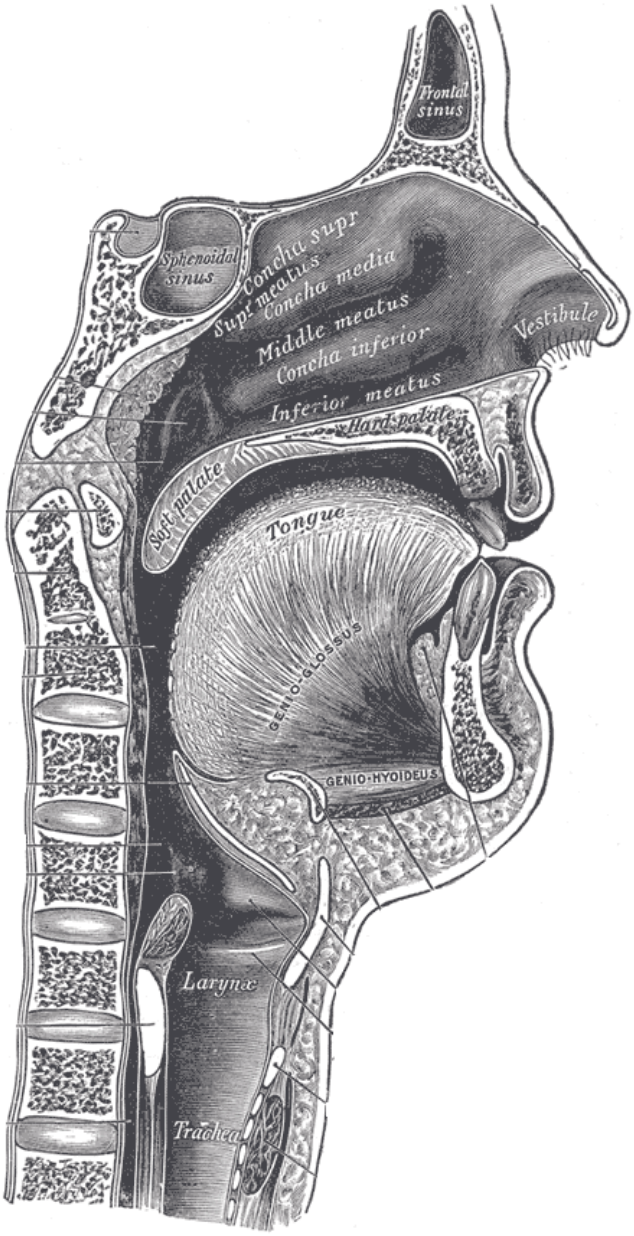

Figure 1.1: Sagittal cross-section depicting the larynx anatomy (adapted from Gray's *Anatomy of the Human Body*, images public domain, www.bartleby.com).

and vocal tract and is situated in the anterior portion of the neck, in front of the esophagus. The vocal folds are situated within the larynx, behind the laryngeal prominence of the thyroid cartilage (commonly referred to as the Adam's apple). The air passage between the vocal folds is referred to as the glottis (see Fig. 1.2). Voice production begins with the vocal folds being drawn close

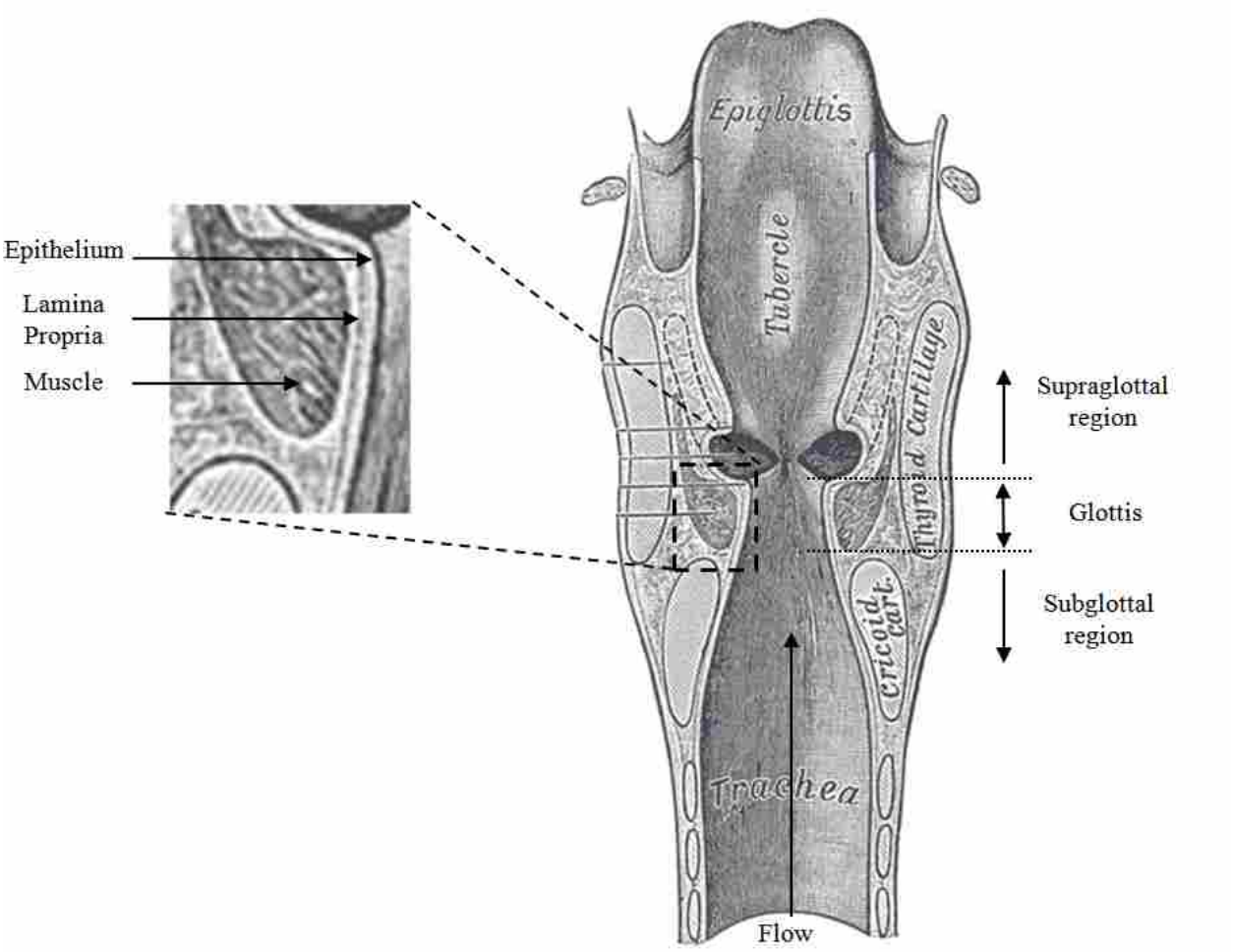

Figure 1.2: Coronal cross-section of the human larynx. Vocal fold layers (left) and glottal, supraglottal, and subglottal areas (right) are denoted (adapted from Gray's *Anatomy of the Human Body*, images public domain, www.bartleby.com).

together. Air pressure from the lungs builds, the vocal folds are forced open and air passes through the glottis. When the lung pressure reaches a sufficiently high value (termed onset pressure) the vocal folds undergo self-sustained oscillations. These oscillations will generally continue until the pressure is decreased to the point where the folds cease vibrating (termed offset pressure). These oscillations cause pressure differences inside the larynx which propagate up through the vocal tract and out of the mouth, producing sound.

The vocal folds are comprised of several tissue layers (see Fig. 1.2). The muscle layer (thyrovocalis muscle) is the deepest and largest layer. The muscle fibers are activated during speech to adjust the tension of the folds and to some extent, the pitch of sound produced. The lamina propria layer surrounds the muscle layer and is comprised of three portions, each differing only slightly in material property and thickness. The most superficial layer of the vocal folds is the epithelium, which is a thin, stratified squamous cell layer that aids in protecting the vocal folds during vibration.

1.1.2 Previous voice research

Through research, a better understanding of voice production mechanics is possible. Areas of research interest include aerodynamic energy transfer, asymmetric vibration, glottal jet flow, intraglottal pressure distributions, mucosal wave quantification, laryngeal geometric definitions, airway surface layer adhesion, tissue properties, abnormal movement, and acoustics. Ideally, researchers and clinicians would acquire measurements *in vivo* (situated inside the body). While this is possible for views from a superior perspective, complete laryngeal exploration is not feasible due to the embedded position of the vocal folds. Models for analyzing flow and tissue dynamical characteristics have thus been developed that simulate conditions inside the larynx. These models can be divided into three main groups: excised larynges, computational models, and physical models. All of these models aid in overcoming limitations of *in vivo* measurements, but a perfect replication of the larynx has yet to be achieved. The following is a brief overview of some of these models. More in-depth discussions of previous work are provided in Chapters 2 through 4.

Excised larynges

Excised larynges - human, canine, and other mammalian - have been used to simulate airflow through the larynx and vocal fold vibration. Excised larynges are geometrically accurate; this is important because geometry plays an integral role in governing vocal fold vibration. Since the larynx is somewhat symmetric, a hemilarynx (or half-larynx) can be used together with transparent materials (e.g., Plexiglas) to allow for visualization of glottal and subglottal surfaces, which is otherwise not possible via *in vivo* methods or full excised larynx modeling. Hence, flow velocities and vocal fold position throughout vibration of actual human vocal folds can be quantified [2, 3]. However, excised larynges are somewhat difficult to procure, and are difficult to work with since the tissues dehydrate quickly and undergo other changes. They also are very limited in terms of parametric studies involving geometric and material property changes.

Computational models

There are several types of computational vocal fold models used in voice research (e.g., finite-element, continuum-based, high fidelity, etc.) [4–8] These models can yield data regarding pressure, modal analysis, vibratory movement, acoustics, and other flow and solid characteristics. Current models incorporate the fluid-structure coupling of the air and vocal fold tissue that is essential for voice production. Two-dimensional and three-dimensional models have been developed [9, 10]. Much has been discovered using computational models, such as the sensitivity of model motion to geometric and material parameters [8, 11], as well as other vocal fold vibration characteristics (e.g., onset frequency and threshold pressure [12]).

Physical models

Physical modeling of the vocal folds can be further divided into two groups: static (rigid) and self-oscillating.

Static models are used to examine flow characteristics in stationary vocal fold models. Most commonly, these are used to study intraglottal pressure distributions and flow profiles [13, 14]. These models are a convenient way of studying flow separation downstream of the glottis. Although these models provide control over geometric definitions, they do not self-oscillate and thus lack the coupled fluid-solid dynamics that are central to vocal fold vibration.

Self-oscillating models are used to capture life-like movement of the vocal folds. Titze et al. [15] developed a simple stainless steel "body" model (representing the muscle layer of the vocal folds) with a surrounding silicone "cover" membrane and fluid (representing the lamina propria and epithelial layers of the vocal folds) to study phonation threshold pressure (i.e., onset pressure). This model has been used to study the effect of various material and geometric parameters on flow characteristics, such as the effect of cover membrane thickness and various biomaterials on onset pressure [16, 17]. However, this model was limited in its movement due to the stiff body layer; hence, only oscillations of the cover layer could be generated.

Recently, self-oscillating models were developed that incorporated body layer movement via models fabricated from three-part silicone [7, 18]. A cover layer was added to this model to provide even more realistic movement [19, 20]. These models provide an essential characteristic in vocal fold movement in that the fluid-structure interaction is manifest, and higher amplitude oscillations are captured. Recently, researchers have used variations of this model to study the effect of subglottal acoustics [21], explore aerodynamically and acoustically driven modes of vibration [22],

investigate flow structures immediately downstream of the glottal exit [23], and study the effect of supraglottal structures on jet flow characteristics [20].

1.1.3 Motivation

Even with the progress that has been made with regards to voice modeling, much has yet to be understood. This is in part due to limitations of synthetic vocal fold models, but also because these models have yet to be fully studied. Specifically, while material and geometric parameters of the models are central to their flow-induced vibratory characteristics, the degree of influence that these parameters have on model motion characteristics has yet to be quantified. It is the goal of this research to provide a better understanding of how material and geometric properties of the vocal folds affect vibratory and flow characteristics. It is anticipated that the results from this research will provide a greater understanding of voice production, which eventually may lead to improved quality of life for people who suffer from voice disabilities.

1.2 Thesis overview

This work attempts to further expand the knowledge of voice production by incorporating material and geometric variations to the model introduced by Thomson et al. [7] using both experimental and computational modeling techniques. All of the models used in this work were two-layered, which represented two of the primary layers of the vocal folds: the lamina propria (cover) and the muscle (body). This is shown in Fig. 1.3, along with an illustration of the test setup. Further details of the experimental setup, model fabrication methods, and computer models are provided in subsequent chapters.

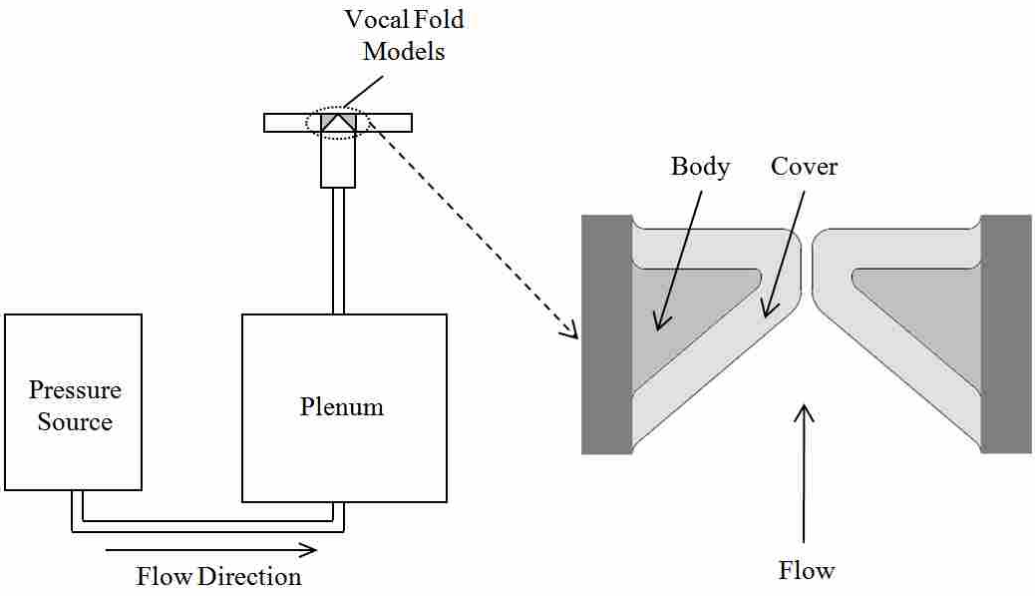

Figure 1.3: Test setup (left) and geometrically idealized two-layer vocal fold model (right).

1.3 Thesis outline

This work is divided into three main areas:

1) The change in synthetic model response due to material asymmetries (Chapter 2).

2) The dynamic response of synthetic models with idealized vs. magnetic resonance imaging (MRI)-based geometry (Chapter 3).

3) A parametric investigation of the influence of vocal fold model geometry using computational models (Chapter 4).

1.3.1 Influence of asymmetric stiffness on synthetic vocal fold model vibration (Chapter 2)

One of the purposes of this thesis was to investigate the influence of asymmetric material properties on vocal fold dynamics. Numerous studies have used computational and synthetic vocal folds to investigate vocal fold vibration and glottal airflow for both healthy and diseased vocal fold

scenarios, specifically aiming to explore asymmetric characteristics [9, 14, 23–25]. Lacking has been a controlled study of the influence of material-only asymmetry on vocal fold vibration and glottal aerodynamics. In this research, synthetic models were fabricated, and varying degrees of left-right material asymmetry were incorporated. Aspects of vocal fold vibration were quantified by measuring frequency, left-right vocal fold phase-shift, onset pressure, and glottal jet flow.

1.3.2 Idealized vs. MRI-based synthetic vocal fold models (Chapter 3)

Synthetic and computational vocal fold models used by researchers have typically been defined using simplified geometries, which have proven to exhibit some life-like characteristics of human vocal folds [21, 23, 26]. These simplified models have made it possible to parametrically investigate model motion without using expensive and highly sensitive models (i.e., excised larynges). More life-like motion of synthetic vocal fold models may be achieved if a more geometrically accurate model is utilized in experimentation. In order to determine whether this is feasible, models based on magnetic resonance imaging (MRI) data were fabricated and their responses were compared with those of geometrically idealized models.

1.3.3 Influence of geometric features on vocal fold model vibration (Chapter 4)

As mentioned above, many researchers have used simplified models to simulate vocal fold flow-induced vibration. It is known that geometry significantly impacts how vocal fold models vibrate; what is not known, however, is the impact that specific geometric features have on model motion. This work identifies which geometric features of a computational vocal fold model play significant roles in governing its movement. The model was geometrically parameterized, and a screening-type design-of-experiments approach was used to identify the relative effects of 13 geo-

metric parameters. Five separate measurements were assessed in order to estimate the magnitude of the effect each geometric parameter had on vibratory motion, including flow-induced vibration frequency, changes in glottal width, flow rate, and intraglottal angle, and intraglottal phase delay. Identifying key geometric parameters may lead to improved (yet still simplified) computational and physical models of the vocal folds that better exhibit true vocal fold vibratory characteristics.

CHAPTER 2. INFLUENCE OF ASYMMETRIC STIFFNESS ON SYNTHETIC VOCAL FOLD MODEL VIBRATION [1]

The influence of asymmetric vocal fold stiffness on voice production was evaluated using life-sized, self-oscillating vocal fold models with an idealized geometry based on the human vocal folds. The models were fabricated using flexible, materially-linear silicone compounds with Young's modulus values comparable to that of vocal fold tissue. The models included a two-layer design to simulate the vocal fold layered structure. The respective Young's moduli of elasticity of the "left" and "right" vocal fold models were varied to create asymmetric conditions. High-speed videokymography was used to measure maximum vocal fold excursion, vibration frequency, and left-right phase shift, all of which were significantly influenced by asymmetry. Onset pressure, a measure of vocal effort, increased with asymmetry. Particle image velocimetry (PIV) analysis showed significantly greater skewing of the glottal jet in the direction of the stiffer vocal fold model. Potential applications to various clinical conditions are mentioned, and suggestions for future related studies are presented.

2.1 Introduction of asymmetric modeling

Healthy human vocal folds experience flow-induced vibrations in response to tracheal airflow. These vibrations modulate glottal airflow, thus creating pressure fluctuations within the vocal tract that generate sound for voice production. The vocal folds exhibit natural asymmetry [27],

[1] This chapter is based on Pickup, B.A., Thomson, S.L. (2009). "Influence of asymmetric stiffness on the structural and aerodynamic response of synthetic vocal fold models," Journal of Biomechanics 42: 2219-2225.

but this is generally asymptomatic. However, voice disorders such as vocal fold scarring [28], inflammation (e.g., due to reflux or laryngitis [29]), and sulcus vocalis [30] may exhibit sufficient asymmetry so as to contribute to noticeably irregular vocal fold vibration. Voice quality, and consequently quality of life, is adversely affected. The research described in this chapter is aimed at studying asymmetric material properties in vocal fold vibration in order to assist in the continued development of improved clinical care of the human voice.

Studies using computational and synthetic vocal folds have been used to investigate vocal fold vibration and glottal airflow for both healthy and diseased vocal fold scenarios. The following summarizes a few studies that have focused on structural and/or aerodynamic asymmetry.

Zhang and Jiang [24] demonstrated that the addition of a unilateral mass (polyp) added to the commonly-used two-mass vocal fold model [9] would adversely affect vocal fold vibratory characteristics, and concluded that other conditions that result in added mass to the vocal folds (e.g., nodules) may produce abnormal vocal fold movements. Using a synthetic rubber vocal fold model to investigate irregular vocal fold vibration, Berry et al. [31] showed two types of biphonation, one related to asymmetries found between vocal folds (left-right asymmetry), and the other within vocal folds (anterior-posterior asymmetry). The benefit of using synthetic vocal fold models to study asymmetric vibration patterns was emphasized. They recommended further studies into mechanisms of irregular vocal fold vibration across many phonatory conditions involving both symmetric and asymmetric vocal folds using multilayered synthetic vocal fold models.

Regarding glottal jet aerodynamics, Shinwari et al. [14] used flow visualization to characterize the flow through rigid acrylic vocal fold models with varying degrees of intraglottal asymmetry, and discussed ways in which aerodynamic driving forces could differ between symmetric and asymmetric vocal folds. Khosla et al. [25] recently used particle image velocimetry (PIV) to

investigate the supraglottal flow in excised canine larynges (both normal and asymmetric). They found that asymmetric stiffness between vocal folds resulted in lateral jet skewing, asymmetric glottal areas, and periodic asymmetric mucosal waves. Drechsel and Thomson [20] demonstrated sensitivity of the glottal jet to the lateral position of supraglottal structures (such as a vocal tract and/or false vocal folds) using a synthetic, self-oscillating vocal fold model. Neubauer et al. [23] showed that slight unevenness in the mounting of otherwise nominally symmetric self-oscillating synthetic models could produce a laterally-skewed jet.

These studies have focused on asymmetry resulting largely from geometric factors. Lacking is a controlled study of the influence of material-only asymmetry on vocal fold vibration and glottal aerodynamics. It is anticipated that through further studies of geometric and material asymmetry, improved phonosurgical procedures will lead to improved voice preservation and/or restoration. The purpose of this research was to investigate the influence of asymmetric material properties on vocal fold dynamics. This was done using high-speed videokymography and particle image velocimetry (PIV) in conjunction with multi-layer synthetic vocal fold models that included varying degrees of stiffness asymmetry.

2.2 Methods

2.2.1 Synthetic vocal fold model fabrication

Synthetic, one-layer (homogeneous), self-oscillating, continuum vocal fold models have been the subject of several recent studies (e.g., [7, 21–23, 31]). To reflect the soft cover layer and stiff body layer composition of the human vocal folds [32], two-layer versions of these synthetic models have recently been used [20, 33]; see Fig. 2.1), with geometries based on that of Scherer et al. [13]. These models are of the same size, similar shape, and similar flexibility as the hu-

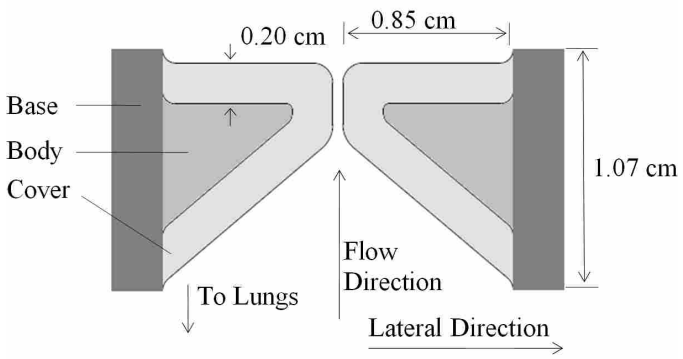

Figure 2.1: Diagram of vocal fold model dimensions.

man vocal folds. Simplifications associated with these models have included idealized geometries with uniform anterior-posterior cross sections, exclusion of physiological mechanisms (e.g., blood flow, cell response, etc.), as well as elastic, materially-linear, isotropic material properties (in contrast with the viscoelastic, materially-nonlinear, anisotropic properties of human vocal fold tissue). Nevertheless, the models have been shown to vibrate at pressures and frequencies typical of human phonation. Further, they allow for prolonged testing and parametric studies not feasible with excised larynges, and are based on relatively simple and inexpensive manufacturing methods.

The models for the present research were fabricated using a three-component addition-cure silicone compound, consisting of two-part Ecoflex 0030® silicone rubber and single-part Silicone Thinner® (Smooth-On, Inc.) Variation in stiffness between vocal fold models was achieved by using varying amounts of thinner (more thinner reduces the modulus of elasticity of the cured material). Symmetric and asymmetric models were fabricated and tested. Table 2.1 lists Young's modulus values for the body and cover layers of the different models. The notation $L_{BC}R_{BC}$ is used as follows. L and R denote the position of the vocal fold models from the anterior perspective (left and right, respectively). B and C represent the volume ratio of silicone thinner for the body and cover layers, respectively; for example, a value of B = 2 corresponds to a 1:1:2 mixing ratio,

or one part of each Ecoflex compound to two parts Silicone Thinner. For a baseline measure, a model representing a healthy vocal fold was kept on the left side (L_{24}) during the experiments for both asymmetric and symmetric cases, and only the right vocal fold model was changed.

Table 2.1: Young's modulus of elasticity (kPa) of vocal fold models.

Case	Left cover	Right cover	Left body	Right body
$L_{24}R_{24}$	3.3	2.9	8.9	8.6
$L_{24}R_{23}$	3.3	5.2	8.9	9.0
$L_{24}R_{22}$	3.3	8.7	8.9	8.8

The cover layer thickness for each model was approximately 2 mm. The models were attached to acrylic plates using a silicone rubber adhesive as previously described [19]. An approximately 3 mm base at the lateral edge of each vocal fold model was used to position the model laterally. The base was made of two-part silicone compound DragonSkin™ (also by Smooth-On, Inc.); it was much stiffer than the other vocal fold model material, and thus did not vibrate significantly during model oscillation.

2.2.2 Test setup

The test setup is shown in Fig. 2.2. An approximately 4.0 m long, 0.95 cm diameter flexible PVC tube connected a compressed air supply to a rigid plenum. Air flow was regulated via a manual valve and monitored using an in-line rotameter (only in place during onset pressure measurements) and a differential pressure transducer (Omega PX138-001D5V). Upstream of the plenum was a LaVision aerosol generator (not shown) used to create seed particles from DEHS oil (di-ethyl-hexyl sebacate, CAS#122-62-3) for PIV data collection. The section immediately upstream of the vocal folds ("trachea") was a 1.27 cm diameter, 7.6 cm long rigid PVC pipe

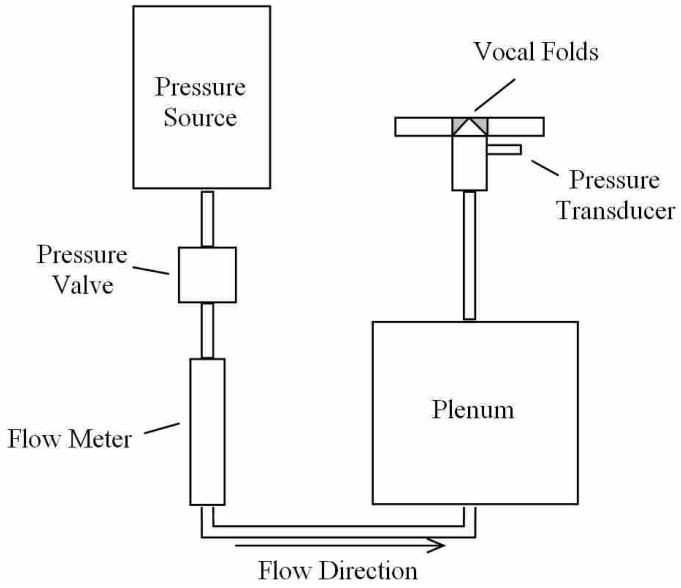

Figure 2.2: Synthetic vocal fold model setup.

mounted to the plates holding the synthetic vocal fold models. A 1.27 cm diameter, 30 cm long flexible PVC tube connected the subglottal area to the plenum. As is commonly the case with excised larynx studies, no downstream test section ("vocal tract") was used.

2.2.3 Data acquisition

A National Instruments data acquisition system (PXI-1042Q) with LabVIEW software was used to collect frequency data obtained from the pressure transducer. The PIV system was used to acquire two-dimensional velocity data of the supraglottal jet in what would be the equivalent of a coronal cross section at the approximate anterior-posterior midplane of the vocal fold models. The PIV camera (LaVision VC-Imager Intense, 1376×1045 pixels) was positioned approximately 25 cm from the vocal folds; a sample image of raw data is shown in Fig. 2.3. The differential pressure transducer provided a trigger input to synchronize the PIV laser (New Wave Research

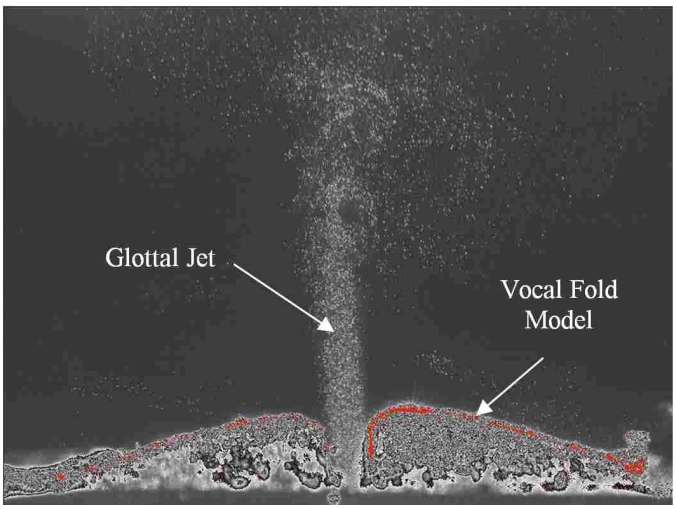

Figure 2.3: Sample raw PIV image showing instantaneous particles and vocal fold model position. Shown is a symmetric model opening at low pressure (1.0 kPa).

Solo II Nd:YAG laser) with the vocal fold vibration. Software-adjustable PIV time delay allowed for imaging at various phases.

PIV images were acquired at 30 different phases. The time delay between image pairs was 2 μs. A multi-pass 64×64 to 32×32 cross-correlation search window with 50% overlap was used to calculate velocity. Since the vocal folds vibrated at a frequency much greater than the maximum sampling frequency of the PIV system, ensemble averaging was performed over 100 image pairs at each phase. For asymmetric models, PIV data was obtained for low (1.0 kPa) and high (2.0 kPa) pressures. PIV data for the symmetric case ($L_{24}R_{24}$) were obtained at 1.0 kPa and 1.5 kPa, since the high vibration amplitude at 2.0 kPa made these models overly susceptible to damage.

A high-speed camera (Photron APS-RX) was used to examine medial-lateral model motion in the transverse plane. It was located approximately 20 cm above the model. The camera frame rate and resolution were 3000 fps and 1024×1024 pixels, respectively. Four high-intensity LED lights and controller (Visual Instrumentation Corporation #900415, #200900) were used for model illumination. High-speed images were acquired at 1.0 kPa and 2.0 kPa upstream pressures for

all models. (Because short phonation periods were adequate for high-speed data acquisition, the symmetric models were able to be imaged at an upstream pressure of 2.0 kPa.)

Using custom MATLAB codes (see Appendix A), image sequences were analyzed for frequency, glottal width, and phase shift measurements. The glottis boundary in each high-speed image was identified using grayscale intensity thresholding, from which the glottal area and half width values were directly computed. Videokymography (VKG), a method used to visualize high frequency vocal fold movement (e.g., [34,35]), was used to track the opening and closing of the vocal folds. This was done by constructing a time-sequenced compilation (kymogram) of grayscale intensity values of images of the models at the anterior-posterior center of the vocal folds through multiple cycles.

Onset pressure (the minimum pressure to initiate vibration from rest) and offset pressure (the minimum pressure to sustain vibration once initiated) were recorded, with vibration onset and offset determined by monitoring the pressure signal in LabVIEW.

An Instron tensile testing apparatus (Instron 3342) was used to measure the Young's modulus of the materials fabricated with varying silicone mixing ratios. Cylindrical test specimens measuring approximately 17 cm long and 0.9 cm diameter were manufactured. Stress was measured for a periodic strain input from 0 to 40% strain at a rate of 1000 mm/min over 10 cycles for each specimen.

2.2.4 Repeatability and uncertainty

Measurements of the symmetric model were compared to previously quantified values of similar models. Uncertainty was limited for each measurement by taking multiple measurements and averaging. For PIV analysis, uncertainty was limited by using high resolution, as well as en-

semble averaging. For Young's modulus measurements, uncertainty was minimized by averaging measurements from multiple samples.

2.3 Results and discussion

2.3.1 Young's modulus of model materials

Young's modulus values for the different layers of the different models are shown in Table 2.1. These values are similar to values used by others in both synthetic and computational vocal fold modeling (e.g., [6, 7, 20]), and the magnitude of the Young's modulus is similar to that of human vocal fold tissue in the small-strain range (approximately 10 kPa for the body layer, 3 kPa for the cover layer; e.g., [36]).

Table 2.2: Phonation onset and offset threshold pressures (kPa) and maximum glottal area (mm^2) at low (1.0 kPa) and high (2.0 kPa) pressures.

Case	P_{onset}	P_{offset}	P_{low} area	P_{high} area
$L_{24}R_{24}$	0.48	0.41	30.18	67.69
$L_{24}R_{23}$	1.35	0.94	12.58	42.48
$L_{24}R_{22}$	1.23	0.94	12.05	37.12

2.3.2 Onset and offset pressure

The symmetric model had the lowest frequency of vibration (approximately 103 Hz at 2.0 kPa) and the lowest onset and offset pressures, as shown in Table 2.2. Interestingly, the onset pressure significantly increased as asymmetry was introduced ($L_{24}R_{23}$ model) but did not increase further as asymmetry was enhanced ($L_{24}R_{22}$ model). Increased pressure required to induce self-

oscillation can be correlated to increased effort necessary to speak. Thus, lower onset pressures are preferable.

2.3.3 Kinematic variables

Asymmetry significantly affected the maximum glottal area, as shown in Table 2.2, causing an over 50% decrease for the low pressure cases and an approximately 30% decrease for the high pressure cases. This decreased area could cause either reduced mass flow through the glottis and/or increased flow velocity. However, since the coupling between glottal flow and radiated sound is complex and not yet fully understood (e.g., [37, 38]), further studies would need to be performed to determine the effect of the decreased area on radiated sound amplitude and quality.

High-speed images for selected symmetric and asymmetric cases are shown in Fig. 2.4. High-speed VKG images for all cases are shown in Fig. 2.5. As is evident in Figs. 2.4 and 2.5, in some cases the mid-region of the stiff vocal fold model was overlapped by the opposing less-stiff vocal fold model.

In Fig. 2.4, the differences in glottal area over one cycle are shown. In the symmetric case, the glottal area stays primarily symmetric throughout the cycle, whereas for the asymmetric case, the glottal area does not stay symmetric. Also, phase delays between the left and right model are also evident.

In Fig. 2.5, differences in glottal area are shown between the symmetric and asymmetric cases. Furthermore, phase differences between the left and right model are shown. No evidence of mucosal wave-like motion can be seen from any of the VKG images.

Data derived from the high-speed images include glottal area (Fig. 2.6), glottal half-width (Fig. 2.7), and phase shift (Fig. 2.8). The two asymmetric models had similar glottal half-widths

$L_{24}R_{24}$, Low Pressure (1.0 kPa)

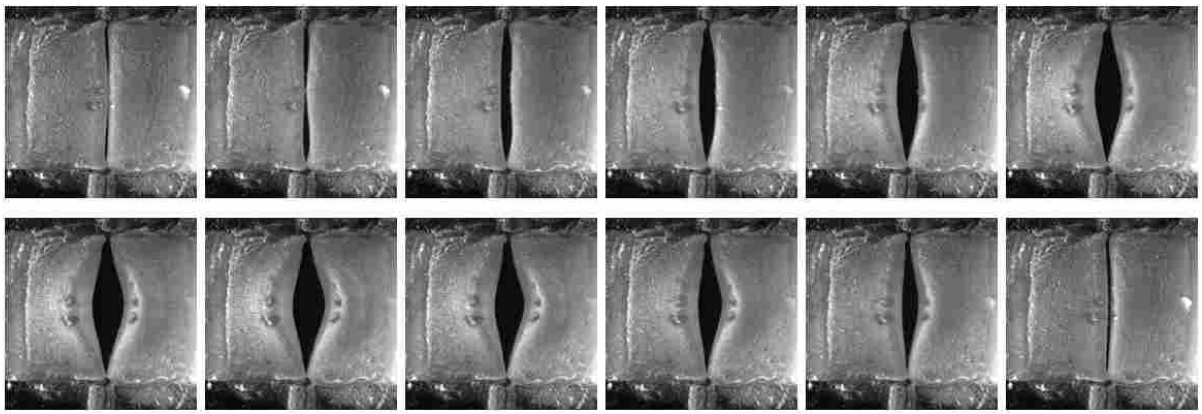

$L_{24}R_{22}$, High Pressure (2.0 kPa)

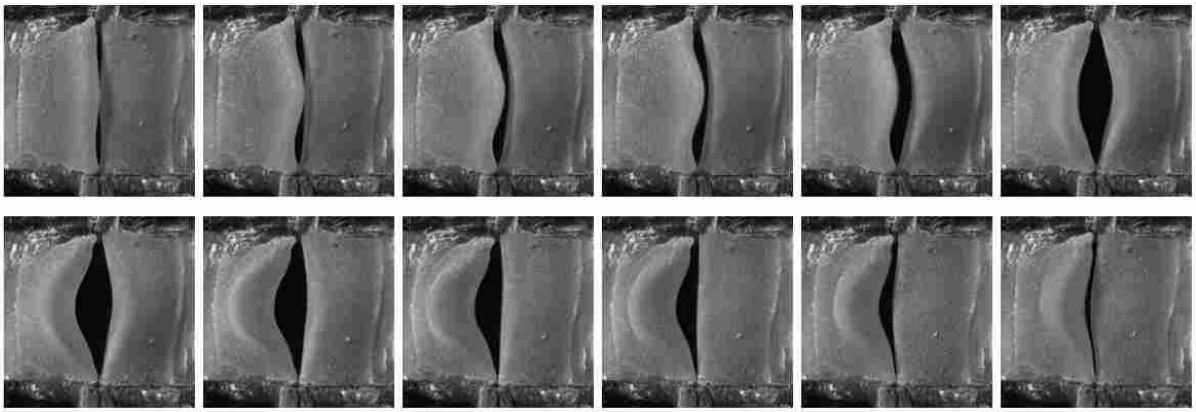

Figure 2.4: Sample high-speed images over one cycle for symmetric (top) and asymmetric (bottom) cases.

that were both significantly smaller than that of the symmetric model. Reduced vibration amplitude is consistent with a clinically observed "weak" or "hoarse" voice characteristic. It is also important to note that the orifice between the asymmetric models (the "glottis") did not close completely during the glottal cycle (see Fig. 2.6); this would contribute to a "breathy" voice.

These results show that increasing the stiffness of one vocal fold significantly reduces the amplitude of both vocal folds, and not just that of the stiff vocal fold. In treating conditions in which asymmetric vocal fold stiffness is a concern, a close match between Young's modulus values for

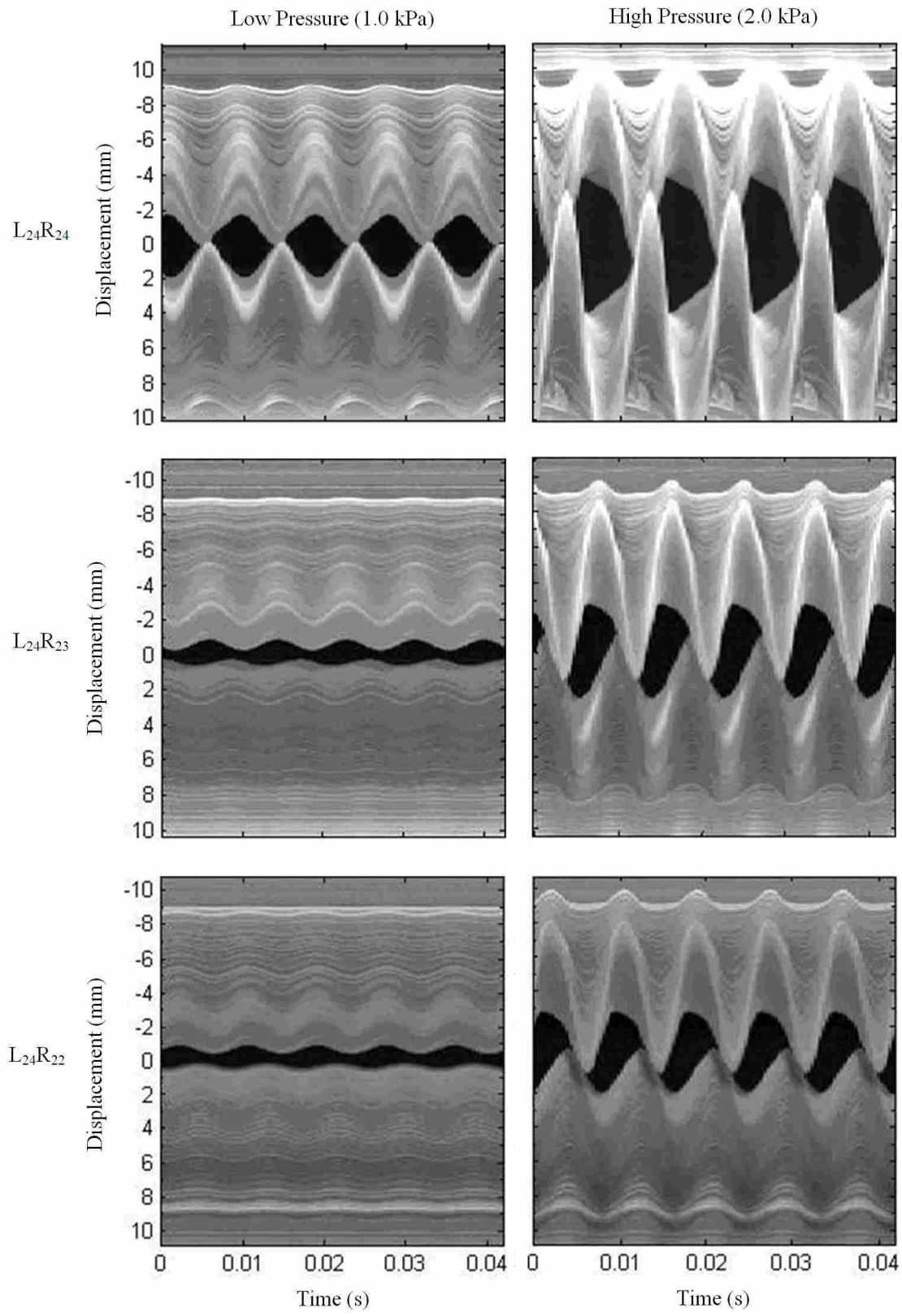

Figure 2.5: High-speed videokymographic images for asymmetric and symmetric models at low and high pressures. The top model is L_{24} (baseline symmetric model) in every case.

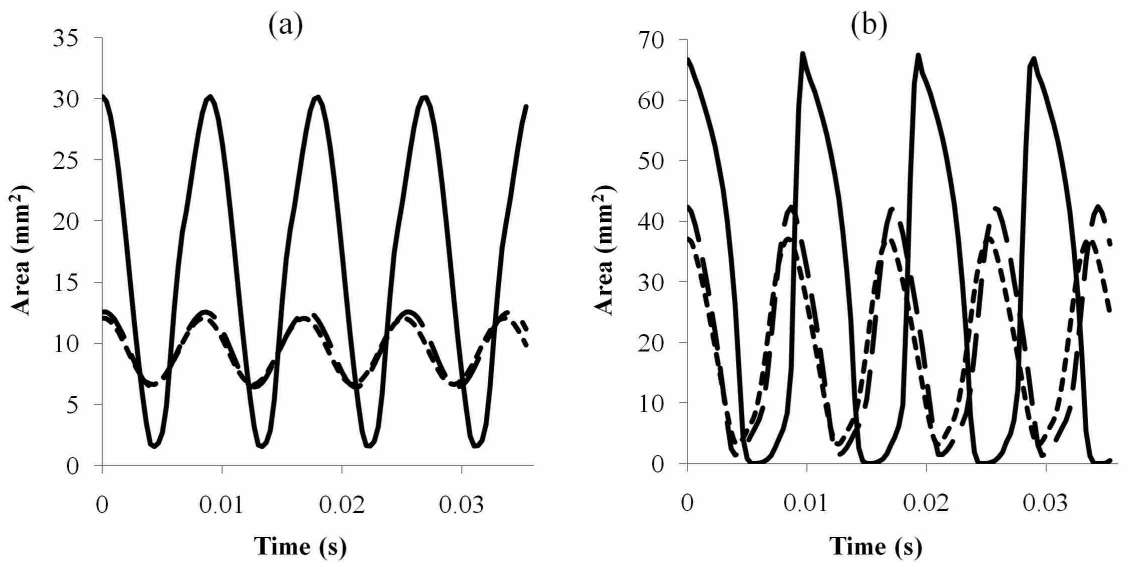

Figure 2.6: Glottal area derived from VKG images for (a) low (1.0 kPa) pressure and (b) high (2.0 kPa) pressure. Vertical scales area adjusted. Data for asymmetric (short dashes - $L_{24}R_{22}$, long dashes - $L_{24}R_{23}$, solid - $L_{24}R_{24}$) models are compared.

both covers is highly preferable. In the $L_{24}R_{23}$ case, the right cover modulus was relatively close to that of the left cover, but nevertheless yielded a reduction of approximately 50% in vibration amplitude at the 1 kPa pressure. Given the high variability of tissue stiffness between individuals (e.g., [36]), precise stiffness matching may be difficult and would require a method for *in vivo* measurement of the healthy fold's Young's modulus.

The left and right models appeared to oscillate at the same frequency, although longer recordings would be required to confirm this. The phase between the two sides differed significantly in the presence of asymmetry. As asymmetry increased, the phase difference also increased up to 90° for the 2 kPa, highest asymmetry case (see Fig. 2.8). The phase difference alters the shape of the glottal area, in turn influencing the flow rate waveform and hence quality of generated sound. It is speculated that this out-of-phase asymmetry could possibly result in a qualitatively

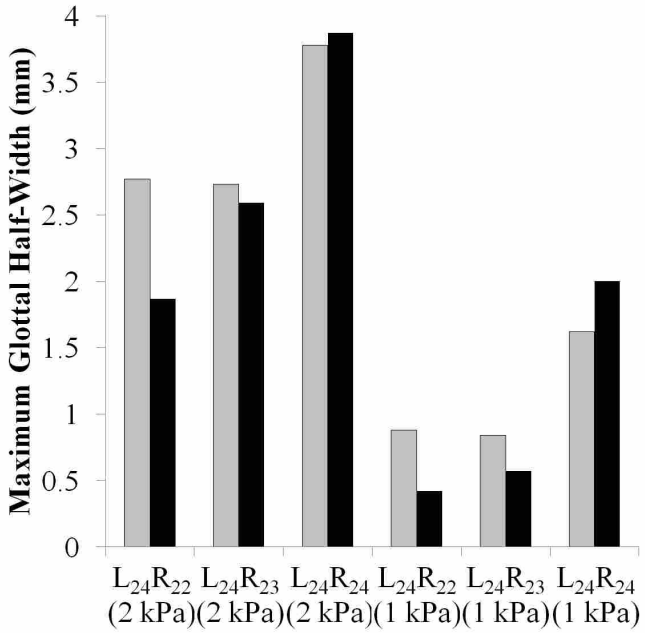

Figure 2.7: Maximum glottal half-width measured (clear bar - left vocal fold, solid bar - right vocal fold) using high-speed VKG images, for symmetric and asymmetric models at high and low pressures.

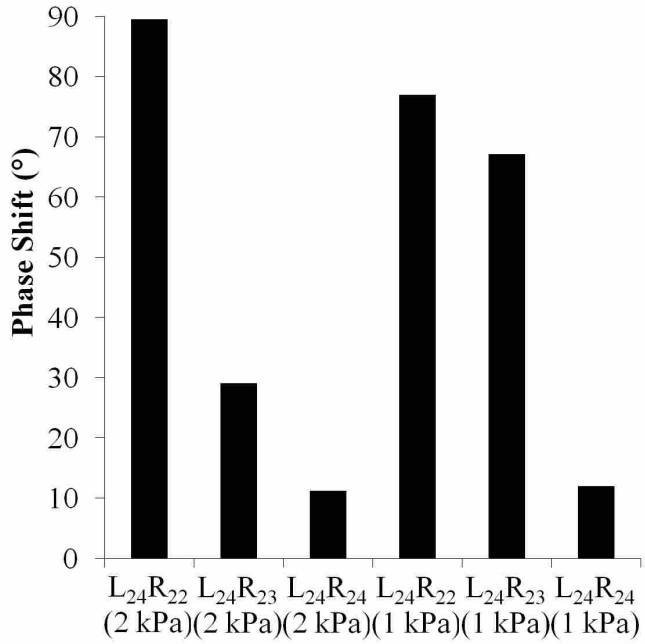

Figure 2.8: Phase shift derived from high-speed VKG images for symmetric and asymmetric models at high and low pressures.

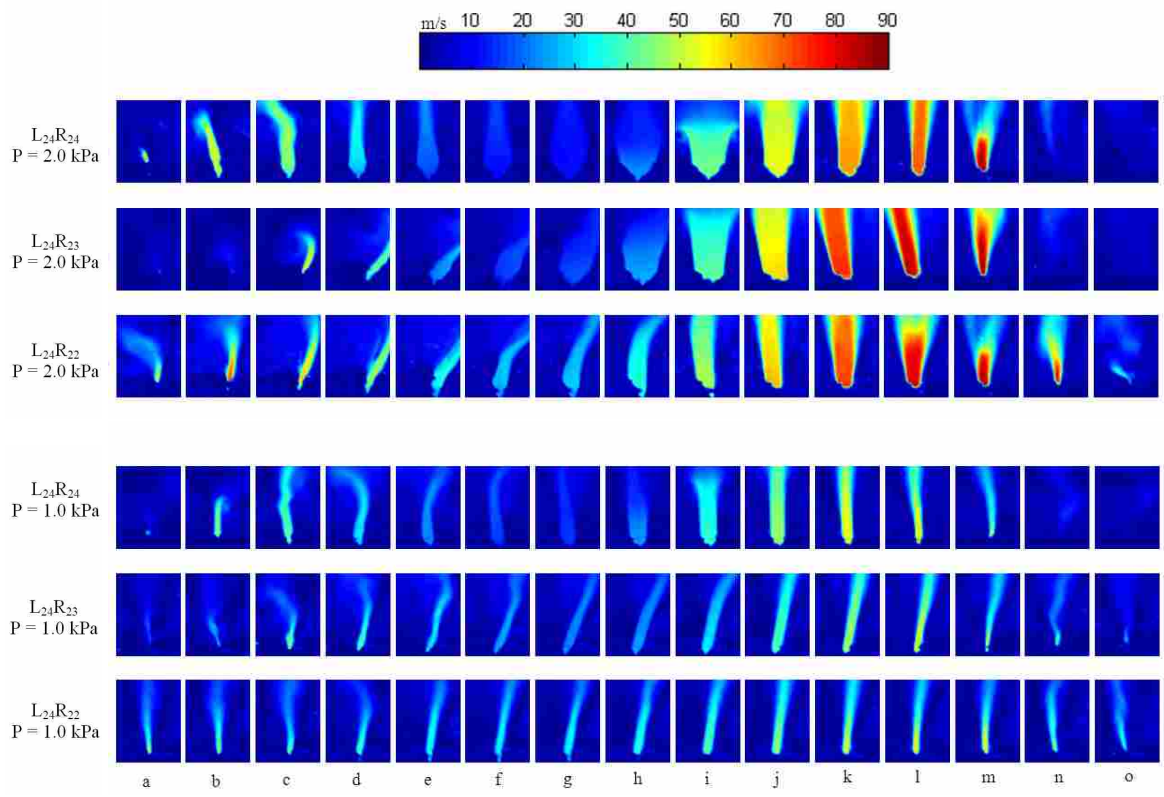

Figure 2.9: Velocity magnitude from PIV data for asymmetric and symmetric cases at low and high pressures. Images were obtained at 30 phases over the cycle and velocity fields were ensemble averaged; only every-other-phase is shown here.

"unnatural" sounding voice, although further studies with a vocal tract would be necessary to investigate this.

2.3.4 Glottal jet

PIV velocity contours are shown in Fig. 2.9; every-other recorded phase is displayed. From left to right (*a* to *o*), each model completes one cycle. The model is closed at *a* and *o*, and completely open around *h* and *i*. The contours show velocity profiles throughout the cycle. The top three sequences are for high pressure cases, and the bottom three sequences are for low pressure cases. The top line for both pressure cases is the symmetric model ($L_{24}R_{24}$).

Except for during immediate opening and closing, the symmetric model yielded a relatively symmetric jet near the glottal exit; asymmetry in the jet further from the glottal exit is evident, likely due to flow instability associated with free jets. In contrast, the two asymmetric models yielded skewed velocity profiles, generally towards the stiffer model (right side), for both pressures. At the low pressure, the jet was generally skewed towards the stiffer model throughout the cycle, with the exception of the immediate opening and closing. At the high pressure, the jet straightened out during most of the open phase. This behavior was likely due to the angle of the medial surface of the models with respect to the vertical plane. At immediate opening and closing, the models were at roughly the same elevation vertically and likely were of similar instantaneous geometry. During the bulk of the open phase, however, the stiffer model was lower in elevation than the flexible model; consequently, the flexible model medial surface would be expected to have a greater divergence angle than the stiffer model. The flow thus remained attached to the wall with a lower divergence angle. At the higher pressure, however, the stiffer model angle was sufficiently large that the flow separated from the inferior glottal margin and did not skew significantly. As skewing of the glottal jet may adversely influence sound production, for example, by potential impinging the glottal jet on the ventricular folds causing broadband sound generation, it is generally thought to be desirable that the jet be as symmetric as possible.

Such glottal jet skewing has been seen in other vocal fold models, including synthetic rigid [14], self-oscillating [23] and excised canine [25] models. In the case of the nominally symmetric rigid model of Shinwari et al. [14], skewing was attributed to the Coanda effect (the tendency of a fluid jet to be attracted to a nearby surface). In the case of the self-oscillating synthetic model of Neubauer et al. [23], skewing was attributed to uneven mounting of the left and right models. In the case of the canine models of Khosla et al. [25], skewing was attributed

to differences in stiffness between the vocal folds. Skewing has also been shown to occur due to lateral offsetting of a supraglottal duct [20]. These studies highlight the sensitivity of the glottal jet to its surroundings. In the present study, since introduction of asymmetric materials strongly influenced the instantaneous glottal geometry, and since the asymmetric models all demonstrated more skewing than the symmetric models, it is reasonable to conclude that material asymmetry played a significant role in causing glottal jet skewing. This is consistent with the findings of Khosla et al. [25]. However, contribution due to potential slight unevenness in mounting cannot be ruled out. The role of the Coanda effect in influencing the dynamics of a jet through a time-varying glottis is currently an open question in voice research, and no speculation is made here regarding its potential role in the jet skewing observed in these studies.

2.4 Conclusions and future research

Asymmetry in the stiffness of synthetic vocal folds is shown to reduce glottal width by as much as 1.25 mm, introduce phase differences between the left and right folds up to 90°, increase onset pressure by almost 300%, and contribute to asymmetric glottal velocity profiles. These suggest that from a phonatory perspective, close matching of left-right stiffness is desired, since increased stiffness of one fold (that is, a greater degree of asymmetry) appears to result in: (1) smaller glottal area; (2) higher onset pressure resulting in greater required phonatory effort; (3) incomplete glottal closure, resulting in breathy voice; and (4) jet skewing, potentially contributing to broadband sound production.

Several areas of future work are suggested. Firstly, comparison should be made of these results with those obtained with a supraglottal vocal tract and false vocal folds. While numerous synthetic and excised larynx studies have been performed without a vocal tract - usually for in-

strumentation access - it has been shown (e.g., [20, 39]) that a vocal tract can directly influence the glottal jet. The vocal tract can also present an acoustic loading, thus potentially forming strong acoustic coupling between the vocal folds and the vocal tract [39]. Other areas of suggested work include: similar studies using computational models for more precise control over stiffness and geometry; further investigation into the effects of increased phase difference in asymmetric vocal fold vibration, including the presence or absence of irregular phonation as evidenced by slightly different frequencies; and development and testing of improved models (e.g., with nonlinear stress-strain characteristics and less idealized geometry) to more closely mimic human vocal folds.

CHAPTER 3. IDEALIZED VS. MRI-BASED SYNTHETIC VOCAL FOLD MODELS [1]

Recent vocal fold vibration studies have used models that were defined by idealized geometry. Although these models exhibit important similarities with human vocal fold vibration, some aspects of their motion are less than realistic. In this chapter it is demonstrated that more realistic motion may be obtained when using models with geometry derived from magnetic resonance imaging (MRI) data. The dynamic response of both idealized and MRI-based synthetic vocal fold models are presented. MRI-based model improvements include evidence of mucosal wave-like motion and less vertical movement. Limitations of the MRI-based model are discussed and suggestions for further synthetic model development are offered.

3.1 Introduction

Synthetic and computational vocal fold models described in the literature have typically been defined using simplified geometries. One example is the so-called "M5" model of Scherer et al. [13]. Self-oscillating models based on this geometry exhibit some life-like characteristics and have thus been used to simulate human vocal folds in research, for example: to study acoustically and aerodynamically-driven vibration modes [21], characterize supraglottic vortices [23], develop *in vivo* measurement devices [26], study acoustical effects of non-human mammalian air

[1] This chapter was published as Pickup, B.A., Thomson, S.L. (In Press). "Flow-induced vibratory response of idealized vs. magnetic resonance imaging-based synthetic vocal fold models," Journal of the Acoustical Society of America Express Letters

sacs on voice quality [33], estimate the sensitivity of vocal fold response to lateral material stiffness asymmetry [40], and investigate fluid-structure and acoustic-structure interactions [12].

M5-based studies such as these allow for parametric physical modeling and detailed experimentation without using excised larynges, and they present several advantages and disadvantages. Advantages include low cost, low maintenance, durability, control over geometric and material property parameters, and relatively good agreement with human vocal fold characteristics, such as true self-oscillation capability and similar phonation threshold pressures. Disadvantages include (a) idealized geometry, including a uniform anterior-posterior cross section profile, and (b) some dissimilarity with true vocal fold motion, including a generally more divergent glottal profile during the entire vibratory cycle, the lack of mucosal wave-like motion, and large vertical (inferior-superior) motion.

Considering recent studies [41–43] that have highlighted the role of geometry in vocal fold response, it is likely that the differences between the responses of the M5-based models and the true vocal folds are due to geometric as well as material property differences. The purpose of this chapter is to show that more life-like motion can indeed be achieved when using more realistic geometry. This is done by comparing the flow-induced responses of two synthetic, self-oscillating models of matching material properties but differing geometries. One model was based on the idealized M5 geometry. The other was based on geometry derived from magnetic resonance imaging (MRI) data [44]. It is hoped that these findings will stimulate and provide direction for research efforts aimed towards developing improved synthetic vocal fold models for human voice production research.

3.2 Methods

3.2.1 Geometry definition

The M5 model geometry was based on the definition given by Scherer et al. [13] with a 2 mm cover layer [40]. The shape of the MRI-based model was obtained as follows (see Fig. 3.1):

1) Vocal fold tissues were outlined from each MRI image via commercial segmentation software (Velocity2™);

2) Segmented regions were exported as three-dimensional stereolithography (STL) files;

3) STL files were imported into commercial computer-aided design (CAD) software (Pro/ENGINEER), scaled to approximately match typical laryngeal size [45,46] and cropped;

4) Cropped STL files (one for the cover layer, one for the body layer) were exported from Pro/ENGINEER, from which solid models were fabricated using rapid prototyping hardware; and

5) Negative molds were fabricated from rapid prototyped solid models, from which final models were fabricated as described in the next section.

The M5 and MRI-based model geometries are shown in Fig. 3.1. The M5 model was a simplified geometry, whereas the MRI-based model had a complicated surface geometry that was more realistic to human vocal folds. Both models contained a convergent portion and were relatively the same size.

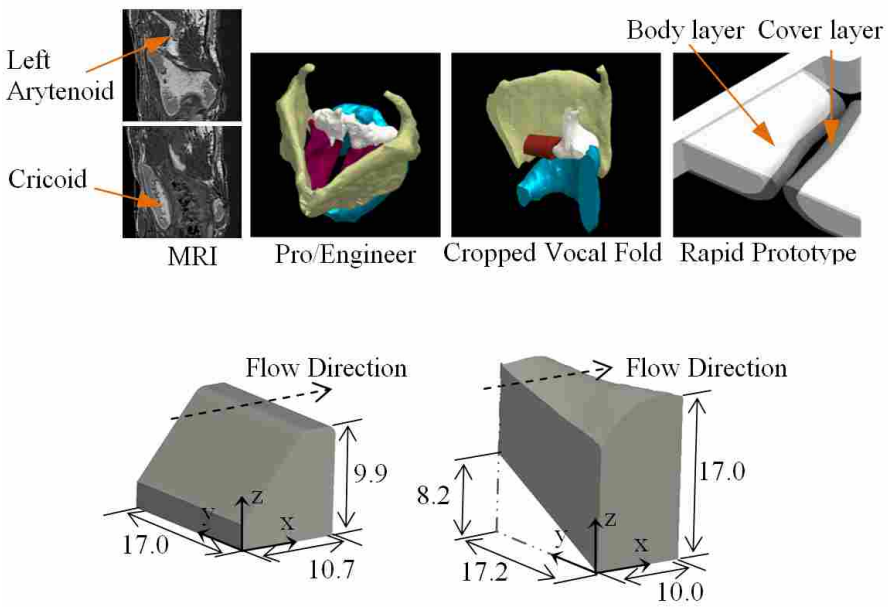

Figure 3.1: Top row: MRI geometry extraction sequence showing, from left to right, representative sagittal images, Pro/ENGINEER CAD models, cropped CAD model, and models of body and cover layers for rapid prototyping. Bottom row: Isometric views of M5 (left) and MRI (right) models. The *x*-, *y*-, and *z*-coordinates are aligned with the vertical (inferior-superior), anterior-posterior, and medial-lateral directions, respectively. All dimensions are in mm.

3.2.2 Model fabrication

Similar to previous studies [33, 40] and as previously described in Chapter 2, all models were made using two-part Ecoflex 0030 addition-cure silicone, combined with a Silicone Thinner (Smooth-On, Inc.) Increased amounts of thinner yielded lower Young's moduli of the cured material. Different ratios of thinner were used for the body and the cover layers. Models with a compound mixing ratio of 1:1:2 (i.e., one part each of Ecoflex compounds A and B to 2 parts Silicone Thinner) for the body and 1:1:4 for the cover were fabricated, as well as models with 1:1:3 and 1:1:5 mixing ratios for the body and cover layers, respectively. Four different models were tested, here referred to by their geometry and body-cover thinner-to-silicone ratios: $M5_{24}$, $M5_{35}$, MRI_{24}, and MRI_{35}. To ensure material consistency, models with identical modulus values were created simultaneously (i.e., the $M5_{24}$ and MRI_{24} body layers were made at the same time

using the same material batch, as were the cover layers, and so on). The models were mounted to 38×70×6.35 mm acrylic plates using silicone adhesive (Sil-Poxy©, Smooth-On, Inc.) applied to the lateral, anterior, and posterior surfaces. The plates were then mounted on an air flow supply tube that was connected upstream to a compressed air source.

To measure the Young's modulus, a cylindrical test specimen of each material was fabricated concurrently with model fabrication and tested using an Instron tensile testing apparatus (Instron 3342). The Young's modulus values (1.5 kPa for 1:1:5, 2.94 kPa for 1:1:4, 5.2 kPa for 1:1:3, and 8.5 kPa for 1:1:2 mixing ratios) were similar to those reported in previous synthetic model studies and are generally agreeable with approximate values for human vocal fold tissue [36].

3.2.3 Experimental setup and methods

The experimental setup was the same as that described in Chapter 2, with additional high-speed camera positions for different views of the models. The only aspects of the setup that changed during the data acquisition process (described below) were the exchange of acrylic plates containing the different models and the high-speed camera positioning. The acrylic plates used for the MRI and M5 models were machined such that the medial surfaces of opposing vocal fold models were approximately in contact when there was no flow.

Data acquired for all models during flow-induced vibration included onset and offset pressures, glottal area, model motion, and vertical (inferior-superior) displacement. Onset pressure was measured using a pressure sensor (Omega PX138-001D5V) mounted approximately 3 cm upstream of the model. The sensor fed information into a custom National Instruments LabVIEW software program that displayed pressure fluctuations during vibration. Onset pressure was identified by slowly increasing the upstream pressure until self-oscillation was induced (i.e., a steady

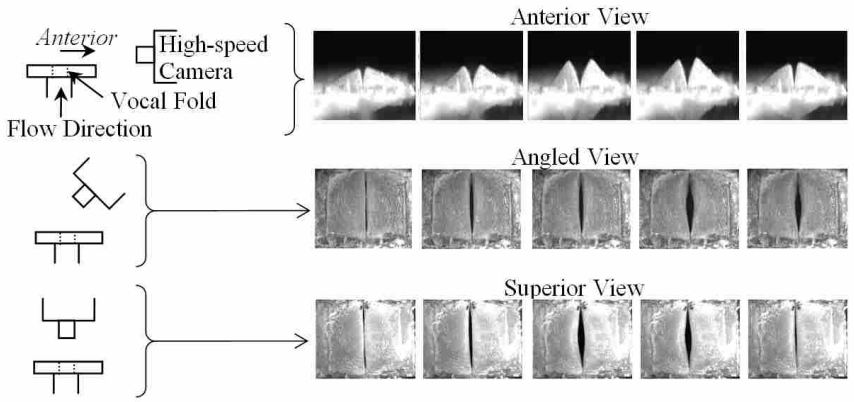

Figure 3.2: High-speed camera positioning (left) and corresponding images (right) of the $M5_{24}$ model at 133% P_{onset}.

sinusoidal wave was visible on the LabVIEW screen). Offset pressure was measured by decreasing the pressure until vibration ceased (i.e., the sinusoidal wave stopped). This process was repeated five times, and averages are here reported. The measurements had a maximum standard deviation of 0.05 kPa.

A high-speed camera (Photron APX-RS) was used to image glottal area and model motion from anterior, angled (approximately 45° in the sagittal plane), and superior perspectives (Fig. 3.2). Images were recorded at 9000 frames per second at resolutions ranging from 400×800 to 1024×1024 pixels. Glottal area and vertical displacement measurements were obtained for each model at two pressures corresponding to 110% and 133.3% of each model's onset pressure. Custom MATLAB subroutines were used to quantify glottal area, vertical displacement and to create videokymographic (VKG) images from the coronal midplane of the model (Appendix A); the latter were used to support the determination of whether mucosal wave-like motion was present.

3.3 Results and discussion

3.3.1 Threshold pressures

Onset and offset pressure data are listed in Table 3.1. The M5 models exhibited lower onset pressures than the MRI models, and were closer to human vocal fold onset phonation threshold pressures (around 0.30 kPa [47, 48]). MRI model onset pressures were closer to values measured for canine vocal folds (around 1.0 kPa [49]). Both models operated within ranges typical of human phonation (around 0.3 kPa to 4.0 kPa [50]). The MRI model onset pressure may be able to be reduced (and thus improved to be more life-like) using other modeling methods, such as lowering the modulus cover layer materials and/or implementing further geometric changes. In terms of threshold pressure, the M5 model functions more similarly to human vocal folds than the MRI-based model.

Table 3.1: Threshold pressure and maximum glottal area data for M5 and MRI models.

		$M5_{24}$	$M5_{35}$	MRI_{24}	MRI_{35}
Threshold Pressure (kPa)	*Onset*	0.65	0.91	2.25	1.86
	Offset	0.52	0.33	2.06	1.68
Maximum Glottal Area (mm^2)	*110%*	7.06	33.27	5.83	6.29
	133%	15.38	47.23	11.97	11.17

3.3.2 Glottal area

Also shown in Table 3.1 are maximum glottal areas from the high-speed images taken from the superior perspective. Area was calculated using a custom MATLAB subroutine to identify the glottis based on pixel intensity. This was done by setting a threshold pixel intensity for the glottis (close to 0 since the area was darker than the vocal fold model) and tracking that area through time;

the uncertainty was estimated to be $\pm$ 1.53 mm^2 (detailed description of the uncertainty analysis is provided in section 3.3.6). The maximum glottal areas increased with increased pressure for all models at all pressures. The M5 models had significantly larger areas than the MRI models, despite the MRI models operating at significantly higher pressures. This was attributed to reduced body layer deformation and vertical displacement (discussed below) of the MRI models. In terms of glottal area, the MRI-based models behaved more life-like than the M5 models.

3.3.3 Vertical displacement

A significant drawback of the M5 models has been its large, unnatural vertical displacement during vibration. The MRI-based models did not exhibit this behavior. This can be seen in Fig. 3.3, which shows high-speed images from anterior and angled perspectives of the M5 and MRI models during vibration. By comparing the images for the M5 and MRI models, it is evident that the M5 model vibrated with excessive vertical (seen in anterior view images) and vertical-lateral displacement (seen in angled view images) of the superior and medial surfaces, whereas that of the MRI model was much more realistic.

As a quantitative measure illustrating this behavior, Table 3.2 lists the vertical displacement data for each case. The data correspond to the height, H, of the highest point on the vocal fold model as seen in the images acquired from the anterior view (Fig. 3.2). H_{max} and H_{min} denote the maximum and minimum model height, respectively, over the oscillation cycle. Especially noteworthy is the net displacement, $H_{net} = H_{max} - H_{min}$. For the M5 models, H_{net} varied from 0.57 to 2.31 mm, indicating significant vertical displacement during vibration. For the MRI models, H_{net} varied from 0.12 to 0.54 mm, which is much smaller than for the M5 models. Thus, in terms of vertical displacement, the MRI models behaved more life-like than the M5 models.

$M5_{35}$ (1.20kPa)

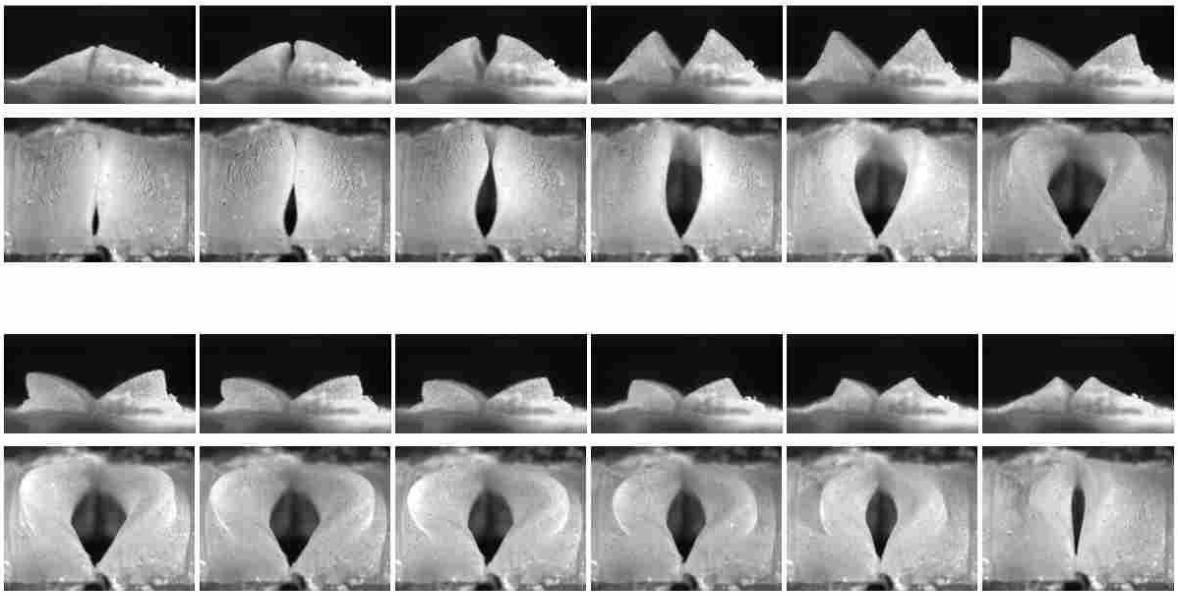

MRI_{35} (2.47kPa)

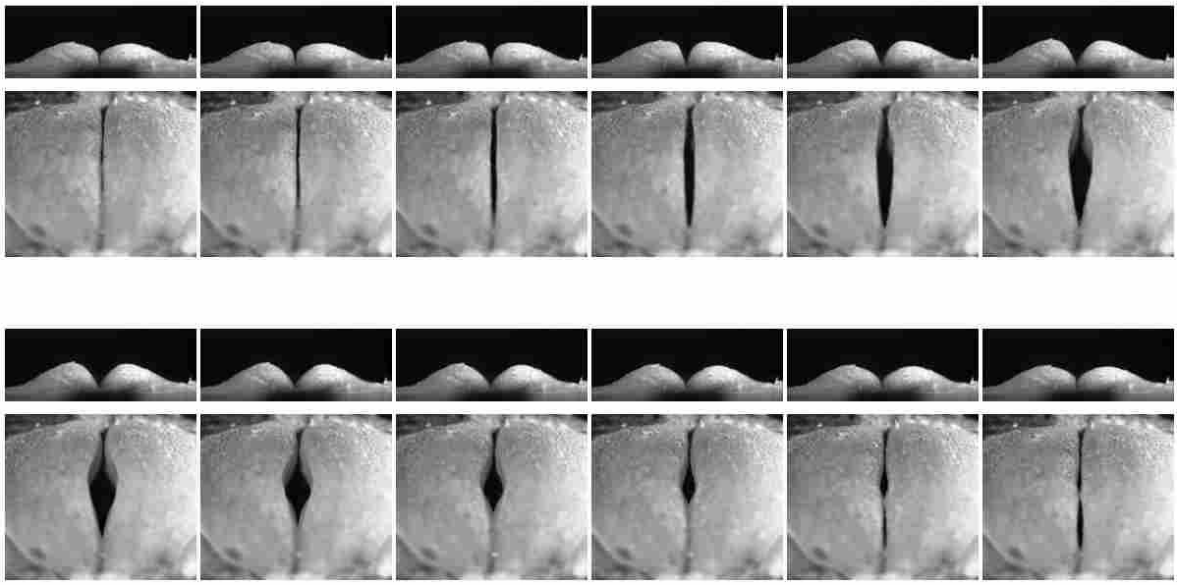

Figure 3.3: Anterior (above) and angled (below) images from high-speed camera of the M5 (top) and MRI-based (bottom) models through one oscillation.

Table 3.2: Vertical displacement (height) data for M5 and MRI models.

	$M5_{24}$		$M5_{35}$		MRI_{24}		MRI_{24}	
	110%	*133.3%*	*110%*	*133.3%*	*110%*	*133.3%*	*110%*	*133.3%*
H_{max}(mm)	3.28	3.96	5.13	6.25	4.59	5.25	4.34	4.23
H_{min}(mm)	2.71	2.83	3.33	3.94	4.47	4.89	3.80	3.68
H_{net}(mm)	0.57	1.13	1.79	2.31	0.12	0.36	0.54	0.54

3.3.4 Model motion

Other evidence of improved MRI-based model motion is in the glottal profile, also seen in Fig. 3.3. While not entirely visible, the M5 model glottis profile in the anterior view images was divergent over a significant portion of the oscillation cycle (this was particularly apparent at low oscillating pressures). By contrast, the MRI model glottis profile in the anterior view images appeared to feature an alternating convergent-divergent pattern that is more typical of human vocal fold vibration. Other imaging methods (e.g., using a hemilarynx arrangement) would be necessary to verify this observation, as well as to quantify convergent-divergent and other aspects of the models' motion. It is possible that an M5 model with a convergent prephonatory shape may yield improved convergent-divergent self-oscillating motion, and this prospect is discussed further in Chapter 4.

The difference in deformation between the models can be seen in Fig. 3.3. Again, the M5 model has much more vertical and vertical-lateral displacement. Also, evidence of anterior-posterior mucosal wave-like motion, as well as anterior-posterior asymmetries in vibration, are evident in the MRI model videos, both of which are absent in the M5 model videos.

Further evidence of mucosal wave-like motion can be seen in the VKG images in Fig. 3.4. With the M5 model, the deformation curves above and below the glottis (in Fig. 3.4; anatomically, these curves are in the medial-lateral direction) are in-phase; however, with the MRI model, these

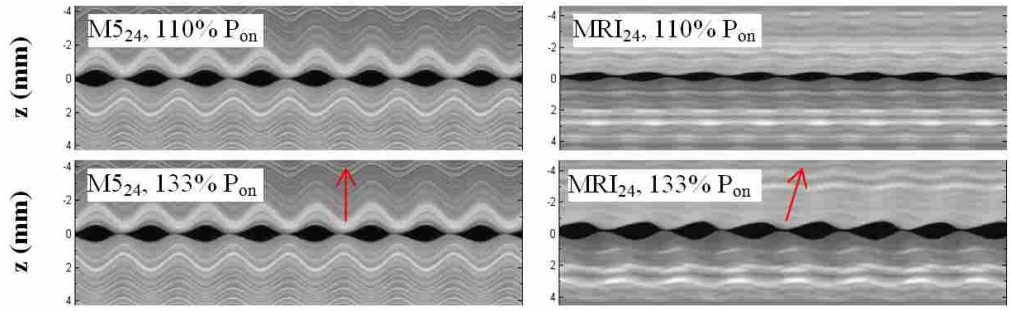

Figure 3.4: VKG images showing mucosal wave-like motion produced by the MRI models (right), but not by the M5 models (left). Red arrows indicate direction of wave motion.

curves are slightly out-of-phase, providing evidence of a traveling "mucosal" wave-like feature. This improvement is significant given the important role that the mucosal wave plays in human vocal fold function and clinical observation.

3.3.5 Medial surface equation

For reference, an equation approximating the medial surface of the MRI-based model, calculated using a 5th-order surface fit to the STL file data in MATLAB, is given below (all units are in μm, and a coordinate system is provided in Fig. 3.1). The R^2 value was 0.989, and the equation is for the domain $0 < x < 10$ mm, $0 < y < 17.22$ mm.

$$\begin{aligned} z(x,y) \;=\; & -3.33\times10^{-1}x^5 + 8.92\times10^{-2}x^4y + 6.18x^4 + 2.56\times10^{-1}x^3y^2 - \\ & 6.89y - 25.31x^3 - 1.88\times10^{-2}x^2y^3 - 2.53x^2y^2 + 69.29x^2y - 149.75x^2 - \\ & 3.54\times10^{-2}xy^4 + 1.39xy^3 - 8.97xy^2 - 169.74xy + 1572.76x + \\ & 2.39\times10^{-2}y^5 - 9.94\times10^{-1}y^4 + 14.56y^3 - 88.12y^2 + 434.90y + 13.129\times10^3 \end{aligned} \tag{3.1}$$

3.3.6 Uncertainty analysis

The uncertainty of the glottal area measurements, u_{area}, was estimated using a combination of zero-order (u_o), threshold (u_{th}), and calibration (u_c) uncertainties, as follows:

$$u_{area} = \pm\sqrt{u_o^2 + u_{th}^2 + u_c^2}. \tag{3.2}$$

Uncertainty due to the resolution of the high-speed camera was calculated using

$$u_o^2 = \pm\frac{1}{2}\left[\left(\frac{1\,pixel}{pixels/mm}\right)^2\right]^2. \tag{3.3}$$

An average of each of the model cases' resolution (pixels/mm) for the camera in the superior position was calculated and used in Eq. 3.3. The value for the MRI_{35} model's uncertainty was found to be the highest (1.3×10^{-6} mm^2) and was thus used as the u_o value in Eq. 3.2.

The threshold uncertainty was due to differences in measured glottal area based on the threshold for calculating pixel intensity differences between the physical vocal fold model and the airway, and was calculated using

$$u_{th}^2 = \left(\frac{dA}{dTh}c_{th}\right)^2, \tag{3.4}$$

where A represents the glottal area, Th represents the assigned threshold value (from 10 to 80, based on a maximum value of 255 for 8-bit grayscale intensity values in MATLAB), and c_{th} represents the difference of threshold values per case that yielded reasonable area measurements. Values of c_{th} ranged from 20 to 40. The maximum glottal area was calculated at the range of threshold values. The difference of area based on changing threshold values was calculated for each case

(i.e., the slope $\frac{dA}{dTh}$). Each model's uncertainty based on threshold was calculated, and the worst case was from the MRI_{24} 133% onset pressure case ($u_{th} = 1.49$ mm^2).

The calibration uncertainty was due to differences in location selection when calibrating the high-speed videos, and was calculated using

$$u_c^2 = \left(\frac{dA}{dy} y_p\right)^2. \tag{3.5}$$

The sensitivity of the glottal area to the user-selected calibration points, $\frac{dA}{dy}$, was calculated by varying the selection of the calibration ruler provided in the calibration images for each model at the superior view. A position of 2 pixels in either direction of the user selected position was used to adjust the pixels/mm calibration. Areas corresponding to these varying calibration points were calculated, and the differences between largest and smallest areas were used to calculate dA. The overall difference in y-position for the expected mis-selected calibration points was used to calculate dy. The uncertainty in selecting calibration points was estimated to be $y_p = \pm 4$ pixels. The highest uncertainty was found in the $M5_{35}$ model ($u_c = 0.36$ mm^2).

Substituting $u_o = 1.3 \times 10^{-6}$ mm^2, $u_{th} = 1.49$ mm^2, and $u_c = 0.36$ mm^2 into Eq. 3.2 yielded a total uncertainty for the glottal area calculations of $u_{area} = 1.53$ mm^2.

3.4 Conclusions and future work

The flow-induced responses of the MRI-based synthetic models showed remarkable differences compared with those of the M5 models. Improvements include:

1) less vertical motion (by 1.77 mm);

2) apparently more typical alternating convergent-divergent glottal profile pattern; and

3) evidence of mucosal wave-like motion.

The primary disadvantage of the MRI models was the higher onset pressure, and techniques to lower the onset pressure are currently being researched. It is interesting to note that the MRI model exhibited asymmetric anterior-posterior vibrations and some irregularities in glottal area waveforms at higher pressures; these observations are not necessarily perceived as being advantageous or disadvantageous.

Since fabrication methods for both the M5 and MRI models were similar, the differences between the two models' motions are primarily attributable to differences in geometry. It is, of course, expected that different geometries will yield different vibration patterns. What is significant, however, is that the MRI model showed important improvements in yielding more life-like motion than the M5 model while using the same materials.

It is emphasized that further developments are still needed to create truly life-like synthetic self-oscillating models. Additionally, research into understanding synthetic vocal fold model response is needed. For example, this research does not address the issue of which geometric features governed the various aspects of the vibratory responses of the M5 and MRI models. It is possible that the M5 model may be geometrically altered to improve its response. Systematic, parametric investigations of geometric features of the M5 and other vocal fold models, similar to the recent work by Zhang [12] and Cook et al. [11], is discussed in Chapter 4.

The role of material properties in governing vocal fold model response must also continue to be explored; synthetic model materials reported in the literature (including the present ones) have typically been isotropic and linearly elastic, in contrast with the anisotropic, nonlinear material

properties of vocal fold tissue. The development of more realistic synthetic materials will be an important step towards creating more life-like vocal fold models.

CHAPTER 4. INFLUENCE OF GEOMETRIC FEATURES ON VOCAL FOLD MODEL VIBRATION

Many researchers have used simplified models to simulate and study the flow-induced vibrations of the human vocal folds. While it is clear that the models' responses are sensitive to geometry, what is not clear is how and to what extent specific geometric features influence model motion. In this study a computation vocal fold model was used to identify which geometric features play significant roles in governing vocal fold movement. The model was geometrically parameterized, and a screening-type design-of-experiments approach was used to identify the relative effect of 13 geometric parameters. Five output measures were analyzed to assess the magnitude of each geometric parameter's effect on vocal fold motion, including flow-induced vibration frequency, changes in glottal width, flow rate, and intraglottal angle, and intraglottal phase delay. It is shown that the geometric parameters that most significantly influence model motion are the cover layer geometries - primarily the prephonatory intraglottal angle - and the body layer inferior angle. Simplified models with altered geometries are shown to feature evidence of improved model motion, including mucosal wave-like motion and alternating convergent-divergent glottal profiles during vibration.

4.1 Introduction

Voice production is the result of the flow-induced vibration of the vocal folds. Simplified, self-oscillating synthetic models of the vocal folds have been used to study various aspects of this

system, such as: aerodynamic energy transfer [7], coupling of subglottal acoustics with vocal fold models [21], acoustically and aerodynamically driven modes of vibration [22, 39], glottal airflow [20, 23], material asymmetries [40], flow-structure-acoustic interactions [51], and subglottal flow [52]. Synthetic models such as these are inexpensive, durable, relatively easy to fabricate, and can be conveniently parameterized. These features allow for detailed parametric investigations of the underlying flow-induced vibration physics.

While these models have demonstrated some vibratory similarities with those of the human vocal folds, such as with regards to onset pressure, frequency, and amplitude, the models have also exhibited some less-than-life-like motion-related behavior. Examples include the lack of mucosal wave-like motion (a key feature of phonation [53]), excessive inferior-superior motion [20], and a generally divergent profile during vibration (as opposed to the more realistic convergent-divergent profile) [54].

Researchers have studied how geometric parameters and material properties influence the resulting fluid, solid, and/or coupled fluid-solid dynamics of vocal fold models. For example, static models have been used to study intraglottal pressure and flow characteristics. One example is the "M5" static vocal fold model of Scherer et al. [13], used to investigate the effect of asymmetric intraglottal profiles on intraglottal pressure distributions. Using the same model, Scherer et al. [55] found that the intraglottal pressure distribution was highly dependent upon the exit radius in models with convergent intraglottal profiles. Li et al. [41] conducted numerical investigations of the influence of inferior and superior surface angles of these static vocal fold models. They showed that intraglottal pressures are relatively insensitive to inferior and superior vocal fold surface angles, although they emphasized the need to study the degree of influence these angles might have on vocal fold motion.

Studies on the effects of vocal fold thickness, epithelial membrane thickness, prephonatory glottal geometry, and cover layer material properties on phonation threshold pressure have been investigated. Titze et al. [15] studied the effects of cover layer material properties and prephonatory glottal width on phonation threshold pressure of a physical model. They showed that phonation threshold pressure increases with increasing prephonatory glottal width. Using a similar model, Chan et al. [56] showed that phonation threshold pressure increases with non-zero prephonatory glottal convergence angles, increased epithelial membrane thickness, and decreased vertical model thickness. These studies did not include analysis of the model motion.

Continuum-based numerical vocal fold models have also been studied in order to understand model response characteristics. Cook and Mongeau [8] investigated the role of lateral depth, anterior-posterior length, and vertical thickness of a single-layer, three-dimensional vocal fold model on modal frequencies. They showed that modal frequencies were most sensitive to variations in anterior-posterior length and least sensitive to changes in vertical thickness. Subsequently, Cook et al. [11] extended this study to consider how other geometric and material parameters influence the modal response of a three-dimensional body-cover layer computational model. These two studies focused on *in vacuo* modal analysis, absent flow-induced vibration. Zhang [12] used a two-layer body-cover continuum-based vocal fold model with a reduced-order flow model to study mechanical and geometric properties on model response at phonation onset. It was shown that significant changes in phonation onset frequency can be induced by slight changes in body layer stiffness, and that similar changes in phonation onset frequency may also be induced by geometric changes.

Chapter 3 showed a comparison of the flow-induced responses of synthetic models with geometries based on magnetic resonance imaging (MRI) data with the responses of models based

on the more geometrically simplified M5 model. The MRI-based models showed evidence of mucosal wave-like motion, a feature absent in the M5-based physical models. The M5-based models also showed primarily divergent motion, whereas convergent-divergent motion was evident in the MRI-based models. The M5 prephonatory intraglottal profiles were straight and it was hypothesized that convergent profiles may have improved the convergent-divergent behavior of the MRI-based models. It was concluded that parametric studies investigating the role of the effect of the various geometric features on the flow-induced vibratory response was necessary.

The research in this chapter was undertaken to determine which geometric features significantly influenced a vocal fold model's flow-induced vibratory response. The work was intended to extend the work of Cook and Mongeau [8], Cook et al. [11], and Zhang [12] by using a similarly-defined two-dimensional computational vocal fold model, only with motion fully-coupled with an unsteady, viscous, slightly-compressible flow solver. The vocal fold model (see Fig. 4.1) was a modification of the M5 model of Scherer et al. [13]. It generally consisted of linear subglottal and supraglottal profiles of varying angles, a linear intraglottal profile of varying angle and length, and rounded glottal inlet and exit regions of varying radii. A body-cover representation was used, with body and cover geometries independently defined. In order to accommodate the significant computation times required for model simulation, the geometric parameters were defined and the simulation results were analyzed based on a screening-type design-of-experiments methodology. The simulation results were analyzed to estimate the relative significance of different geometric parameters on the model's response.

In the following sections, the computational approach is described, including model parameterization, screening design, computational simulation methods, and data analysis. The results, including rankings of the influence of model parameters on various aspects of model response, are

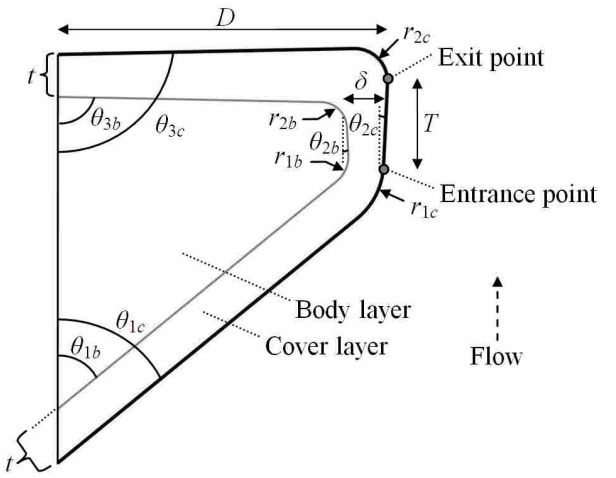

Figure 4.1: Parametric two-layer vocal fold model.

presented and discussed. Finally, suggestions for further studies of specific model parameters and development of improved models are provided.

4.2 Methods

4.2.1 Model definition and parameterization

The model body and cover layer geometries were defined using 14 parameters (Fig. 4.1). Of these the vocal fold depth, D, was constant and the other 13 were variable. The variable parameters were each given a low, baseline, and high value (see Table 4.1), according to similar values found in previous reports [13, 42, 57–60].

4.2.2 Screening design

In order to determine which geometric parameters were significant in terms of influencing model response, a twenty-run Plackett-Burman screening design-of-experiment was used to analyze the effect of the 13 variable parameters on various measurements of vocal fold motion. This approach, as opposed to a full-factorial design-of-experiment or sensitivity analysis, was taken be-

Table 4.1: Vocal fold model geometric parameter values and descriptions.

Parameter	Baseline	Low, High Values	Description
θ_{1c}, θ_{1b}	50°	49.35, 50.65°	Inferior glottal angle (cover, body)
θ_{2c}, θ_{2b}	0°	-2.75, 2.75°	Intraglottal angle (- divergent, + convergent)(cover, body)
θ_{3c}, θ_{3b}	90°	88.85, 91.15	Superior glottal angle (cover, body)
r_{1c}	1.5 mm	1.18, 1.82 mm	Entrance radius (cover)
r_{1b}	1.12 mm	0.80, 1.45 mm	Entrance radius (body)
r_{2c}	0.987 mm	0.837, 1.137 mm	Exit radius (cover)
r_{2b}	0.513 mm	0.36, 0.66 mm	Exit radius (body)
T	2.0 mm	1.85, 2.15 mm	Glottal thickness (vertical)
δ	1.15 mm	1.0, 1.3 mm	Maximum medial cover layer thickness
t	1.15 mm	1.075, 1.225 mm	Inferior and superior cover layer thickness
D	8.4 mm	8.4 mm	Lateral depth

cause of the computational cost of the model simulations (approximately 19 hours per simulation on a 2.8 GHz quad-core Intel Nehalem CPU; time to complete all cases was reduced by running simulations simultaneously on a supercomputer). The combinations of high-low parameter values for each simulation were adapted from Lawson and Erjavec [61] and are given in Table 4.2. Since 13 geometric attributes were analyzed but twenty runs were performed, six unassigned factors (X14-X19 in Table 4.2) represent unknown combinations of 2^{nd}, 3^{rd}, and higher-order interactions of the 13 assigned factors. In addition to the twenty high-low runs, an additional run with all parameters set to baseline values was executed.

The benefit of using a Plackett-Burman design is that the influence of each parameter on the measured output can be estimated using relatively few runs. The tradeoff is that interactions between parameters are confounded with the main effect of each parameter. It is therefore intended to serve as a screening design to be followed up with focused, more detailed studies on the parameters found to be significant. In this study, analysis of the magnitude of each parameter's effect was used to determine which parameters are recommended for such future detailed studies.

Table 4.2: Plackett-Burman 20-run statistical design of experiment table. “1” indicates a high geometric value; “-1” indicates a low geometric value. In row 1, factors X1 through X13 correspond to model variable parameters denoted directly underneath in row 2. Factors X14 through X20 represent unknown interactions of main factors. Run 0 corresponds to the baseline set of parameter values.

	X1	**X2**	**X3**	**X4**	**X5**	**X6**	**X7**	**X8**	**X9**	**X10**	**X11**	**X12**	**X13**	**X14**	**X15**	**X16**	**X17**	**X18**	**X19**
Run	r_{1c}	r_{1b}	r_{2c}	r_{2b}	θ_{1c}	θ_{1b}	θ_{2c}	θ_{2b}	θ_{3c}	θ_{3b}	T	δ	t	**X14**	**X15**	**X16**	**X17**	**X18**	**X19**
0	0	0	0	0	0	0	0	0	0	0	0	0	0	0	0	0	0	0	0
1	1	1	-1	-1	1	1	1	1	-1	1	-1	1	-1	-1	-1	-1	1	1	-1
2	1	-1	-1	1	1	1	1	-1	1	-1	1	-1	-1	-1	-1	1	1	-1	1
3	-1	-1	1	1	1	1	-1	1	-1	1	-1	-1	-1	-1	1	1	-1	1	1
4	-1	1	1	0.2	1	-1	1	-1	1	-1	-1	-1	-1	1	1	-1	1	1	-1
5	1	1	1	1	-1	1	-1	1	-1	-1	-1	-1	1	1	-1	1	1	-1	-1
6	1	1	1	-1	1	-1	1	-1	-1	-1	-1	1	1	-1	1	1	-1	-1	1
7	1	1	-1	1	-1	1	-1	-1	-1	-1	1	1	-1	1	1	-1	-1	1	1
8	1	-1	1	-1	1	-1	-1	-1	-1	1	1	-1	1	1	-1	-1	1	1	1
9	-1	1	-1	1	-1	-1	-1	-1	1	1	-1	1	1	-1	-1	1	1	1	1
10	1	-1	1	-1	-1	-1	-1	1	1	-1	1	1	-1	-1	1	1	1	1	-1
11	-1	1	-1	-1	-1	-1	1	1	-1	1	1	-1	-1	1	1	1	1	-1	1
12	1	-1	-1	-1	-1	1	1	-1	1	1	-1	-1	1	1	1	1	-1	1	-1
13	-1	-1	-1	-1	1	1	-1	1	1	-1	-1	1	1	1	1	-1	1	-1	1
14	-1	-1	-1	1	1	-1	1	1	-1	-1	1	1	1	1	-1	1	-1	1	-1
15	-1	-1	1	1	-1	1	1	-1	-1	1	1	1	1	-1	1	-1	1	-1	-1
16	-1	1	1	-1	1	1	-1	-1	1	1	1	1	-1	1	-1	1	-1	-1	-1
17	1	1	-1	1	1	-1	-1	1	1	1	1	-1	1	-1	1	-1	-1	-1	-1
18	1	-1	1	1	-1	-1	1	1	1	1	-1	1	-1	1	-1	-1	-1	-1	1
19	-1	1	1	-1	-1	1	1	1	1	-1	1	-1	1	-1	-1	-1	-1	1	1
20	-1	-1	-1	-1	-1	-1	-1	-1	-1	-1	-1	-1	-1	-1	-1	-1	-1	-1	-1

The levels of the high and low parameter values were chosen such that changing each parameter from high to low resulted in a similar overall change (in terms of magnitude) in the model's shape. For example, the inferior surface angle (θ_{1c}) levels were determined as follows. First, all parameters were set to their baseline values. Then, keeping all other parameters at their baseline values, high and low θ_{1c} values that yielded 0.15 mm displacement of a point on the glottal entrance radius position from its original position were determined (yielding a total displacement of 0.3 mm of the point position when alternating between high and low settings of parameter θ_{1c}). This was repeated for all parameters. The total displacement value of 0.3 mm was selected due to geometric restrictions (i.e., higher displacement values resulted in geometrically infeasible body layer definitions).

The profile of the model was defined using basic geometric and linear algebra principles. An Excel spreadsheet was used to draw each model based on input parameters. The shape of the vocal fold was checked to make sure that no parameters were being violated (e.g., excessive length and height, tangency between radii and straight surfaces, etc.). All 20 run profiles were compiled in Excel and proved to be accurate. (One exception to this was Run 4, for which the high value of r_{2b} = 0.66 mm was not feasible, and was thus reduced to 0.56 mm. For this run, proper weighting of the value was taken into consideration when calculating the effects. This modification was deemed to be acceptable since the results showed that overall, r_{2b} was insignificant in the measured effects.) Profiles of various geometrically defined models, including the baseline model, are provided in Fig. 4.2.

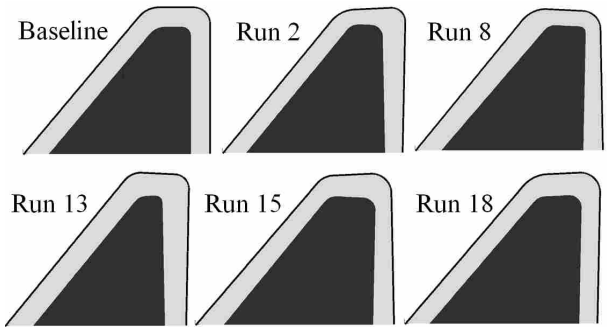

Figure 4.2: Illustration of two-layer (cover - gray; body - black) models used in select runs.

4.2.3 Computational model

A computational model was used to simulate the flow-induced vibratory motion of a two-dimensional representation of a previously described experimental setup [19, 40] (see Fig. 4.3; note the use of symmetry for computational efficiency). The experimental setup consisted of a compressed air source supplying air into a plenum-tube-synthetic vocal fold model series. No vocal tract was included; the supraglottal flow was thus a free jet.

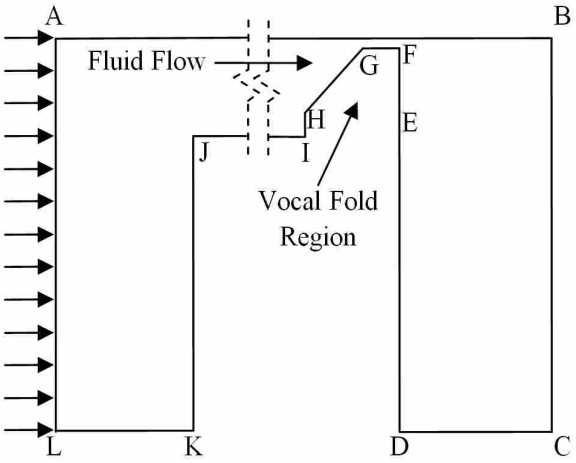

Figure 4.3: Computational fluid domain (not to scale). See Table 4.1 for geometric and other boundary condition settings. Model is symmetric about line AB.

Table 4.3: Computational fluid domain line lengths and boundary conditions.

Line Segment	Length (m)	Boundary Type
AB	0.9767	Slip Wall
BC	0.1524	Zero Pressure
CD	0.1000	Zero Pressure
DE	0.1439	Wall
EF	0.0084	FSI
FG	0.0021	FSI
GH	0.0114	FSI
HI	0.0042	FSI
IJ	0.5588	Wall
JK	0.1397	Wall
KL	0.3080	Wall
AK	0.1524	Fixed pressure (900 Pa)

The commercial finite element software ADINA, designed specifically for systems that exhibit fluid-structure interactions and that has been used previously in voice research [7], was used. The computational model consisted of distinct but fully-coupled solid and fluid domains, each of which is described below.

The solid domain included different materials for the model body and cover layers (see Fig. 4.4). A hyperelastic Ogden material allowed for large strain. The Young's modulus values for the body and cover layers were approximately 15 kPa and 5 kPa, respectively. The density was 1070 kg/m^3 for each layer. The Rayleigh damping scheme was used, with damping coefficients of $\alpha = 1.948$ and $\beta = 2.866\times10^{-4}$. These correspond to damping ratios of approximately 0.018 and 0.029 at frequencies of 120 and 200 Hz, respectively. A zero displacement boundary condition was applied to the lateral edge of the solid domain. A fluid-structure interaction boundary condition was applied to the remaining borders of the solid domain (i.e., those that were in contact with the fluid domain). This boundary condition enforced consistent displacement and stress in both fluid and solid domains along the interface.

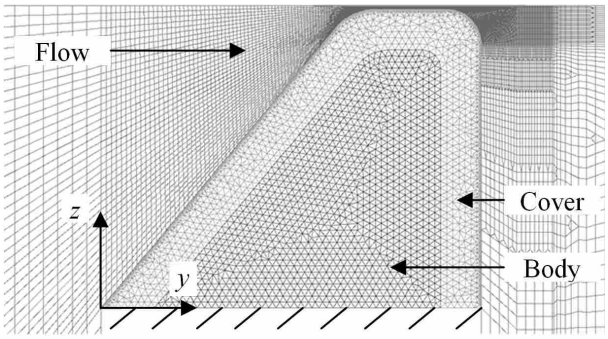

Figure 4.4: Meshed solid and fluid domains.

The fluid (airflow) domain (see Figs. 4.3 and 4.4) was governed using the unsteady, viscous, incompressible Navier-Stokes momentum equations coupled with a slightly compressible form of the continuity equation. The air density, viscosity, and bulk modulus values were 1.2 kg/m^3, 1.8×10^{-5} Pa·s, and 1.41×10^5 Pa, respectively. The fluid domain dimensions and boundary conditions are given in Table 4.3. The initial glottal gap width was 0.2 mm.

The slightly compressible fluid model was used to enable modeling of acoustic feedback in the subglottic section. In the slightly compressible algorithm [62], a compressible density, ρ_m, is defined as the incompressible density ρ at a pressure of $p = 0$, modified by the ratio of pressure, p, to bulk modulus, κ:

$$\rho_m = \rho\left(1+\frac{p}{\kappa}\right) \tag{4.1}$$

This compressible density replaces the incompressible density in the continuity equation:

$$\frac{\rho}{\kappa}\left(\frac{\partial p}{\partial t}+v\cdot\nabla p\right)+\rho_m\nabla\cdot v=0 \tag{4.2}$$

where t and v denote time and velocity, respectively.

In this formulation there is no need to use the energy equation. Compared with a fully-compressible algorithm, this approach is more computationally efficient [63], and convergence may be more easily obtained for the low Mach numbers typical of voice production. It is noted that this approach is valid only for $\frac{p}{\kappa} << 1$. For these simulations, maximum pressure values were around 3 kPa, for maximum $\frac{p}{\kappa}$ ratios of around 0.02, thus satisfying the $\frac{p}{\kappa} << 1$ condition.

Figure 4.4 shows the meshes in both domains. Model verification was performed to ensure that the solution was reasonably independent of time step size and mesh density. The time step was decreased from 2.5×10^{-5} s to 6.25×10^{-6} s; the solution converged at 1.25×10^{-5} s. The element mesh density around the vocal folds ranged from 20 by 40 up to 80 by 160 (these numbers represent a ratio of lateral versus vertical elements around the FSI boundary); the solution converged at a mesh density of 40 by 80. Thus, a time step of 1.25×10^{-5} s and a mesh density of 40 by 80 was used in this study.

The fluid domain utilized primarily four-node quadrilateral elements, and consisted of approximately 19,000 nodes. The solid domain used three-node triangular elements, and contained approximately 3,000 nodes. As has been done previously [7], a contact line was used to prevent complete mesh collapse as the solid domain moved medially. This contact line was placed such that the minimum allowable glottal gap width was 0.05 mm. An example of the script files used to define the geometry, fluid and solid domain of one of the models is provided in Appendix B.

4.2.4 Yield calculation

To estimate the effect of each of the 13 geometric parameters on the model's response, various output measures, denoted here as yields, were obtained. These included the following (described in detail below; see also Table 4.4): flow-induced vibration frequency (f_{FIV}), changes

in lateral glottal width (Δd), flow rate (Δq), and intraglottal angle ($\Delta\alpha$), and lateral phase delay ($\Delta\phi/T$, where T is the vertical glottal thickness). Similar measures of lateral phase delay have been used by Titze et al. [64] and Boessenecker et al. [3] to quantify mucosal wave-like motion.

Table 4.4: Nomenclature of measured yields.

Yield	**Definition**
f_{FIV} (Hz)	Flow-induced vibration frequency
Δd (mm)	Difference between min/max glottal width
Δq (m^3/s)	Difference between min/max flow rate
$\Delta\alpha$ ($^\circ$)	Difference between min/max intraglottal angle
$\Delta\phi/T$ ($^\circ$/mm)	Lateral phase delay between points near entrance and exit radii
f_{MOD} (Hz)	Second *in vacuo* modal frequency

These five measures were calculated for each case using Excel and Ensight (Appendix C) after steady-state oscillation was reached. The flow-induced vibration frequency (f_{FIV}) was measured by tracking the "entrance point" position (see Fig. 4.1). Measures of Δd, Δq, $\Delta\alpha$, and $\Delta\phi/T$ are visually portrayed in Fig. 4.5, in which three different simulation results (comparing the baseline model to a "good" and "bad" model) are shown. The difference in minimal glottal width (Δd) was measured by taking the net difference between high and low values of the minimum glottal gap (z-direction; see coordinate system in Fig. 4.4) over time. The change in flow rate (Δq) was measured by integrating the velocity profile just downstream of the model, multiplying by 0.017 cm (around the length of the average adult male's vocal folds [65]), and taking the difference between high and low flow rates over time. The change in intraglottal angle ($\Delta\alpha$) was measured by tracking the y- and z-locations of the entrance and exit points and taking the net difference between the low and high angle between them. The phase delay ($\Delta\phi/T$) was measured by tracking the

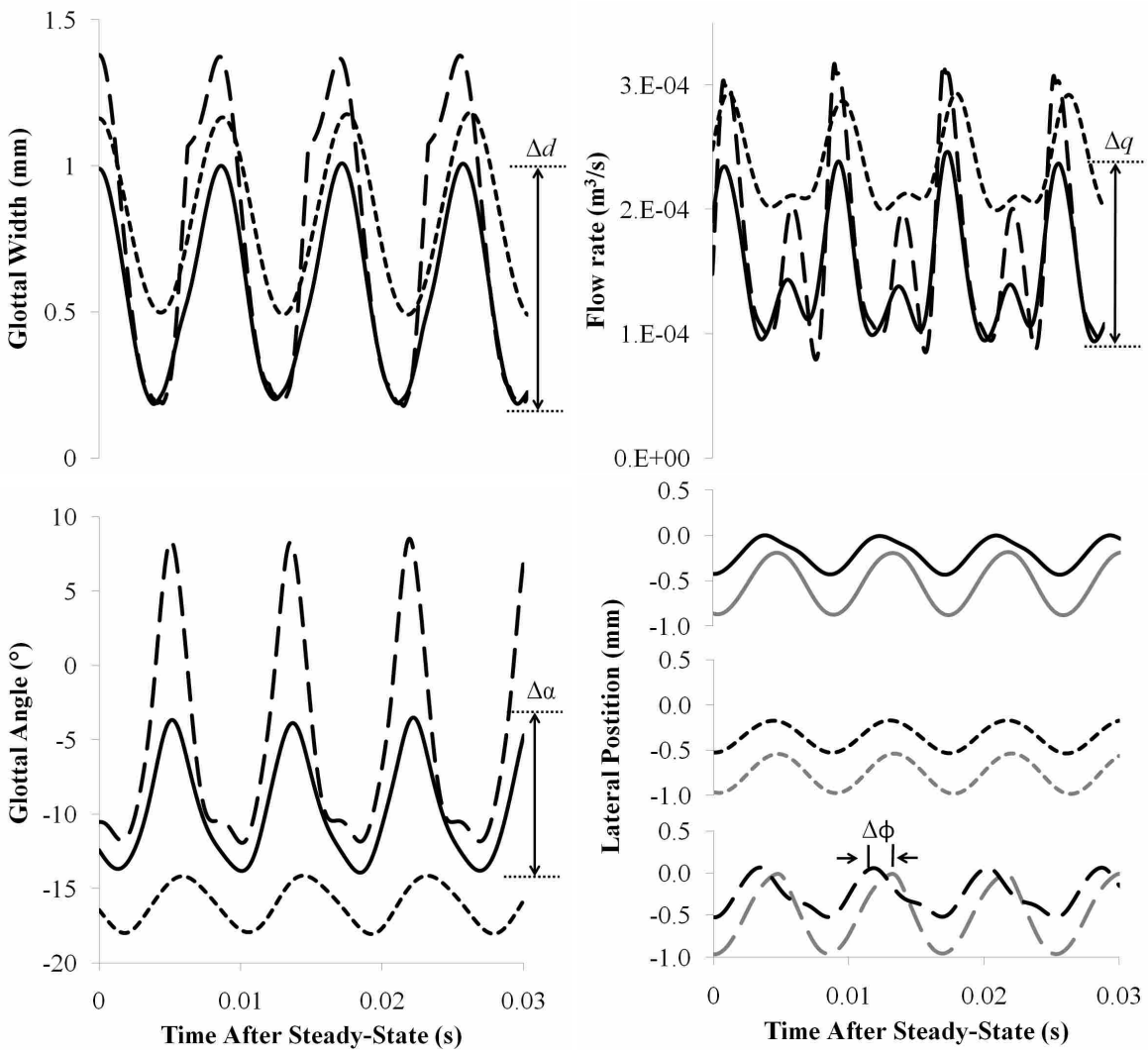

Figure 4.5: Predicted yields for the baseline (solid), Run 13 (short dashes), and Run 18 (long dashes) models. In the lower right plot, black and gray colors denote entrance and exit point positions, respectively (see Fig. 1).

entrance and exit z-locations over time, taking the difference in time between peak values, dividing by the period, multiplying by 360°, and dividing by the vertical glottal thickness (T).

The effect of each parameter was calculated as follows. Each parameter's yields from runs with a specified 'high' value were averaged. Each parameter's yields from runs with a specified 'low' value were also averaged, subtracted from the 'high' yield average, and then normalized. A resulting value relatively close to zero indicated that even though the parameter levels may have

been changing, the overall yield did not vary; i.e., the parameter had a minimal effect on model response. A value close to +1 or -1 meant that a particular parameter had a high impact on the measured yield. A positive effect meant that increasing that parameter's value increased the yield, while a negative effect meant the opposite.

Statistical p-values were estimated for each parameter at each measured yield. A standard $\alpha = 0.5$ value was used. Since there was no anticipated variation in the calculated yields (due to the use of computational analysis), a Monte Carlo technique (implemented by the commercial statistical software package JMP) was used to provide a pseudo-standard error (PSE) which allowed for calculated p-values. p-values less than 0.05 were considered to be significant; p-values less than 0.10 but greater than 0.05 were considered to be marginally significant.

In addition to these yields, animations of the simulated model motion were created for visual inspection. Finally, *in vacuo* modal analysis was performed on each vocal fold model (also using ADINA). These modal analysis results were not used to estimate which parameters were important in governing the model motion, but were used to assist in interpreting the results. As discussed below, the second modal frequency, f_{MOD}, was of particular interest.

4.3 Results and discussion

Table 4.5 lists the six calculated yields from each of the 20 runs; Fig. 4.6 contains plots of the normalized effects of each parameter per yield, with significant and marginally significant p-values denoted.

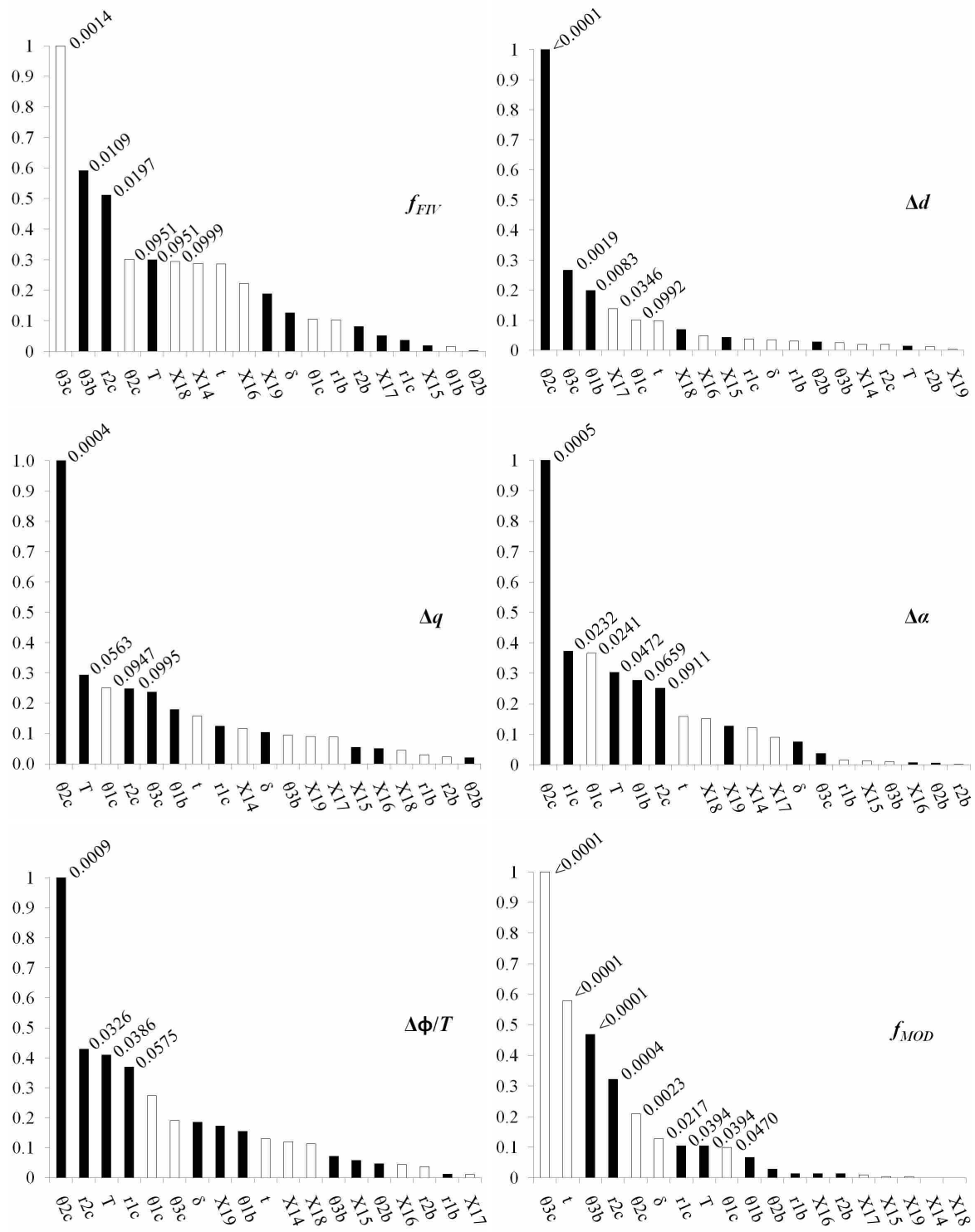

Figure 4.6: Normalized yield effects: flow-induced vibration frequency (f_{FIV}), change in glottal width (Δd), change in flow rate (Δq), change in intraglottal angle ($\Delta\alpha$), lateral phase delay ($\Delta\phi/T$), and second *in vacuo* modal vibration frequency (f_{MOD}). Filled bars represent positive effects; empty bars represent negative effects. Numbers above bars represent individual p-values.

Table 4.5: Yield values for each run.

Run	f_{FIV} (Hz)	Δd (mm)	Δq (m^3/s)	$\Delta\alpha$ (°)	$\Delta\phi/T$ (°/mm)	f_{MOD} (Hz)
0	117.8	0.829	1.53E-04	10.5	18.5	116.8
1	119.2	1.045	1.89E-04	15.2	24.9	120.4
2	115.9	1.264	2.40E-04	20.0	26.2	114.9
3	121.3	0.724	1.17E-04	7.1	14.4	122.6
4	114.5	1.120	2.01E-04	10.5	17.5	115.1
5	118.2	0.715	1.31E-04	10.4	16.7	119.1
6	118.8	1.023	2.01E-04	16.7	28.6	117.0
7	119.1	0.757	1.53E-04	13.2	21.2	119.9
8	121.5	0.503	0.92E-04	7.3	18.0	120.7
9	116.2	0.732	1.01E-04	4.5	8.5	114.1
10	117.8	0.694	1.96E-04	12.7	21.7	117.0
11	120.0	1.061	1.96E-04	16.0	26.6	121.1
12	113.8	1.223	2.17E-04	16.3	20.8	114.6
13	115.2	0.712	0.98E-04	4.1	8.1	112.1
14	115.9	1.040	1.91E-04	11.0	19.4	115.6
15	122.3	1.099	2.48E-04	19.7	32.5	119.4
16	118.6	0.861	1.62E-04	9.7	16.2	118.4
17	117.5	0.733	1.29E-04	7.3	13.0	115.2
18	118.8	1.202	2.38E-04	20.6	30.3	117.5
19	116.1	1.253	2.54E-04	20.0	28.7	114.1
20	119.3	0.711	1.07E-04	6.0	9.3	119.4

4.3.1 Flow-induced vibration frequency

Flow-induced vibration frequency (f_{FIV}) of the ranged from 113 to 122 Hz, all of which are within the acceptable range of male phonation. The parameter that had the largest effect was the cover layer superior angle (θ_{3c}), which had a negative effect. Other significant parameters were the body layer superior angle (θ_{3b}) and the cover exit radius (r_{2c}), both of which had positive effects. Marginally significant parameters were θ_{2c}, T, and X18 (an unknown interaction).

The flow-induced vibration profiles from three runs through one cycle of vibration are showed in Fig. 4.7. Cases displayed include the baseline model (Run 0) and Runs 13 (bad model) and 18 (good model). For the baseline model, the cover and body layer prephonatory intraglottal angles were 0°. Its movement was similar to previous similarly-defined synthetic mod-

els (e.g., [54]). The vibration frequency was 117 Hz. There was minimal presence of mucosal wave-like motion, and the glottal profile stayed primarily divergent throughout the cycle. Run 13 produced similar results as the baseline model, with no evidence of mucosal wave-like motion and consistently divergent glottal profile throughout the cycle. Its cover layer intraglottal angle (θ_{2c}) was set at its low value of -2.75° (divergent). As seen in Fig. 4.7, Run 18 showed improvement in motion over that of both the Run 0 and Run 13 models. The intraglottal angle altered between convergent during opening (t/T = 4/6 to 5/6) and divergent during closing (t/T = 1/6 to 3/6). This attribute was nonexistent in the Run 0 and Run 13 models (see also Fig. 4.5), and is also a characteristic of true vocal fold motion. A common feature between Run 18 and other cases with similar convergent-divergent motion was that the cover layer intraglottal angle (θ_{2c}) was set to its high value of 2.75° (convergent).

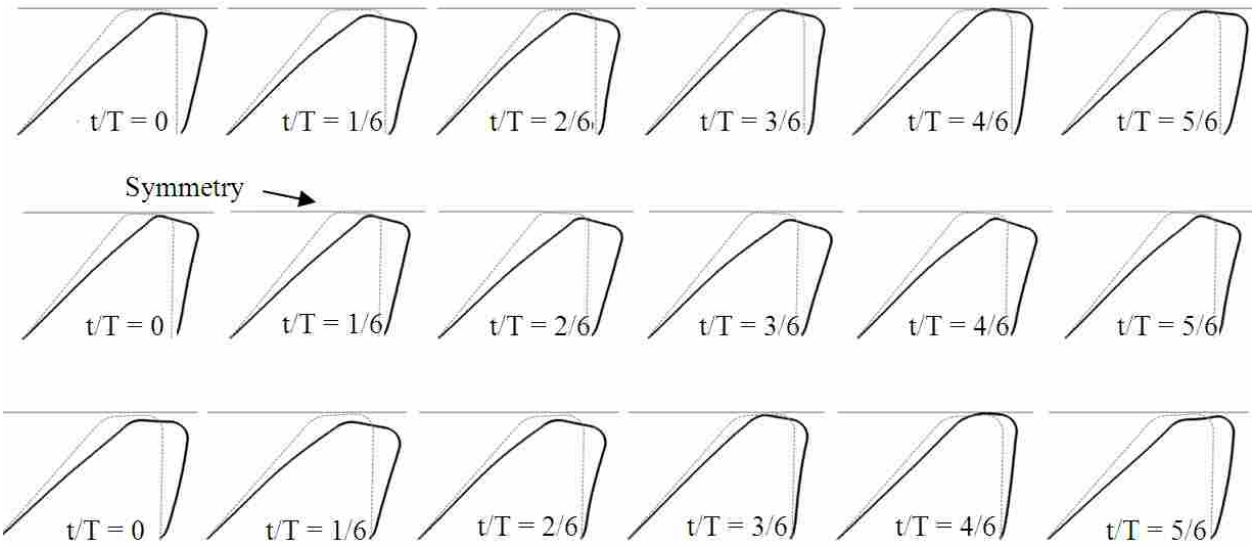

Figure 4.7: Profiles of different parametric models of the vocal folds over one oscillation cycle. The baseline model (Run 0, top), Run 13 (middle) and Run 18 (bottom) are all shown. Gray profiles represent each model's original position.

The significance of the cover superior angle in influencing f_{FIV} is related to its role in governing model stiffness. The first and second mode shapes for Run 18 are shown in Fig. 4.8. The first mode features primarily inferior-superior motion, whereas the second mode also features alternating convergent-divergent motion. The first modal frequencies were around 50 Hz, whereas the second modal frequencies (f_{MOD}) were very close to those of the flow-induced vibration frequency. This is evident in Fig. 4.9, where a strong correlation between f_{FIV} and f_{MOD} is seen. This is likely due to acoustic coupling of the subglottic system with the model's second mode of vibration (Zhang et al., 2006b; 2009). As seen in Fig. 4.6, the second mode of vibration (f_{MOD}) was most influenced by θ_{3c}, the same parameter that most significantly influenced f_{FIV}. Decreasing θ_{3c} led to a larger inferior-superior base length, which in turn increased the model stiffness. This caused f_{MOD} to increase, and by virtue of the acoustic coupling, f_{FIV}.

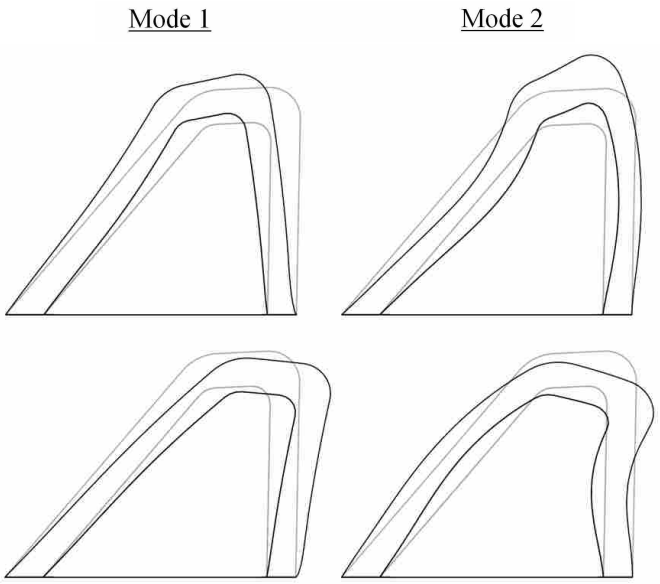

Figure 4.8: Mode shapes 1 (left) and 2 (right). Light gray lines denote undeformed shapes.

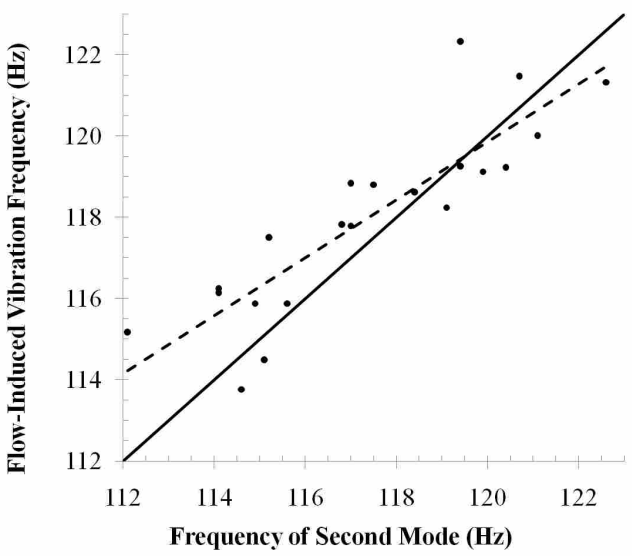

Figure 4.9: Relationship between flow-induced vibration frequency (f_{FIV}) and the second modal frequency (f_{MOD}) of the solid models. Hypothetical one-to-one relationship (solid line) and actual data trend line (dashed line, $R^2 = 0.75$) are shown.

4.3.2 Glottal width, flow rate, intraglottal angle, and phase delay

The other four measured yields (change in glottal width, Δd; change in flow rate, Δq; change in intraglottal angle, $\Delta\alpha$; and phase delay, $\Delta\phi/T$) all exhibited somewhat similar trends in terms of significant parameters and were more strongly influenced by the cover intraglottal angle (θ_{2c}) than by any other yield.

The glottal width (Δd) was mainly influenced by θ_{2c}, which had a positive effect. The largest differences in the glottal width were around 1.4 mm, which is similar to previous values measured using excised human hemilarynges [2, 3]. Only one body layer geometry (θ_{1b}) had a significant effect on Δd. Other significant and marginally significant parameters include θ_{3c}, X17, and θ_{1c}.

Unknown interactions of parameters appear to be somewhat significant only in Δd and f_{FIV} yields (see Fig. 4.6). As mentioned above, the Plackett-Burman design has interactions con-

founded in the main effects. In order to understand the magnitude of the effect that interactions play in governing f_{FIV} and Δd, further parametric studies considering the most influential parameters and their interactions would be necessary.

The change in flow rate (Δq) was mainly influenced by θ_{2c} (positive effect). Other parameters that affected Δq were T, θ_{1c}, and r_{2c}. This is important since changes in flow rate are strongly correlated with sound production. The change in intraglottal angle ($\Delta\alpha$) was also most strongly influenced by θ_{2c}, which had a positive effect. Other parameters that effected $\Delta\alpha$ include r_{1c}, θ_{1c}, T, θ_{1b}, and r_{2c}. Adjusting these parameters for large $\Delta\alpha$ is desirable for generating alternating convergent-divergent motion. For phase delay ($\Delta\phi/T$), other significant and marginally significant parameters included r_{2c}, T, and r_{1c}. All of these geometries had a positive effect. Relative to the baseline model, increased phase delays are desirable; hence, increased values of θ_{2c} (more convergent profile), r_{2c}, T, and r_{1c} are recommended for improving the phase delay.

4.3.3 Overall parameter significance

To quantify the overall effect of each parameter on vocal fold movement, the geometric parameters for Δd, Δq, $\Delta\alpha$, and $\Delta\phi/T$ were ranked for each yield (i.e., assigned a number 1-19), summed, and normalized. These overall rankings are shown in Fig. 4.10, and provide a graphical representation of the parameters that exerted the greatest overall effect on vocal fold motion. The cover medial angle profile θ_{2c} is clearly the most significant factor overall. It had the greatest effect (positive) on all calculated yields, except for the flow-induced vibration and second modal frequencies. Altering the intraglottal angle to have a convergent prephonatory profile significantly improves model motion in terms of generating alternating convergent-divergent motion and mucosal wave-like motion (phase delay). The influence of θ_{2c} is followed by θ_{1c}, θ_{1b}, r_{1c}, θ_{3c}, T, r_{2c}

(all of which, except for θ_{1b}, govern the cover layer profile), δ and t (which govern cover layer thickness), and other interactions and body layer geometries.

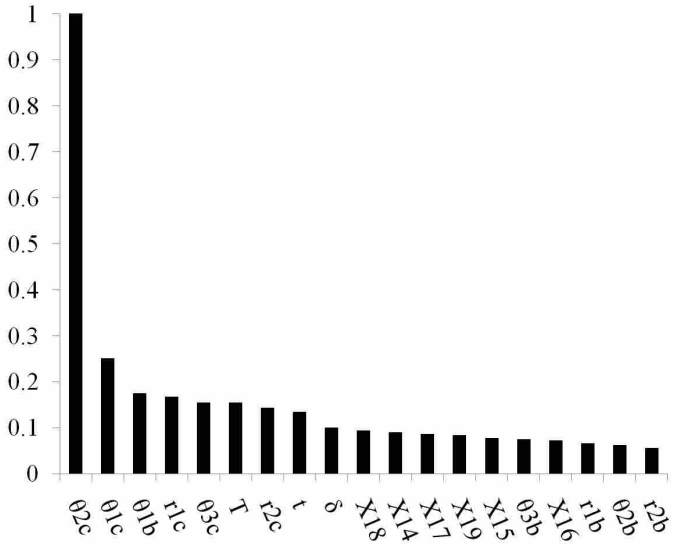

Figure 4.10: Normalized summed effects for Δd, Δq, $\Delta\alpha$, and $\Delta\phi/T$.

The other two model cover layer angles (θ_{1c} and θ_{3c}) also had an effect on model motion, though not nearly as profound as θ_{2c}. θ_{1c} had a negative effect on calculated yields, including Δq, $\Delta\alpha$, and $\Delta\phi/T$. θ_{3c} had a positive effect on Δd and a negative effect on f_{FIV} and f_{MOD}.

The entrance and exit radii (r_{1c} and r_{2c}) showed similar effects on all six yields. Increasing either would provide an increase in Δq, $\Delta\alpha$, and $\Delta\phi/T$. Since large glottal angle differences and changes in flow rate are desirable for improving the motion and increasing sound production, relatively larger entrance and exit edge radii may be advisable.

Another somewhat influential geometric feature was the glottal thickness (T), which had a significant or marginally significant positive effect on Δq, $\Delta\alpha$, and $\Delta\phi/T$. Increasing T had a significant impact on the phase difference between the inferior-superior portions of the glottis

(similar to θ_{2c}), suggesting that increasing T may provide improved mucosal wave-like motion for physical modeling.

It is interesting to note that the body dimensions did not have a major effect on any of the measured yields, with the exception of θ_{1b}, which had a positive effect on Δd and $\Delta\alpha$. Some of the unknown interactions had higher significance than the body parameters. Therefore, the interactions of the cover layer geometries and θ_{1b} may prove to be important to model motion and should therefore be investigated.

4.4 Conclusions

In this chapter, the influence of geometric parameters on the flow-induced vibration of a simplified vocal fold model was discussed. It was shown that simplified models have the potential to be altered geometrically for more favorable (realistic) vocal fold model movement.

Prior research has shown that the intraglottal angle, vocal fold depth, and vocal fold length significantly influence vocal fold motion [8, 12]. The present work considered more geometric attributes of a simplified model and showed that the geometric parameters that play the most important role in affecting the flow-induced vibration frequency, glottal area, flow rate, change in glottal angle during phonation, phase delay, and second modal frequency were the cover layer geometries (foremost, the intraglottal cover layer angle, θ_{2c}, followed by θ_{1c}, r_{1c}, θ_{3c}, T, r_{2c}, and t), and the inferior glottal angle of the body (θ_{1b}).

A key aspect of vocal fold movement is the mucosal wave. Previous geometrically-simplified synthetic models have not displayed this type of motion. The phase delay measurement provided a quantitative assessment of mucosal wave-like motion; the phase delays calculated in this work are similar to data obtained using excised human larynges [3]. Although an optimized model was not

created in this study, the results show the potential for creating a model that has at least a 34.5°/mm phase delay (lateral $\Delta\phi$ values calculated by Boessenecker et al. reached a maximum of 89°, which correspond to a $\Delta\phi/T$ value of approximately 44.5°/mm [3]). Therefore, previously limited mucosal wave-like features on simplified models may be obtainable if these geometric definitions of the cover layer are incorporated. Further, the present work shows that using a convergent profile will increase intraglottal phase delays and alternating convergent-divergent glottal angles that may more accurately simulate human vocal fold movement.

The results from this design-of-experiment do not reflect the level of influence of each parameter in its entirety. Therefore, recommended future work includes a full factorial statistical analysis, which will provide information on the interaction of substantial parameters. Also, it would prove beneficial to perform physical tests on these simplified models with improved geometric features suggested above to validate the computational data provided. Such analysis and testing is suggested so that specific geometric values for each parameter may be recommended. Further studies over a wider range of parameter values, including three-dimensional geometric parameters, and development of anisotropic modeling materials are also strongly recommended.

CHAPTER 5. CONCLUSIONS AND FUTURE WORK

Knowledge of vocal fold vibratory characteristics is pivotal in assessing voice disorders. In order to contribute to an improved understanding of voice production, this thesis research has been conducted, which included investigations into the role of material and geometric parameters on the vibratory response of vocal fold models. An extension of the vocal fold model introduced by Thomson et al. [7] was used for physical and computational testing of vocal fold functionality, and various output parameters (such as pressure, frequency, flow rate, glottal area, etc.) were used to quantify differences in model motion.

5.1 Influence of asymmetric stiffness on synthetic vocal fold model vibration (Chapter 2)

5.1.1 Conclusions

Asymmetry was introduced into synthetic models of the vocal folds by varying the relative stiffness between the paired models, thus allowing for a controlled study of the influence of material-only asymmetry on vocal fold vibration and glottal aerodynamics. This was done using high-speed videokymography and particle image velocimetry (PIV).

It was shown that asymmetry in the models' stiffness reduced glottal width by 1.25 mm, introduced phase differences between the left and right folds up to 90°, increased onset pressure by almost 300%, and contributed to asymmetric glottal velocity profiles. These suggest that from

a phonatory perspective, close matching of left-right stiffness is desired, since increased stiffness of one fold (that is, a greater degree of asymmetry) appears to result in:

(1) smaller glottal area;

(2) higher onset pressure resulting in greater required phonatory effort;

(3) incomplete glottal closure, resulting in a breathy voice; and

(4) jet skewing, potentially contributing to broadband sound production.

5.1.2 Future work

Several areas of future work on asymmetric modeling are here suggested. Firstly, comparison should be made between these results and those obtained using a model with a supraglottal vocal tract and false vocal folds. While numerous synthetic and excised larynx studies have been performed without a vocal tract - usually for instrumentation access - it has been shown (e.g., [20, 39]) that a vocal tract can directly influence the glottal jet. The vocal tract can also present an acoustic loading, thus potentially forming strong acoustic coupling between the vocal folds and the vocal tract [39]. Other areas of suggested work include: similar studies using computational models for more precise control over stiffness and geometry; further investigation into the effects of increased phase difference in asymmetric vocal fold vibration, including the presence or absence of irregular phonation as evidenced by slightly different frequencies; and development and testing of improved models (e.g., with nonlinear stress-strain characteristics and less idealized geometry) that more closely mimic human vocal folds.

5.2 Idealized vs. MRI-based synthetic vocal fold models (Chapter 3)

5.2.1 Conclusions

The flow-induced responses of two models of differing geometries were characterized in order to show that more life-like motion can be achieved when using more realistic geometry. This was done by comparing the flow-induced responses of two synthetic, self-oscillating models of matching material properties but differing geometries. One model was based on an idealized geometry (the so-called "M5" geometry commonly used by voice researchers). The other was based on geometry derived from magnetic resonance imaging (MRI) data [44].

The flow-induced responses of the MRI-based synthetic models showed remarkable differences compared with those of the M5 models. Improvements include:

(1) less vertical motion (by 1.77 mm);

(2) apparently more typical alternating convergent-divergent glottal profile pattern; and

(3) evidence of mucosal wave-like motion.

Since fabrication methods for both the M5 and MRI models were similar, the differences between the two models' motions were primarily attributable to differences in geometry. It is, of course, expected that different geometries will yield different vibration patterns. What is significant, however, is that the MRI model showed important improvements in yielding more life-like motion than the M5 model while using the same materials. It is hoped that these findings will stimulate and provide direction for research efforts aimed towards developing improved synthetic vocal fold models for human voice production research.

5.2.2 Future work

The role of material properties in governing vocal fold model response must also continue to be explored; synthetic model materials reported in the literature have typically been isotropic and linearly elastic, in contrast with the anisotropic, nonlinear material properties of vocal fold tissue. The development of more realistic synthetic materials will be an important step towards creating more life-like vocal fold models.

5.3 Influence of geometric features on vocal fold model vibration (Chapter 4)

5.3.1 Conclusions

The influence of geometric parameters on the flow-induced vibration of a simplified vocal fold model was analyzed. It was shown that simplified models have the potential to be altered geometrically for more favorable (realistic) vocal fold model movement. The geometric parameters that exerted the most significant influence on vibratory parameters (change in glottal width, change in flow rate, change in glottal angle during phonation, and phase delay) were the cover layer geometries (primarily that of the intraglottal cover layer angle, θ_{2c}) and the inferior glottal angle of the body (θ_{1b}). It was shown that previously limited mucosal wave-like features on simplified models may be obtainable using proper cover layer geometric definitions. Furthermore, increasing the glottal convergence angle also provides alternating convergent-divergent glottal angles during model oscillation.

5.3.2 Future work

A full factorial statistical analysis will provide information on the interaction of significant parameters, as well as provide a newly "idealized," yet still geometrically simple model to be used

in future vocal fold modeling research. Also, physical tests on simplified models with improved geometric features should be performed to validate these results. Also, a study investigating single variables and their influence on model motion is suggested so that specific geometric definitions of each parameter may be assigned.

5.4 Additional work

There remain significant open questions in the general area of voice research. Below are a few suggestions for future work that may prove to be beneficial in advancing the community's understanding of voice production mechanics:

- The vocal folds are generally comprised of three major tissue layers, and yet the models used in this study (both computational and physical) and many other published studies use only two layers. The most neglected layers are the epithelial (or outer) and ligament layers. The epithelial layer is difficult to manufacture and implement due to its small thickness (around 0.05 to 0.1 mm). However, if these layers could be incorporated, synthetic models may yield more life-like characteristics of vocal fold movement.

- The vocal folds have a surface liquid that seems to affect vocal fold movement. Incorporating this liquid into synthetic models may also prove to be beneficial.

- Current MRI data does not provide sufficiently high resolution images for voice research. Methods to provide higher resolution upon MRI image capture (such as coils designed to provide better focus on the area of the vocal tract) may result in overall better models of the vocal folds, and may also provide more detailed information about the entire vocal tract.

- The MRI-based model developed in this work showed promise in vibrating similar to true vocal folds. However, the MRI-based model's primary shortcoming was the high onset pressure. Methods to decrease this onset pressure should be explored. It is conceivable that in the future, a patient diagnosed with a voice disorder could have an MRI scan of their vocal folds, and corresponding models could be built and tested to observe dissimilarities with healthy vocal folds.

- Two-dimensional computational models were used in this research. Expanding to a third dimension would allow for investigations of models that do not have uniform anterior-posterior (coronal) cross-sections.

- Since geometric features of the larynx are central to the vocal fold's flow-induced response, development of a dynamic model that uses all supporting cartilage around the vocal folds, as well as muscle contraction techniques, may provide more realistic modeling conditions.

REFERENCES

[1] NIDCD, 2010. `http://www.nidcd.nih.gov/health/statistics/vsl.asp`, May. 1

[2] Doellinger, M., and Berry, D. A., 2006. "Visualization and quantification of the medial surface dynamics of an excised human vocal fold during phonation." *Journal of Voice,* **20**(3), pp. 401 – 413. 5, 64

[3] Boessenecker, A., Berry, D. A., Lohscheller, J., Eysholdt, U., and Doellinger, M., 2007. "Mucosal wave properties of a human vocal fold." *Acta Acustica united with Acustica,* **93**, pp. 815–823. 5, 57, 64, 67, 68

[4] Titze, I. R., 1976. "On the mechanics of vocal fold vibration." *Journal of the Acoustical Society of America,* **60**, pp. 1366–1380. 5

[5] Berry, D. A., and Titze, I. R., 1996. "Normal modes in a continuum model of vocal fold tissues." *Journal of the Acoustical Society of America,* **100**(5), November, pp. 3345–3354. 5

[6] Alipour, F., Berry, D. A., and Titze, I. R., 2000. "A finite-element model of vocal-fold vibration." *Journal of the Acoustical Society of America,* **108**(6), December, pp. 3003–3012. 5, 19

[7] Thomson, S. L., Mongeau, L., and Frankel, S. H., 2005. "Aerodynamic transfer of energy to the vocal folds." *Journal of the Acoustical Society of America,* **118**(3), pp. 1689–1700. 5, 6, 7, 13, 19, 46, 54, 56, 69

[8] Cook, D. D., and Mongeau, L., 2007. "Sensitivity of a continuum vocal fold model to geometric parameters, constraints, and boundary conditions." *The Journal of the Acoustical Society of America,* **121**(4), pp. 2247–2253. 5, 47, 48, 67

[9] Ishizaka, K., and Flanagan, J. L., 1972. "Synthesis of voiced sounds from a two-mass model of the vocal cords." *Bell System Technical Journal,* **51**(1), pp. 1233–1268. 5, 9, 12

[10] Hunter, E. J., Titze, I. R., and Alipour, F., 2004. "A three-dimensional model of vocal fold abduction/adduction." *Journal of the Acoustical Society of America,* **115**, pp. 1747–1759. 5

[11] Cook, D. D., Nauman, E., and Mongeau, L., 2009. "Ranking vocal fold model parameters by their influence on modal frequencies." *Journal of the Acoustical Society of America,* **126**(4), October, pp. 2002–2010. 5, 42, 47, 48

[12] Zhang, Z., 2009. "Characteristics of phonation onset in a two-layer vocal fold model." *Journal of the Acoustical Society of America,* **125**(2), pp. 1091–1102. 5, 30, 42, 47, 48, 67

[13] Scherer, R. C., Shinwari, D., Witt, K. J. D., Zhang, C., Kucinschi, B. R., and Afjeh, A. A., 2001. "Intraglottal pressure profiles for a symmetric and oblique glottis with a divergence

angle of 10 degrees." *Journal of the Acoustical Society of America,* **109**(4), pp. 1616–1630. 6, 13, 29, 31, 46, 48, 49

[14] Shinwari, D., Scherer, R. C., Witt, K. J. D., and Afjeh, A. A., 2003. "Flow visualization and pressure distributions in a model of the glottis with a symmetric and oblique divergent angle of 10 degrees." *Journal of the Acoustical Society of America,* **113**(1), pp. 487–497. 6, 9, 12, 26

[15] Titze, I., Schmidt, S., and Titze, M., 1995. "Phonation threshold pressure in a physical model of the vocal fold mucosa." *Journal of the Acoustical Society of America,* **97**(5), pp. 3080–3084. 6, 47

[16] Chan, R. W., and Titze, I., 1997. "Further studies of phonation threshold pressure in a physical model of the vocal fold mucosa." *Journal of the Acoustical Society of America,* **101**, pp. 3722–3727. 6

[17] Chan, R. W., and Titze, I., 2006. "Dependence of phonation threshold pressure on vocal tract acoustics and vocal fold tissue mechanics." *Journal of the Acoustical Society of America,* **119**, pp. 2351–2362. 6

[18] Thomson, S. L., 2004. "Fluid-structure interactions within the human layrnx." PhD thesis, Purdue University, West Lafayette, Indiana. 6

[19] Drechsel, J. S., 2007. "Characterization of synthetic, self-oscillating vocal fold models." Master's thesis, Brigham Young University, Provo, UT. 6, 15, 53

[20] Drechsel, J. S., and Thomson, S. L., 2008. "Influence of supraglottal structures on the glottal jet exiting a two-layer synthetic, self-oscillating vocal fold model." *Journal of the Acoustical Society of America,* **123**(6), June, pp. 4434–4445. 6, 7, 13, 19, 27, 28, 46, 70

[21] Zhang, Z., Neubauer, J., and Berry, D. A., 2006. "The influence of subglottal acoustics on laboratory models of phonation." *Journal of the Acoustical Society of America,* **120**(3), pp. 1558–1569. 6, 9, 13, 29, 46

[22] Zhang, Z., Neubauer, J., and Berry, D. A., 2006. "Aerodynamically and acoustically driven modes of vibration in a physical model of the vocal folds." *Journal of the Acoustical Society of America,* **120**(5), pp. 2841–2849. 6, 13, 46

[23] Neubauer, J., Zhang, Z., Miraghaie, R., and Berry, D., 2007. "Coherent structures of the near field flow in a self-oscillating physical model of the vocal folds." *Journal of the Acoustical Society of America,* **121**(2), pp. 1102–1118. 7, 9, 13, 26, 29, 46

[24] Zhang, Y., and Jiang, J. J., 2004. "Chaotic vibrations of a vocal fold model with a unilateral polyp." *Journal of the Acoustical Society of America,* **115**(3), pp. 1266–1269. 9, 12

[25] Khosla, S., Murugappan, S., Paniello, R., Ying, J., and Gutmark, E., 2009. "Role of vortices in voice production: normal versus asymmetric tension." *The Laryngoscope,* **119**(1), pp. 216–221. 9, 12, 26, 27

[26] Popolo, P. S., and Titze, I. R., 2008. "Qualification of a quantitative laryngeal imaging system using videostroboscopy and videokymography." *Annals of Otology, Rhinology, and Laryngology,* **117**(6), pp. 404–412. 9, 29

[27] Hirano, M., Kurita, S., Yukizane, K., and Hibi, S., 1989. "Asymmetry of the laryngeal framework: a morphologic study of cadaver larynges." *Annals of Otology, Rhinology, and Laryngology,* **98**(2), April, pp. 135–140. 11

[28] Thibeault, S. L., Gray, S. D., Bless, D. M., Chan, R. W., and Ford, C. N., 2002. "Histologic and rheologic characterization of vocal fold scarring." *Journal of Voice,* **16**(1), pp. 96–104. 12

[29] Hanson, D. G., and Jiang, J. J., 2000. "Diagnosis and management of chronic laryngitis associated with reflux." *The American Journal of Medicine,* **108**(4A), March, pp. 112S–119s. 12

[30] Lee, S. T. S., and Niimi, S., 1990. "Vocal fold sulcus." *The Journal of Laryngology and Otology,* **104**(1), pp. 876–878. 12

[31] Berry, D. A., Zhang, Z., and Neubauer, J., 2006. "Mechanisms of irregular vibration in a physical model of the vocal folds." *Journal of the Acoustical Society of America,* **120**(3), September, pp. EL36–EL42. 12, 13

[32] Hirano, M., and Kakita, Y., 1985. *Speech Science: Recent Advances*., 1 ed., Vol. 1 College-Hill Press, San Diego, CA. 13

[33] Riede, T., Tokuda, I. T., Munger, J. B., and Thomson, S. L., 2007. "Mammalian laryngeal air sacs add variability to the vocal tract impedance: Physical and computational modeling." *Journal of the Acoustical Society of America,* **124**(1), pp. 634–647. 13, 30, 32

[34] Qiu, Q., and Shutte, H. K., 2007. "Real-time kymographic imaging for visualizing human vocal-fold vibratory function." *Review of Scientific Instruments,* **78**(2), pp. 1–6 (024302). 18

[35] Svec, J. G., Frantisek, S., and Schutte, H. K., 2007. "Videokymography in voice disorders: What to look for?." *Annals of Otology, Rhinology, and Laryngology,* **116**(3), pp. 172–180. 18

[36] Chan, R. W., Fu, M., Young, L., and Tirunagari, N., 2007. "Relative contributions of collagen and elastin to elasticity of the vocal fold under tension." *Annals of Biomedical Engineering,* **35**(8), August, pp. 1471–1483. 19, 23, 33

[37] Barney, A., Shadle, C. H., and Davies, P. O. A. L., 1999. "Fluid flow in a dynamic mechanical model of the vocal folds and tract. i. measurements and theory." *Journal of the Acoustical Society of America,* **105**(1), January, pp. 444–455. 20

[38] Zhao, W., Zhang, C., Frankel, S. H., and Mongeau, L., 2002. "Computational aeroacoustics of phonation, part i: Computational methods and sound generation mechanisms." *Journal of the Acoustical Society of America,* **112**(5), pp. 2134–2146. 20

[39] Zhang, Z., Neubauer, J., and Berry, D. A., 2009. "Influence of vocal fold stiffness and acoustic loading on flow-induced vibration of a single-layer vocal fold model." *Journal of Sound and Vibration,* **322**, pp. 299–313. 28, 46, 70

[40] Pickup, B. A., and Thomson, S. L., 2009. "Influence of asymmetric stiffness on the structural and aerodynamic response of synthetic vocal fold models." *Journal of Biomechanics,* **42**, pp. 2219–2225. 30, 31, 32, 46, 53

[41] Li, S., Scherer, R. C., Wan, M., Wang, S., and Wu, H., 2006. "Numerical study of the effects of inferior and superior vocal fold surface angles on vocal fold pressure distributions." *Journal of the Acoustical Society of America,* **119**(5), pp. 3003–3010. 30, 46

[42] Sidlof, P., Svec, J. G., Horaced, J., Vesely, J., Klepacek, I., and Havlik, R., 2008. "Geometry of human vocal folds and glottal channel for mathematical and biomechanical modeling of voice production." *Journal of Biomechanics,* **41**(5), pp. 985–995. 30, 49

[43] Zhang, Z., 2008. "Influence of flow separation location on phonation onset." *Journal of the Acoustical Society of America,* **124**(3), pp. 1689–1694. 30

[44] Selbie, W. S., Zhang, L., Levine, W. S., and Ludlow, C. L., 1998. "Using joint geometry to determine the motion of the cricoarytenoid joint,." *Journal of the Acoustical Society of America 103(2), 1115-1127,* **103**(3), pp. 1115–1127. 30, 71

[45] Hunter, E. J., and Titze, I. R., 2005. "Individual subject laryngeal dimensions of multiple mammalian species for biomechanical models." *Annals of Otology, Rhinology, and Laryngology,* **114**(10), pp. 809–818. 31

[46] Hunter, E. J., Hunter, L. M., and Titze, I. R., 2005. "Individual subject laryngeal dimensions of multiple mammalian species for biomechanical models: A supplement." *The National Center for Voice and Speech Online Technical Memo*(9). 31

[47] Verdolini, K., Titze, I. R., and Druker, D. G., 1990. "Changes in phonation threshold pressure with induced conditions of hydration." *Journal of Voice,* **4**, pp. 142–151. 35

[48] Verdolini, K., Titze, I. R., and Sandage, M., 1994. "Effect of hydration treatments of laryngeal nodules and polyps and related measures." *Journal of Voice,* **8**, pp. 30–47. 35

[49] Jiang, J., Ng, J., and Hanson, D., 1999. "The effects of rehydration on phonation in excised canine larynges." *Journal of Voice,* **13**(1), pp. 51–59. 35

[50] Hsiao, T. Y., Liu, C. M., Luschei, E. S., and Titze, I. R., 2001. "The effect of cricothyroid muscle action on the relation between subglottal pressure and fundamental frequency in an in vivo canine model." *Journal of Voice,* **15**(2), pp. 187–193. 35

[51] Becker, S., Kniesburges, S., Muller, S., Delgado, A., Link, G., Kaltenbacker, M., and Dollinger, M., 2009. "Flow-structure-acoustic interaction in a human voice model." *Journal of the Acoustical Society of America,* **125**(3), March, pp. 1351–1361. 46

[52] Misun, V., Svancara, P., and Vasek, M., 2010. "Experimental analysis of the characteristics of artificial vocal folds." *Journal of Voice,* **In Press, Corrected Proof**. 46

[53] Bless, D., Hirano, M., and Feder, R., 1987. "Videostroboscopic evaluation of the larynx." *Ear Nose and Throat Journal,* **66**, pp. 289–296. 46

[54] Pickup, B. A., and Thomson, S. L., 2010. "Flow-induced vibratory response of idealized vs. magnetic resonance imaging-based synthetic vocal fold models." *Journal of the Acoustical Society of America,* **In Press, Corrected Proof**. 46, 62

[55] Scherer, R. C., Witt, K. J. D., and Kucinschi, B. R., 2001. "The effect of exit radii on intraglottal pressure distributions in the convergent glottis." *Journal of the Acoustical Society of America,* **110**(5), pp. 2267–2269. 46

[56] Chan, R. W., Titze, I. R., and Titze, M. R., 1997. "Further studies of phonation threshold pressure in a physical model of the vocal fold mucosa." *Journal of the Acoustical Society of America,* **101**(6), June, pp. 3722–3727. 47

[57] Stiblar-Martincic, D., 1997. "Histology of laryngeal mucosa." *Acta Otolaryngology,* **527**, pp. 138–141. 49

[58] Tayama, N., Chan, R. W., Kaga, K., and Titze, I. R., 2002. "Functional definitions of vocal fold geometry for laryngeal biomechanical modeling." *Annals of Otology, Rhinology, and Laryngology,* **111**, pp. 83–92. 49

[59] Alipour, F., Scherer, R. C., and Hollien, H., 2003. "The false vocal folds: Shape and size in frontal view during phonation based on laminagraphic tracings." *Journal of Voice,* **17**, pp. 97–113. 49

[60] Nanayakkara, I., 2005. "Vocal fold superior and inferior angles measured from radiographic images." Master's thesis, Bowling Green State University, Bowling Green, OH. 49

[61] Lawson, J., and Erjavec, J., 2001. *Modern Statistics for Engineering and Quality Improvement*., 1 ed. Duxbury (Wadsworth Group), Pacific Grove, CA. 50

[62] Keshtiban, I., Belblidia, F., and Webster, M., 2009. Compressible flow solvers for low mach number flows - a review. Institute of Non-Newtonian Fluid Mechanics. 55

[63] ADINA, 2005. *ADINA Theory and Modeling Guide Volume 1: Solids and Structures*., 1 ed., Vol. 1 ADINA Research and Development, Inc, Watertown, MA. 56

[64] Titze, I. R., Jiang, J. J., and Hsiao, T., 1993. "Measurement of mucosal wave propagation and vertical phase difference in vocal fold vibration." *Annals of Otology, Rhinology, and Laryngology,* **102**, pp. 58–63. 57

[65] Titze, I. R., 2000. *Principles of Voice Production*., 2 ed. National Center for Voice and Speech, Iowa City, IA. 57

APPENDIX A. MATLAB

MATLAB was utilized to efficiently solve for various factors of model motion, including frequency, glottal area, phase shift, vertical displacement, and glottal width. Also, MATLAB was used to compile videokymographic images (defined in Chapter 2). The following appendices provide the computer code used in this research.

A.1 Calculating frequency, glottal area, phase shift, glottal width, and VKG

```
% Program to read high-speed images and calculate glottal area vs. time and
% position of left & right vocal fold models.  Also, data about frequency
% and phase shift can be derived

% Modified by Brian Pickup, 07 Aug 2009.  Read movie files

clear all
clf; close all
clc

fps= 9000;
ep = 1/2;                                   %Edge Position. 1/2 for midpoint
NFrames = 4000;          %Number of frames kymographed. Change as necessary
MinTime = 0/fps;
MaxTime = (NFrames-1)/fps;
Time=0:1/fps:MaxTime;
extension = 'M5_35_1_00kPa_superior_60fps';               %Change per movie
folder = ['F:\BrianP\HS Camera Videos for M5 MRI comparison\' extension];
filename = [folder '\' extension '.avi'];

%% Calibration

calibfile = ['C:\Documents and Settings\bapickup\My Documents\Research...
                \Thesis\M5 MRI\HS Camera\Calibration\M5_35_superior.tif'];
                                                                %Change per model
calibimage = imshow(calibfile);
calibpixel = ginput(2);
title('Select two points exactly 17 mm apart')
ppmm = sqrt((calibpixel(1,1)-calibpixel(2,1))^2+(calibpixel(1,2)...
                -calibpixel(2,2))^2)/17;

for i=1:NFrames
    % Read images; change path & filename as necessary
        mov = aviread(filename,i);
        Picture = frame2im(mov);

    % Convert image to type double
    C=double(Picture);

    % Select top & bottom of orifice
    if i==1
        figure(1)
```

```
        NonDimTime=0:1/NFrames:(NFrames-1)/NFrames;
        subplot(111)
        image(C/3); axis xy; colormap(gray)
        title(['Select top of orifice'])
        [xtop,ytop]=ginput(1);
        xtop=round(xtop);
        ytop=round(ytop);
        title(['Select bottom of orifice'])
        [xbottom,ybottom]=ginput(1);
        xbottom=round(xbottom);
        ybottom=round(ybottom);
    end

    % Display original image with top as well as bottom orifice lines
    figure(1)
    subplot(311)
    set(gca,'FontSize',10,'FontName','Times');
    image(C/3); axis xy
    shading interp
    colormap gray
    hold on
    plot([0 size(C,2)],[ytop ytop],[0 size(C,2)],[ybottom ybottom])
    plot([xtop,xbottom],[ytop,ybottom],'r--');
    hold off
    title(['' num2str(i) ''])

    % Choose where to perform VKG and measure left/right edge
    H = round((ytop-ybottom)*ep);
%         if i == 1                              %For Arbitrary Point
%             imshow(Picture);
                TITLE('Choose point for Kymographic construction');
%             H = ginput(1);
%             H = round(H(2));
%         else
%         end
    GrayProfile(i,:)=Picture(H,:);

    % Plot intensity vs. horizontal location along row y= H
    subplot(312)
    set(gca,'FontSize',10,'FontName','Times');
    y=H;
    plot(C(y,:))
    xlim([0 1024]); ylim([0 255])

    % Crop C by removing top & bottom
```

```
C(ytop:size(C,1),:)=[];
C(1:ybottom,:)=[];

% Identify all pixels with intensity > Thresh by coloring them green
Thresh=80;
D=im2bw(C/255,Thresh/255); % Convert grayscale image to binary image
E(:,:,1)=C/255; % Red channel
E(:,:,2)=1-D; % Green channel
E(:,:,3)=C/255; % Blue channel

% Find distance to left edge at midpoint
% Find left & right model displacements from centerline at midpoint
% between top & bottom
yMid=H;                % Change # for MRI imaging at max glottal position
xMid=round(0.5*(xbottom+xtop));
if D(yMid,xMid)==0
    Edge1=1; % xMid,yMid coordinate is in glottis
elseif D(yMid,xMid)==1
    Edge1=0; % Either closed or Right VF is to left of midplane
end

Edge1=0;
Edge2=0;
for j=1:size(D,2)
    if Edge1==0
        if D(yMid,j)==0
            LeftEdge(i)=j;
            Edge1=1;
        end
    end
    if Edge1==1
        if D(yMid,j)==1
            RightEdge(i)=j;
            Edge2=1;
            Edge1=0;
        end
    end
end
if Edge2==0
    LeftEdge(i)=nan;
    RightEdge(i)=nan;
end

% Plot orifice, midline, and lines to left & right vocal folds
subplot(313)
```

```
    set(gca,'FontSize',10,'FontName','Times');
    image(E); axis xy; % All pixels with intensity > Thresh are now green
    hold on
    plot([xtop,xbottom],[ytop,ybottom],'r--');
%     plot([xMid,LeftEdge(i)],[yMid,yMid],'r:');
    plot([LeftEdge(i),RightEdge(i)],[yMid,yMid],'b:');
    hold off

    % Calculate orifice area in pixels
    % Note: 1 = outside orifice, 0 = inside orifice
    DArea(i)=size(D,1)*size(D,2)-bwarea(D);

    % Command to update images
    drawnow

end
% Convert area from pixel to mm^2
DArea=DArea/ppmm^2;
% Convert edge locations to mm relative to midplane
LeftEdge=(LeftEdge-xMid)/ppmm;
RightEdge=(RightEdge-xMid)/ppmm;

% Plot area & edge position vs. t/T
figure(2)
subplot(211)
set(gca,'FontSize',10,'FontName','Times');
plot(NonDimTime,DArea)
xlabel('Nondimensional time (t/T)')
ylabel('Glottal area (mm^2)')
% Convert edge locations to mm
subplot(212)
set(gca,'FontSize',10,'FontName','Times');
plot(NonDimTime,LeftEdge,NonDimTime,RightEdge);
xlabel('Nondimensional time (t/T)')
ylabel('Edge position (mm)')

% Format for plotting
figure(1)
set(gcf,'PaperPosition',[1 1 3 3])
hold(gca,'all');
print('-dtiff','-r200','figure1.tif');
figure(2)
set(gca,'FontSize',10,'FontName','Times');
subplot(211)
set(gcf,'PaperPosition',[1 1 3 3])
```

```
hold(gca,'all');
print('-dtiff','-r200','figure2.tif');

%% Reference
[ht,wd] = size(GrayProfile');
minx = 0/fps;
maxx=NFrames/fps;
y0 = (xtop+xbottom)/2;
maxy = -(y0-ht)/ppmm;
miny = -y0/ppmm;
rangex = maxx-minx;
rangey = maxy-miny;
dx = rangex/wd;
dy = rangey/ht;
x=minx:dx:maxx;
y=miny:dy:maxy;

%% Plot Kymogram
figure(3)
image(x,y,GrayProfile'); colormap gray(256);
set(gca,'YTick',-10:2:10,'YMinorTick','on','XTickLabel',' ');
set(3,'units','inches'); set(3,'position',[1 1 3 3])
ylabel('Displacement (mm)','fontsize',10);
% xlabel('Time (s)','fontsize',10);
Title('Low Pressure (1.0 kPa)')

%% Glottal Area Plot
figure(4)
set(gca,'FontSize',10,'FontName','Times');
plot(NonDimTime,DArea)
xlabel('Nondimensional time (t/T)')
ylabel('Glottal area (mm^2)')
set(gca,'YTick',0:2:24);
TITLE('M5 24 (P = 0.85 kPa)')

% Transpose Wanted Values
LeftEdge = LeftEdge';
RightEdge = RightEdge';
NonDimTime = NonDimTime';
DArea = DArea';
OUTPUT(:,1:4) = [NonDimTime, LeftEdge, RightEdge, DArea];
x = x'; y = y';
OUTPUT(:,5) = x(1:i); OUTPUT(1:ht+1,6) = y;
```

A.2 Vertical Displacement

```
% Program to measure the height of the vocal folds from videos taken at the
% anterior perspective

% Modified by Brian Pickup, 07 Aug 2009.

clear all
clf; close all
clc

fps= 9000;
Start = 5000;
Finish = 6000;
NFrames = Finish-Start;   %Number of frames kymographed. Change as necessary
extension = 'M5_35_1_00kPa_anterior_60fps';                %Change per movie
folder = ['F:\BrianP\HS Camera Videos for M5 MRI comparison\' extension];
filename = [folder '\' extension '.avi'];

%% Calibration

calibfile = ['F:\BrianP\System Back Up\Research\Thesis\M5_MRI\HS Camera\...
                Calibration\M5_35_Anterior.tif'];     %Change per model
calibimage = imshow(calibfile);
calibpixel = ginput(2);
title('Select two points exactly 17 mm apart')
ppmm = sqrt((calibpixel(1,1)-calibpixel(2,1))^2+(calibpixel(1,2)-...
                calibpixel(2,2))^2)/17;

for i=Start:Finish
    % Read images; change path & filename as necessary
        mov = aviread(filename,i);
        Picture = frame2im(mov);

    % Convert image to type double
        C=double(Picture);

    % Select display area corners
    if i==Start
        figure(1)
        NonDimTime=0:1/NFrames:(NFrames-1)/NFrames;
        subplot(111)
        image(C/3); axis xy; colormap(gray)
        title(['Select top left corner of display area'])
```

```
    pos1 = ginput(1); xleft = pos1(1); ytop = pos1(2);
    title(['Select bottom right of display area, flush ...
            with top of acrylic plates'])
    pos2 = ginput(1); xright = pos2(1); ybottom = pos2(2);
    xleft=round(xleft); xright = round(xright);
    ytop = round(ytop); ybottom = round(ybottom);
end

% Display original image with top as well as display area lines
figure(1)
subplot(121)
set(gca,'FontSize',10,'FontName','Times');
image(C/3); axis xy
shading interp
colormap gray
hold on
rectangle('Position',[xleft,ybottom,(xright-xleft),(ytop-ybottom)],...
            'LineStyle','--','EdgeColor','r');
hold off
title(['Image #' num2str(i) ''])

% Crop C by removing top & bottom
C(ytop:size(C,1),:)=[];
C(1:ybottom,:)=[];

% Identify all pixels with intensity > Thresh by coloring them green
Thresh=100;
D=im2bw(C/255,Thresh/255); % Convert grayscale image to binary image
E(:,:,1)=C/255; % Red channel
E(:,:,2)=1-D; % Green channel
E(:,:,3)=C/255; % Blue channel

% Plot orifice, midline, and lines to left & right vocal folds
subplot(122)
set(gca,'FontSize',10,'FontName','Times');
image(E); axis xy; % All pixels with intensity > Thresh are now green

%Find edge of vocal fold
Edge(i-Start+1) = find(min(E(:,:,2))==0,1,'first');
                            %Finds the first column where there is a zero
                            % i.e. left edge of vocal folds

% Command to update images
drawnow
```

```
end

%Convert heights to mm
heightgross = (max(Edge)-min(Edge))/ppmm;
heightmin = (xright-max(Edge))/ppmm;
heightmax = (xright-min(Edge))/ppmm;
OUTPUT(1:3,1) = [heightmax, heightmin, heightgross]

% Plot position of top of vocal fold
x = [0:(NFrames)];
y = (xright-Edge)/ppmm;
figure(2)
plot(x,y)
```

APPENDIX B. SCRIPT FILES

For computational modeling, three files for each geometrically defined model were developed: (1) the parameter file to define geometric properties of the vocal fold models, as well as time step size, inlet conditions, material properties, and domain geometries; (2) the solid domain file to mesh the different layers of the models; and (3) the fluid domain file to mesh the test domain, as well as define properties of the fluid (air) and dictate numerical method settings. These files allowed for communication with the supercomputers, which provided reasonable computational time for each run. The efforts of Dr. Scott Thomson and Jesse Daily in developing these script files are gratefully acknowledged.

B.1 Parameter File

```
*** SUBGLOTTAL DUCT LENGTH
PARAMETER DuctLength '.5588'

*** TIME STEPS
PARAMETER NSteps '12000'
PARAMETER dt '0.0000125'
PARAMETER MaxATS '20'

*** INLET PRESSURE BC
PARAMETER Pressure '-900'

*** ALPHA, BETA: RAYLEIGH DAMPING CONSTANTS
PARAMETER ALPHA '1.948193502'
PARAMETER BETA '0.000286578'

*** COVER MODULUS & POISSON'S RATIO
PARAMETER Ec '5000'
PARAMETER Nuc '0.49'

*** BODY MODULUS & POISSON'S RATIO
PARAMETER Eb '15000'
PARAMETER Nub '0.49'

*** EPITHELIUM MODULUS & POISSON'S RATIO
PARAMETER Ee '5000'
PARAMETER Nue '0.49'

*** ASL MODULUS & POISSON'S RATIO
PARAMETER Ea '300'
PARAMETER Na '0.49'

*** CALCULATIONS FOR STRESS_STRAIN CURVES
PARAMETER EcNeg '-$Ec/10'
PARAMETER EcNegS '-$Ec/2'
PARAMETER EcPos '$Ec/10'
PARAMETER EcPosS '$Ec/2'
PARAMETER EbNeg '-$Eb/10'
PARAMETER EbNegS '-$Eb/2'
PARAMETER EbPos '$Eb/10'
PARAMETER EbPosS '$Eb/2'
PARAMETER EaNeg '-$Ea/12'
PARAMETER EaNegS '-$Ea/1.5'
```

```
PARAMETER EaPos '$Ea/12'
PARAMETER EaPosS '$Ea/1.5'


*** BULK MODULI
*PARAMETER Kappac '$Ec/(3*(1-2*$Nuc))'
*PARAMETER Kappab '$Eb/(3*(1-2*$Nub))'
PARAMETER Kappac '1E5'
PARAMETER Kappab '1E5'

*** INLET DISPLACEMENT BC
PARAMETER TFTime '0.2'
PARAMETER TFdisp '0.01'

*** SOLID GRID DEFINITIONS
PARAMETER GridS '0.00005'
PARAMETER GridS2 '0.0002'

*** FLUID GRID DEFINITIONS
PARAMETER Grid1 '0.005'
PARAMETER Grid2 '8'
***Grid Modify
PARAMETER NDIV1v '40'
PARAMETER NDIV2v '20'
PARAMETER NDIV3v '80'
PARAMETER NDIV4v '3'
PARAMETER NDIV1h '8'
***Grid Modify
PARAMETER NDIV2h '80'
PARAMETER NDIV3h '40'
PARAMETER NDIV4h '4'
PARAMETER NDIV5h '20'
PARAMETER NDIVTube '120'

*** SYMMETRY PLANE
PARAMETER zt '0.0084'
PARAMETER dg '0.0001'
PARAMETER zc '$zt+$dg'
PARAMETER zContact '$zt+.000075'

*** Set Variables
PARAMETER D '.0084'

*** User Defined Variables
PARAMETER r1 '.00182'
```

```
PARAMETER r1B '.00145'
PARAMETER r2 '.000837'
PARAMETER r2B '.000360'
PARAMETER theta1 '50.65*3.14159/180'
PARAMETER theta1B '50.65*3.14159/180'
PARAMETER theta2 '2.75*3.14159/180'
PARAMETER theta2B '2.75*3.14159/180'
PARAMETER theta3 '88.85*3.14159/180'
PARAMETER theta3B '91.15*3.14159/180'
PARAMETER T '.00185'
PARAMETER delta '.00130'
PARAMETER Tt '.001075'


***Point definitions
*Cover Layer
PARAMETER L12 '($D-$r2*(1-cos($theta2))-$T*tan($theta2)...
                -$r1*(cos($theta2)-cos($theta1)))/sin($theta1)'
PARAMETER L1 '$L12*cos($theta1)+$r1*(sin($theta1)-sin($theta2))'
PARAMETER L2 '$T+$r2*(sin($theta2)+sin($theta3))'
PARAMETER L3 '1/tan($theta3)*($D-$r2*(1-cos($theta3)))'
PARAMETER L '$L1+$L2+$L3'
PARAMETER z7 '0'
PARAMETER y7 '$L'
PARAMETER z6 '$D-$r2*(1-cos($theta3))'
PARAMETER y6 '$y7-$z6/tan($theta3)'
PARAMETER z5 '$r2*(cos($theta3-($theta2+$theta3)/2)-cos($theta3))+$z6'
PARAMETER y5 '$r2*(sin(-($theta2-($theta2+$theta3)/2))-sin($theta3))+$y6'
PARAMETER z4 '$D-$r2*(1-cos($theta2))'
PARAMETER y4 '$y6-$r2*(sin($theta3)+sin($theta2))'
PARAMETER z3 '$z4-$T*tan($theta2)'
PARAMETER y3 '$y4-$T'
PARAMETER z2 '$L12*sin($theta1)'
PARAMETER y2 '$y3-$r1*(sin($theta1)-sin($theta2))'
PARAMETER z1 '0'
PARAMETER y1 '0'
PARAMETER z8 '$z2-$r1*cos($theta1)'
PARAMETER y8 '$y2+$r1*sin($theta1)'
PARAMETER z9 '$z6-$r2*cos($theta3)'
PARAMETER y9 '$y6-$r2*sin($theta3)'
*
*Body Layer
PARAMETER Lb '$L-$Tt-$Tt/sin($theta1)'
PARAMETER Tb1 '$Lb-$r1b*(sin($theta1b)-sin($theta2b))...
                -$r2b*(sin($theta2b)+sin($theta3b))'
```

```
PARAMETER Tb2 '-1/tan($theta3b)*($D-$delta-$r2b*(1-cos($theta3b)))'
PARAMETER Tb3 '-1/tan($theta1b)*($D-$delta-$r1b*(cos($theta2b)...
               -cos($theta1b))-$r2b*(1-cos($theta2b)))'
PARAMETER Tb4 '(1-tan($theta2b)/tan($theta1b))'
PARAMETER Tb '($Tb1+$Tb2+$Tb3)/$Tb4'
PARAMETER L12b '1/sin($theta1b)*($D-$delta-$r1b*(cos($theta2b)...
               -cos($theta1b))-$Tb*tan($theta2b)-$r2b*(1-cos($theta2b)))'
PARAMETER z14 '0'
PARAMETER y14 '$y7-$Tt'
PARAMETER z13 '$D-$delta-$r2b*(1-cos($theta3b))'
PARAMETER y13 '$y14-$z13/tan($theta3b)'
PARAMETER z12 '$D-$delta-$r2b*(1-cos($theta2b))'
PARAMETER y12 '$y13-$r2b*(sin($theta3b)+sin($theta2b))'
PARAMETER z11 '$z12-$Tb*tan($theta2b)'
PARAMETER y11 '$y12-$Tb'
PARAMETER z10 '$L12b*sin($theta1b)'
PARAMETER y10 '$y11-$r1b*(sin($theta1b)-sin($theta2b))'
PARAMETER z7a '0'
PARAMETER y7a '$Tt/sin($theta1)'
PARAMETER z15 '$z10-$r1b*cos($theta1b)'
PARAMETER y15 '$y10+$r1b*sin($theta1b)'
PARAMETER z16 '$z13-$r2b*cos($theta3b)'
PARAMETER y16 '$y13-$r2b*sin($theta3b)'
*
*Dr T Parameters
PARAMETER y17 '0.006'
PARAMETER z17 '$zContact'
PARAMETER y18 '0.012'
PARAMETER z18 '$zContact'
PARAMETER yf10 '-$DuctLength-0.308'
PARAMETER zf10 '$zc-10*0.01524'
PARAMETER yf11 '$yf10'
PARAMETER zf11 '-0.0731063'
PARAMETER yf12 '$yf10'
PARAMETER zf12 ' -0.0604063'
PARAMETER yf13 '$yf10'
PARAMETER zf13 '$zc-0.0127'
PARAMETER yf14 '$yf10'
PARAMETER zf14 '$zc'
PARAMETER yf15 '-$DuctLength'
PARAMETER zf15 '$zf10'
PARAMETER yf16 '$yf15'
PARAMETER zf16 '$zf11'
PARAMETER yf17 '$yf15'
PARAMETER zf17 '$zf12'
```

```
PARAMETER yf18 '$yf15'
PARAMETER zf18 '$zf13'
PARAMETER yf19 '$yf15'
PARAMETER zf19 '$zf14'
PARAMETER yf20 '-0.0032625'
PARAMETER zf20 '$zf13'
PARAMETER yf21 '$yf20'
PARAMETER zf21 '$zf14'
PARAMETER yf22 '0'
PARAMETER zf22 '$zf13'
PARAMETER yf23 '0'
PARAMETER zf23 '$zf14'
PARAMETER yf24 '$y3'
PARAMETER zf24 '$zf14'
PARAMETER yf25 '$y4'
PARAMETER zf25 '$zf14'
PARAMETER yf26 '$y6'
PARAMETER zf26 '$zf10'
PARAMETER yf27 '$y6+0.001'
PARAMETER zf27 '$zf10'
PARAMETER yf28 '$yf27'
PARAMETER zf28 '$z6'
PARAMETER yf29 '$yf27'
PARAMETER zf29 '$zf14'
PARAMETER yf30 '$y6+0.002'
PARAMETER zf30 '$zf10'
PARAMETER yf31 '$yf30'
PARAMETER zf31 '$z6'
PARAMETER yf32 '$yf30'
PARAMETER zf32 '$zf14'
PARAMETER yf33 '$y6+0.1'
PARAMETER zf33 '$zf10'
PARAMETER yf34 '$yf33'
PARAMETER zf34 '$z6'
PARAMETER yf35 '$yf33'
PARAMETER zf35 '$zf14'
PARAMETER yf36 '$yf27'
PARAMETER zf36 '$z7-0.001'
PARAMETER yf37 '$yf30'
PARAMETER zf37 '$zf36'
PARAMETER yf38 '$yf33'
PARAMETER zf38 '$zf36'
PARAMETER y39 '$y3+1/3*$T'
PARAMETER z39 '$z3+1/3*($z4-$z3)'
PARAMETER yf49 '$y39'
```

```
PARAMETER zf49 '$zf24'
PARAMETER y40 '$y3+2/3*$T'
PARAMETER z40 '$z3+2/3*($z4-$z3)'
PARAMETER yf50 '$y40'
PARAMETER zf50 '$zf24'

*** How many steps to save
PARAMETER NodeStepSkip '1'
PARAMETER ElementStepSkip '10'
```

B.2 Solid Domain File

```
*s.in
*
DATABASE NEW SAVE=NO PROMPT=NO
FEPROGRAM ADINA
CONTROL FILEVERSION=V84
*
MASTER ANALYSIS=DYNAMIC-DIRECT-INTEGRATION MODEX=EXECUTE,
     TSTART=0.00000000000000 IDOF=100011 OVALIZAT=NONE,
     FLUIDPOT=AUTOMATIC CYCLICPA=1 IPOSIT=STOP REACTION=YES,
     INITIALS=NO FSINTERA=YES IRINT=DEFAULT CMASS=NO,
     SHELLNDO=AUTOMATIC AUTOMATI=ATS SOLVER=SPARSE,
     CONTACT-=CONSTRAINT-FUNCTION TRELEASE=0.00000000000000,
     RESTART-=NO FRACTURE=NO LOAD-CAS=NO LOAD-PEN=NO MAXSOLME=0,
     MTOTM=2 RECL=3000 SINGULAR=YES STIFFNES=1.00000000000000E-09,
     MAP-OUTP=NONE MAP-FORM=NO NODAL-DE='' POROUS-C=NO ADAPTIVE=0,
     ZOOM-LAB=1 AXIS-CYC=0 PERIODIC=NO VECTOR-S=GEOMETRY EPSI-FIR=NO,
     STABILIZ=NO STABFACT=1.00000000000000E-12 RESULTS=PORTHOLE
*
READ parameter01.in
*
COORDINATES POINT SYSTEM=0
@CLEAR
1 0.0 $y1 $z1 0
2 0.0 $y2 $z2 0
3 0.0 $y3 $z3 0
4 0.0 $y4 $z4 0
5 0.0 $y6 $z6 0
6 0.0 $y7 $z7 0
7 0.0 $y8 $z8 0
8 0.0 $y9 $z9 0
9 0.0 $y7a $z7a 0
10 0.0 $y10 $z10 0
11 0.0 $y11 $z11 0
12 0.0 $y12 $z12 0
13 0.0 $y13 $z13 0
14 0.0 $y14 $z14 0
15 0.0 $y15 $z15 0
16 0.0 $y16 $z16 0
17 0.0 $y17 $z17 0
18 0.0 $y18 $z18 0
@
*
```

```
LINE STRAIGHT NAME=1 P1=1 P2=2
LINE ARC NAME=2 MODE=1 P1=2 P2=3 CENTER=7 PCOINCID=YES,
     PTOLERAN=1.0E-05
LINE STRAIGHT NAME=3 P1=3 P2=4
LINE ARC NAME=4 MODE=1 P1=4 P2=5 CENTER=8 PCOINCID=YES,
     PTOLERAN=1.0E-05
LINE STRAIGHT NAME=5 P1=5 P2=6
LINE STRAIGHT NAME=6 P1=9 P2=10
LINE ARC NAME=7 MODE=1 P1=10 P2=11 CENTER=15 PCOINCID=YES,
     PTOLERAN=1.0E-05
LINE STRAIGHT NAME=8 P1=11 P2=12
LINE ARC NAME=9 MODE=1 P1=12 P2=13 CENTER=16 PCOINCID=YES,
     PTOLERAN=1.0E-05
LINE STRAIGHT NAME=10 P1=13 P2=14
LINE STRAIGHT NAME=11 P1=1 P2=9
LINE STRAIGHT NAME=12 P1=6 P2=14
LINE STRAIGHT NAME=13 P1=14 P2=9
LINE STRAIGHT NAME=14 P1=17 P2=18
LINE COMBINED NAME=15 COUPLED=YES RESTRICT=NO
@CLEAR
1 2 3 4 5 12 10 9 8 7 6 11
@
LINE COMBINED NAME=16 COUPLED=YES RESTRICT=NO
@CLEAR
6 7 8 9 10 13
@
*
BODY SHEET NAME=1 LINE=15 DELETE-L=YES
BODY SHEET NAME=2 LINE=16 DELETE-L=YES
*
SUBDIVIDE FACE NAME=1 BODY=1 MODE=LENGTH SIZE=$GridS
SUBDIVIDE EDGE NAME=12 BODY=1 MODE=LENGTH SIZE=$GridS2
@CLEAR
11 10 9 8 7 6
@
SUBDIVIDE EDGE NAME=1 BODY=2 MODE=LENGTH SIZE=$GridS2
@CLEAR
2 3 4 5 6
@
*
SUBDIVIDE EDGE NAME=3 BODY=1 MODE=DIVISIONS NDIV=75,
     RATIO=1 PROGRESS=ARITHMETIC
SUBDIVIDE EDGE NAME=4 BODY=1 MODE=DIVISIONS NDIV=80,
     RATIO=1 PROGRESS=ARITHMETIC
*
```

```
FIXBOUNDARY EDGES FIXITY=ALL BODY=1
@CLEAR
6  'ALL'
12  'ALL'
@
FIXBOUNDARY EDGES FIXITY=ALL BODY=2
@CLEAR
6  'ALL'
@
*
FSBOUNDARY TWO-D NAME=1
@CLEAR
1 1
2 1
3 1
4 1
5 1
@
*
KINEMATICS DISPLACE=LARGE STRAINS=LARGE PRESSURE=NO INCOMPAT=NO
*
* Cover stress-strain curve
SSCURVE NAME=1 CONSTANT=YES NU=0.495
@CLEAR
-0.5 $EcNegS 0
-0.1 $EcNeg 0
0 0 0
0.1 $EcPos 0
0.5 $EcPosS 0
1.0 $Ec 0
@
*
* Body stress-strain curve
SSCURVE NAME=2 CONSTANT=YES NU=0.495
@CLEAR
-0.5 $EbNegS 0
-0.1 $EbNeg 0
0 0 0
0.1 $EbPos 0
0.5 $EbPosS 0
1.0 $Eb 0
@
*
CURVE-FITTIN NAME=1 TENSION-=1 SHEAR-CU=0 EQUIBIAX=0 ORDER=6,
        WEIGHTIN=NO CURVE-TY=STRAIN METHOD=SVD NSINGULA=AUTOMATIC,
```

```
        ECHO=ALL
*
MATERIAL OGDEN NAME=1 MU1=0 ALPHA1=0, MU2=0 ALPHA2=0, MU3=0 ALPHA3=0,
        MU4=0 ALPHA4=0, MU5=0 ALPHA5=0, MU6=0 ALPHA6=0, MU7=0 ALPHA7=0,
        MU8=0 ALPHA8=0, MU9=0 ALPHA9=0, KAPPA=$Kappac DENSITY=1070 FITTING-=1,
        VISCOELA=0 TEMPERAT=NO TREF=0.00000000000000 RUBBER-T=0,
        RUBBER-V=0 RUBBER-M=0 RUBBER-O=0 MDESCRIP='Cover'
*
CURVE-FITTIN NAME=2 TENSION-=2 SHEAR-CU=0 EQUIBIAX=0 ORDER=6,
        WEIGHTIN=NO CURVE-TY=STRAIN METHOD=SVD NSINGULA=AUTOMATIC,
        ECHO=ALL
*
MATERIAL OGDEN NAME=2 MU1=0 ALPHA1=0, MU2=0 ALPHA2=0, MU3=0 ALPHA3=0,
        MU4=0 ALPHA4=0, MU5=0 ALPHA5=0, MU6=0 ALPHA6=0, MU7=0 ALPHA7=0,
        MU8=0 ALPHA8=0, MU9=0 ALPHA9=0, KAPPA=$Kappab DENSITY=1070 FITTING-=2,
        VISCOELA=0 TEMPERAT=NO TREF=0.00000000000000 RUBBER-T=0,
        RUBBER-V=0 RUBBER-M=0 RUBBER-O=0 MDESCRIP='Body'

EGROUP TWODSOLID NAME=1 SUBTYPE=STRAIN DISPLACE=DEFAULT,
     STRAINS=DEFAULT MATERIAL=1 INT=DEFAULT RESULTS=STRESSES DEGEN=NO,
     FORMULAT=0 STRESSRE=GLOBAL INITIALS=NONE FRACTUR=NO,
     CMASS=DEFAULT STRAIN-F=0 UL-FORMU=DEFAULT PNTGPS=0 NODGPS=0,
     LVUS1=0 LVUS2=0 SED=NO RUPTURE=ADINA INCOMPAT=DEFAULT,
     TIME-OFF=0.00000000000000 POROUS=NO WTMC=1.00000000000000,
     OPTION=NONE DESCRIPT='Cover'
*
EGROUP TWODSOLID NAME=2 SUBTYPE=STRAIN DISPLACE=DEFAULT,
     STRAINS=DEFAULT MATERIAL=2 INT=DEFAULT RESULTS=STRESSES DEGEN=NO,
     FORMULAT=0 STRESSRE=GLOBAL INITIALS=NONE FRACTUR=NO,
     CMASS=DEFAULT STRAIN-F=0 UL-FORMU=DEFAULT PNTGPS=0 NODGPS=0,
     LVUS1=0 LVUS2=0 SED=NO RUPTURE=ADINA INCOMPAT=DEFAULT,
     TIME-OFF=0.00000000000000 POROUS=NO WTMC=1.00000000000000,
     OPTION=NONE DESCRIPT='Body'
*
GFACE NODES=3 NCOINCID=BOUNDARIES NCTOLERA=1.00000000000000E-05,
     SUBSTRUC=0 GROUP=1 PREFSHAP=TRIANGULAR BODY=1 COLLAPSE=NO,
     SIZE-FUN=0 MIDNODES=CURVED METHOD=ADVFRONT NLAYER=1 NLTABL=0
@CLEAR
1
@
*
GFACE NODES=3 NCOINCID=BOUNDARIES NCTOLERA=1.00000000000000E-05,
     SUBSTRUC=0 GROUP=2 PREFSHAP=TRIANGULAR BODY=2 COLLAPSE=NO,
     SIZE-FUN=0 MIDNODES=CURVED METHOD=ADVFRONT NLAYER=1 NLTABL=0
@CLEAR
```

```
1

GEDGE NODES=2 NCOINCID=ALL NCTOLERA=1E-05 SUBSTRUC=0,
     GROUP=4 BODY=1 MIDNODES=CURVED
@CLEAR
1 2 3 4 5
@

*
PPROCESS NPROC=1 MINEL=0 MAXEL=999999
*
EGCONTROL MAXELG=999999
*
ELEMSAVE-STE NODESAVE=NO
@CLEAR
1 1 $NSteps $ElementStepSkip
@
NODESAVE-STE ELEMSAVE=NO
@CLEAR
1 1 $NSteps $NodeStepSkip
@
*
RAYLEIGH-DAM
@CLEAR
1 $ALPHA $BETA
2 $ALPHA $BETA
3 $ALPHA $BETA
@
CGROUP CONTACT2 NAME=1 SUBTYPE=STRAIN FORCES=YES TRACTION=YES,
     NODETONO=NO FRICTION=0.00000000000000 EPSN=1.00000000000000E-12,
     EPST=0.00000000000000 DIRECTIO=NORMAL CONTINUO=YES,
     INITIAL-=ALLOWED PENETRAT=ONE DEPTH=0.00000000000000,
     OFFSET=0.00000000000000 OFFSET-T=CONSTANT CORNER-C=NO,
     TBIRTH=0.00000000000000 TDEATH=0.00000000000000 TIED=NO,
     TIED-OFF=0.00000000000000 HHATTMC=0.00000000000000,
     FCTMC=0.500000000000000 FTTMC=0.500000000000000 RIGID-TA=NO,
     NORMAL-S=1.00000000000000E+11 TANGENTI=0.00000000000000,
     PTOLERAN=1.00000000000000E-08 RESIDUAL=0.00100000000000000,
     LIMIT-FO=1.00000000000000 ITERATIO=2 TIME-PEN=0.00000000000000,
     CONSISTE=DEFAULT USER-FRI=NO DESCRIPT='NONE',
     CFACTOR1=0.00000000000000 CS-EXTEN=0.00100000000000000,
     ALGORITH=DEFAULT RTP-CHEC=NO RTP-MAX=0.00100000000000000,
     XDAMP=NO XNDAMP=0.100000000000000 DISPLACE=DEFAULT FRIC-DEL=NO,
     GAP-VALU=0.00000000000000 EKTMC=0.00000000000000
*
```

```
CONTACTSURFA NAME=1 PRINT=DEFAULT SAVE=DEFAULT SOLID=YES BODY=1,
     ORIENTAT=AUTOMATIC MARQUEEB=0 DESCRIPT='NONE'
@CLEAR
2 1 0
3 1 0
4 1 0
@
*
CONTACTSURFA NAME=2 PRINT=DEFAULT SAVE=DEFAULT SOLID=NO BODY=1,
     ORIENTAT=AUTOMATIC MARQUEEB=0 DESCRIPT='NONE'
@CLEAR
14 1 0
@
*
CONTACTPAIR NAME=1 TARGET=2 CONTACTO=1 FRICTION=0.00000000000000,
     TBIRTH=0.00000000000000 TDEATH=0.00000000000000,
     HHATTMC=0.00000000000000 FCTMC=0.00000000000000,
     FTTMC=0.00000000000000 NX=0 NY=0 NZ=0 OFFSETCO=BOTH,
     EKTMC=0.00000000000000
*
SUBDIVIDE LINE NAME=14 MODE=DIVISIONS NDIV=100 RATIO=1,
     PROGRESS=GEOMETRIC CBIAS=NO
*
CSURFACE NAME=2 NODES=2 NCOINCID=SURFACE,
     NCTOLERA=1.00000000000000E-05 SUBSTRUC=0 GROUP=1
****
ADINA OPTIMIZE=SOLVER FILE='s.dat',
   FIXBOUND=YES MIDNODE=NO OVERWRIT=YES
DATABASE SAVE PERMFILE='s.idb' PROMPT=NO
*END SAVE=NO IMMEDIATE = NO
*
*
*THE FOLLOWING LINES ARE FOR MODAL ANALYSIS
*
*CSDELETE LINE GROUP=1 CONTACTS=2 NODE-DEL=YES BODY=0
*@CLEAR
*14
*@
*COORDINATES POINT SYSTEM=0
*17 0.0 $y17 0.009 0
*18 0.0 $y18 0.009 0
*@
*CSURFACE NAME=2 NODES=2 NCOINCID=SURFACE,
*     NCTOLERA=1.00000000000000E-05 SUBSTRUC=0 GROUP=1
*MASTER ANALYSIS=FREQUENCIES MODEX=EXECUTE TSTART=0.00000000000000,
```

```
*     IDOF=100011 OVALIZAT=NONE FLUIDPOT=AUTOMATIC CYCLICPA=1,
*     IPOSIT=STOP REACTION=YES INITIALS=NO FSINTERA=NO IRINT=DEFAULT,
*     CMASS=NO SHELLNDO=AUTOMATIC AUTOMATI=ATS SOLVER=SPARSE,
*     CONTACT-=CONSTRAINT-FUNCTION TRELEASE=0.00000000000000,
*     RESTART-=NO FRACTURE=NO LOAD-CAS=NO LOAD-PEN=NO MAXSOLME=0,
*     MTOTM=2 RECL=3000 SINGULAR=YES STIFFNES=1.00000000000000E-09,
*     MAP-OUTP=NONE MAP-FORM=NO NODAL-DE='' POROUS-C=NO ADAPTIVE=0,
*     ZOOM-LAB=1 AXIS-CYC=0 PERIODIC=NO VECTOR-S=GEOMETRY EPSI-FIR=NO,
*     STABILIZ=NO STABFACT=1.00000000000000E-12 RESULTS=PORTHOLE,
*     FEFCORR=NO BOLTSTEP=1
**
*FREQUENCIES METHOD=SUBSPACE-ITERATION NEIGEN=6 NMODE=3 IPRINT=NO,
*     RIGID-BO=NO RSHIFT=0.00000000000000 CUTOFF=1.00000000000000E+08,
*     NITEMM=DEFAULT NVECTOR=DEFAULT STURM-CH=NO ACCELERA=NO,
*     TOLERANC=DEFAULT STARTTYP=LANCZOS NSTVECTO=0 INTERVAL=NO,
*     FMIN=0.00000000000000 FMAX=DEFAULT MODALSTR=NO STATIC=NO,
*     NSHIFT=AUTO NSHIFT-B=50
*ADINA OPTIMIZE=SOLVER FILE='sMod.dat',
*     FIXBOUND=YES MIDNODE=NO OVERWRIT=YES
*DATABASE SAVE PERMFILE='sMod.idb' PROMPT=NO
```

B.3 Fluid Domain File

```
*** f.in
*
DATABASE NEW SAVE=NO PROMPT=NO
FEPROGRAM ADINA-F
CONTROL FILEVERSION=V84
*
MASTER ANALYSIS=TRANSIENT MODEX=EXECUTE TSTART=0.00000000000000,
     IDOF=10001 TURBULEN=NO HYDRO=YES STREAM=YES TRACTB=YES,
     IRINT=DEFAULT AUTOMATI=YES SOLVER=SPARSE COMPRESS=SLI,
     FSINTERA=YES NMASS=0 MASSCOUP=NO MAP-OUTP=NONE MAP-FORM=NO,
     NONDIMEN=NO MAXSOLME=0 MTOTM=2 RECL=3000 ALE=NO THERMAL-=NO,
     UPWINDIN=FINITE-ELEMENT MESHUPDA=ORIGINAL MESHADAP=NO,
     COUPLING=DIRECT POROUS-C=NO CELL-BCD=YES VOF=NO FCBI=NO,
     TURB-ITE=COUPLED EM-MODEL=NO ALE-CURV=YES ADAPTIVE='' ENSIGHT-=FORMATTED
*
READ parameter01.in
*
COORDINATES POINT SYSTEM=0
@CLEAR
1 0.0 $y1 $z1 0
2 0.0 $y2 $z2 0
3 0.0 $y3 $z3 0
4 0.0 $y4 $z4 0
5 0.0 $y5 $z5 0
6 0.0 $y6 $z6 0
7 0.0 $y7 $z7 0
8 0.0 $y8 $z8 0
9 0.0 $y9 $z9 0
10 0.0 $yf10 $zf10 0
11 0.0 $yf11 $zf11 0
12 0.0 $yf12 $zf12 0
13 0.0 $yf13 $zf13 0
14 0.0 $yf14 $zf14 0
15 0.0 $yf15 $zf15 0
16 0.0 $yf16 $zf16 0
17 0.0 $yf17 $zf17 0
18 0.0 $yf18 $zf18 0
19 0.0 $yf19 $zf19 0
20 0.0 $yf20 $zf20 0
21 0.0 $yf21 $zf21 0
22 0.0 $yf22 $zf22 0
23 0.0 $yf23 $zf23 0
```

```
24 0.0 $yf24 $zf24 0
25 0.0 $yf25 $zf25 0
26 0.0 $yf26 $zf26 0
27 0.0 $yf27 $zf27 0
28 0.0 $yf28 $zf28 0
29 0.0 $yf29 $zf29 0
30 0.0 $yf30 $zf30 0
31 0.0 $yf31 $zf31 0
32 0.0 $yf32 $zf32 0
33 0.0 $yf33 $zf33 0
34 0.0 $yf34 $zf34 0
35 0.0 $yf35 $zf35 0
36 0.0 $yf36 $zf36 0
37 0.0 $yf37 $zf37 0
38 0.0 $yf38 $zf38 0
39 0.0 $y39 $z39 0
40 0.0 $y40 $z40 0
49 0.0 $yf49 $zf49 0
50 0.0 $yf50 $zf50 0
@
*
LINE STRAIGHT NAME=1 P1=1 P2=2
LINE ARC NAME=2 MODE=1 P1=2 P2=3 CENTER=8 PCOINCID=YES,
     PTOLERAN=1.0E-05
LINE ARC NAME=4 MODE=1 P1=4 P2=5 CENTER=9 PCOINCID=YES,
     PTOLERAN=1.0E-05
LINE ARC NAME=5 MODE=1 P1=5 P2=6 CENTER=9 PCOINCID=YES,
     PTOLERAN=1.0E-05
LINE STRAIGHT NAME=6 P1=6 P2=7
LINE STRAIGHT NAME=7 P1=10 P2=11
LINE STRAIGHT NAME=8 P1=11 P2=12
LINE STRAIGHT NAME=9 P1=12 P2=13
LINE STRAIGHT NAME=10 P1=13 P2=14
LINE STRAIGHT NAME=11 P1=10 P2=15
LINE STRAIGHT NAME=12 P1=11 P2=16
LINE STRAIGHT NAME=13 P1=12 P2=17
LINE STRAIGHT NAME=14 P1=13 P2=18
LINE STRAIGHT NAME=15 P1=14 P2=19
LINE STRAIGHT NAME=16 P1=15 P2=16
LINE STRAIGHT NAME=17 P1=16 P2=17
LINE STRAIGHT NAME=18 P1=17 P2=18
LINE STRAIGHT NAME=19 P1=18 P2=19
LINE STRAIGHT NAME=20 P1=18 P2=20
LINE STRAIGHT NAME=21 P1=19 P2=21
LINE STRAIGHT NAME=22 P1=20 P2=21
```

```
LINE STRAIGHT NAME=23 P1=20 P2=22
LINE STRAIGHT NAME=24 P1=20 P2=1
LINE STRAIGHT NAME=25 P1=21 P2=23
LINE STRAIGHT NAME=26 P1=22 P2=1
LINE STRAIGHT NAME=27 P1=1 P2=23
LINE STRAIGHT NAME=28 P1=23 P2=24
LINE STRAIGHT NAME=29 P1=3 P2=24
LINE STRAIGHT NAME=31 P1=4 P2=25
LINE STRAIGHT NAME=32 P1=25 P2=29
LINE STRAIGHT NAME=33 P1=5 P2=29
LINE STRAIGHT NAME=34 P1=6 P2=28
LINE STRAIGHT NAME=35 P1=7 P2=36
LINE STRAIGHT NAME=36 P1=26 P2=7
LINE STRAIGHT NAME=37 P1=26 P2=27
LINE STRAIGHT NAME=38 P1=27 P2=36
LINE STRAIGHT NAME=39 P1=28 P2=29
LINE STRAIGHT NAME=40 P1=27 P2=30
LINE STRAIGHT NAME=41 P1=28 P2=31
LINE STRAIGHT NAME=42 P1=29 P2=32
LINE STRAIGHT NAME=43 P1=30 P2=37
LINE STRAIGHT NAME=44 P1=31 P2=32
LINE STRAIGHT NAME=45 P1=30 P2=33
LINE STRAIGHT NAME=46 P1=31 P2=34
LINE STRAIGHT NAME=47 P1=32 P2=35
LINE STRAIGHT NAME=48 P1=33 P2=38
LINE STRAIGHT NAME=49 P1=34 P2=35
LINE COMBINED NAME=50 COUPLED=YES RESTRICT=YES
@CLEAR
1 2
@
LINE STRAIGHT NAME=51 P1=36 P2=37
LINE STRAIGHT NAME=52 P1=37 P2=38
LINE STRAIGHT NAME=53 P1=36 P2=28
LINE STRAIGHT NAME=54 P1=37 P2=31
LINE STRAIGHT NAME=55 P1=38 P2=34
LINE STRAIGHT NAME=56 P1=3 P2=39
LINE STRAIGHT NAME=57 P1=39 P2=40
LINE STRAIGHT NAME=58 P1=40 P2=4
LINE STRAIGHT NAME=59 P1=24 P2=49
LINE STRAIGHT NAME=60 P1=49 P2=50
LINE STRAIGHT NAME=61 P1=50 P2=25
LINE STRAIGHT NAME=62 P1=39 P2=49
LINE STRAIGHT NAME=63 P1=40 P2=50
*
SURFACE PATCH NAME=1 EDGE1=7 EDGE2=12 EDGE3=16 EDGE4=11
```

```
SURFACE PATCH NAME=2 EDGE1=8 EDGE2=13 EDGE3=17 EDGE4=12
SURFACE PATCH NAME=3 EDGE1=9 EDGE2=14 EDGE3=18 EDGE4=13
SURFACE PATCH NAME=4 EDGE1=10 EDGE2=15 EDGE3=19 EDGE4=14
SURFACE PATCH NAME=5 EDGE1=19 EDGE2=21 EDGE3=22 EDGE4=20
SURFACE PATCH NAME=6 EDGE1=23 EDGE2=24 EDGE3=26 EDGE4=0
SURFACE PATCH NAME=7 EDGE1=22 EDGE2=25 EDGE3=27 EDGE4=24
SURFACE PATCH NAME=8 EDGE1=27 EDGE2=28 EDGE3=29 EDGE4=50
SURFACE PATCH NAME=9 EDGE1=29 EDGE2=59 EDGE3=62 EDGE4=56
SURFACE PATCH NAME=10 EDGE1=31 EDGE2=32 EDGE3=33 EDGE4=4
SURFACE PATCH NAME=11 EDGE1=33 EDGE2=39 EDGE3=34 EDGE4=5
SURFACE PATCH NAME=12 EDGE1=6 EDGE2=34 EDGE3=53 EDGE4=35
SURFACE PATCH NAME=13 EDGE1=35 EDGE2=38 EDGE3=37 EDGE4=36
SURFACE PATCH NAME=14 EDGE1=39 EDGE2=42 EDGE3=44 EDGE4=41
SURFACE PATCH NAME=15 EDGE1=41 EDGE2=43 EDGE3=40 EDGE4=38
SURFACE PATCH NAME=16 EDGE1=44 EDGE2=47 EDGE3=49 EDGE4=46
SURFACE PATCH NAME=17 EDGE1=43 EDGE2=46 EDGE3=48 EDGE4=45
SURFACE PATCH NAME=18 EDGE1=53 EDGE2=41 EDGE3=54 EDGE4=51
SURFACE PATCH NAME=19 EDGE1=38 EDGE2=51 EDGE3=43 EDGE4=40
SURFACE PATCH NAME=20 EDGE1=54 EDGE2=46 EDGE3=55 EDGE4=52
SURFACE PATCH NAME=21 EDGE1=43 EDGE2=52 EDGE3=48 EDGE4=45
SURFACE PATCH NAME=22 EDGE1=62 EDGE2=60 EDGE3=63 EDGE4=57
SURFACE PATCH NAME=23 EDGE1=63 EDGE2=61 EDGE3=31 EDGE4=58
*
BOUNDARY-CON WALL NAME=1 GTYPE=LINES SLIPC=0 MOVING=NO,
     VTYPE=CONVENTIONAL VT=0 NCURVT=0 DX=1 DY=0 DZ=0 X0=0,
     Y0=0 Z0=0 ALL-EXT=NO THERMAL=HEAT-FLUX TVALUE=0 NCURT=0
@CLEAR
*7 0
*9 0
*10 0
11 0
16 0
17 0
18 0
20 0
23 0
26 0
36 0
@
*
BOUNDARY-CON WALL NAME=2 GTYPE=LINES SLIPC=1 MOVING=NO,
     VTYPE=CONVENTIONAL VT=0 NCURVT=0 DX=1 DY=0 DZ=0 X0=0,
     Y0=0 Z0=0 ALL-EXT=NO THERMAL=HEAT-FLUX TVALUE=0 NCURT=0
@CLEAR
15 0
```

```
21 0
25 0
28 0
59 0
60 0
61 0
32 0
42 0
47 0
@
*
BOUNDARY-CON FLUID-STRUCTURE NAME=3 GTYPE=LINES SLIPC=0,
     FSBOUNDA=1 VTYPE=CONVENTIONAL VT=0 NCURVT=0 DX=0 DY=0,
     DZ=0 X0=1 Y0=0 Z0=0 ALL-EXT=NO THERMAL=HEAT-FLUX TVALUE=0 NCURT=0
@CLEAR
50 0
56 0
57 0
58 0
4 0
5 0
6 0
@
* For this area ratio, 0.001 m / 0.005 s is good
TIMEFUNCTION NAME=2
@CLEAR
0 0
$TFTime $TFDisp
1.E+20 $TFDisp
@
zBOUNDARY-CON WALL NAME=4 GTYPE=LINES SLIPC=0,
     MOVING=YES NCURX=0 NCURY=2 NCURZ=0 START=0,
     STOP=1.0E+12 VTYPE=CONVENTIONAL VT=0.0,
     NCURVT=0 DX=1.0 DY=0.0 DZ=0.0 X0=0.0 Y0=0.0,
     Z0=0.0 ALL-EXT=NO THERMAL=HEAT-FLUX TVALUE=0.0 NCURT=0
@CLEAR
8 0
@
*
LEADER-FOLLO
@CLEAR
1 3 24 1 0
2 4 25 1 0
3 5 29 1 0
4 5 32 1 0
```

```
5 6 28 1 0
6 6 31 1 0
7 39 49 1 0
8 40 50 1 0
@
*
LOAD NORMAL-TRACTION NAME=1 MAGNITUD=$Pressure
*
APPLY-LOAD BODY=0
@CLEAR
1  'NORMAL-TRACTION' 1  'LINE' 8 0 1 0 0 0 0 0
2  'NORMAL-TRACTION' 1  'LINE' 9 0 1 0 0 0 0 0
3  'NORMAL-TRACTION' 1  'LINE' 10 0 1 0 0 0 0 0
4  'NORMAL-TRACTION' 1  'LINE' 7 0 1 0 0 0 0 0
@
*
FIXITY NAME=ZEROPRES
@CLEAR
 'X-VELOCITY'
 'PRESSURE'
 'TEMPERATURE'
 'TURBULENT-K'
 'TURBULENT-E'
@
FIXBOUNDARY LINES FIXITY=ALL
@CLEAR
37  'ZEROPRES'
40  'ZEROPRES'
45  'ZEROPRES'
48  'ZEROPRES'
49  'ZEROPRES'
55  'ZEROPRES'
@
MATERIAL CONSTF NAME=1 XMU=1.8E-05 CP=0,
     XKCON=0.0 BETA=0.0 QB=0.0 RHO=1.2 TREF=0.0,
     GRAV-X=0.0 GRAV-Y=0.0 GRAV-Z=0.0 SIGMA=0.0,
     KAPPA=141000 CV=0.0 MDESCRIP='Air'
*
SUBDIVIDE SURFACE NAME=1 MODE=LENGTH SIZE=$Grid1
@CLEAR
2 3 4 5
@
SUBDIVIDE SURFACE NAME=6 MODE=DIVISIONS NDIV1=$NDIV1h NDIV2=$NDIV1h,
     RATIO1=1 RATIO2=1 PROGRESS=GEOMETRIC EXTEND=NONE CBIAS1=NO CBIAS2=NO
SUBDIVIDE SURFACE NAME=7 MODE=DIVISIONS NDIV1=$NDIV1v NDIV2=$NDIV1h,
```

```
     RATIO1=1 RATIO2=1 PROGRESS=GEOMETRIC EXTEND=NONE CBIAS1=NO CBIAS2=NO
SUBDIVIDE LINE NAME=20 MODE=DIVISIONS NDIV=$NDIVTube RATIO=0.05,
     PROGRESS=ARITHMETIC CBIAS=NO
@CLEAR
21
@
SUBDIVIDE LINE NAME=29 MODE=DIVISIONS NDIV=$NDIV1v RATIO=1,
     PROGRESS=ARITHMETIC CBIAS=NO
@CLEAR
31 33 34 63 62
@
SUBDIVIDE LINE NAME=50 MODE=DIVISIONS NDIV=$NDIV1v RATIO=1,
     PROGRESS=ARITHMETIC CBIAS=NO
@CLEAR
4 5 39 41 42 44
@
SUBDIVIDE LINE NAME=56 MODE=DIVISIONS NDIV=25 RATIO=1,
     PROGRESS=ARITHMETIC CBIAS=NO
@CLEAR
57 58 59 60 61
@
SUBDIVIDE LINE NAME=32 MODE=DIVISIONS NDIV=$NDIV1v RATIO=4,
     PROGRESS=ARITHMETIC CBIAS=NO
SUBDIVIDE LINE NAME=28 MODE=DIVISIONS NDIV=$NDIV2h RATIO=0.4,
     PROGRESS=ARITHMETIC CBIAS=NO
SUBDIVIDE LINE NAME=50 MODE=DIVISIONS NDIV=$NDIV2h RATIO=0.25,
     PROGRESS=ARITHMETIC CBIAS=NO
SUBDIVIDE LINE NAME=6 MODE=DIVISIONS NDIV=$NDIV1v RATIO=10,
     PROGRESS=ARITHMETIC CBIAS=NO
SUBDIVIDE LINE NAME=53 MODE=DIVISIONS NDIV=$NDIV1v RATIO=0.1,
     PROGRESS=ARITHMETIC CBIAS=NO
@CLEAR
54
@
SUBDIVIDE LINE NAME=35 MODE=DIVISIONS NDIV=$NDIV4h RATIO=1,
     PROGRESS=ARITHMETIC CBIAS=NO
@CLEAR
51
@
SUBDIVIDE LINE NAME=36 MODE=DIVISIONS NDIV=$NDIV2v RATIO=0.05,
     PROGRESS=ARITHMETIC CBIAS=NO
@CLEAR
38 43 48
@
SUBDIVIDE LINE NAME=46 MODE=DIVISIONS NDIV=$NDIV3v RATIO=50,
```

```
     PROGRESS=ARITHMETIC CBIAS=NO
@CLEAR
47 52
SUBDIVIDE LINE NAME=45 MODE=DIVISIONS NDIV=$NDIV5h RATIO=1,
     PROGRESS=ARITHMETIC CBIAS=NO
SUBDIVIDE LINE NAME=55 MODE=DIVISIONS NDIV=$NDIV4v RATIO=1,
     PROGRESS=ARITHMETIC CBIAS=NO
*
EGROUP TWODFLUID NAME=1 SUBTYPE=PLANAR MATERIAL=1 INT=3,
     RESULTS=STRESSES DEGEN=NO DISSP=NO SOLID=NO UPWINDIN=DEFAULT,
     OPTION=NONE FLOWTYPE=DEFAULT VOF-MATE=1 DESCRIPT='NONE'
*
GSURFACE NODES=4 PATTERN=AUTOMATIC NCOINCID=BOUNDARIES NCEDGE=1234,
     NCVERTEX=1234 NCTOLERA=1.00000000000000E-05 SUBSTRUC=0 GROUP=1,
     PREFSHAP=AUTOMATIC MESHING=MAPPED SMOOTHIN=NO DEGENERA=NO,
     COLLAPSE=NO MIDNODES=CURVED METHOD=ADVFRONT FLIP=NO
@CLEAR
1 2 3 4 5 6 7 8 9 10 11 12 13 14 16 18 19 20 21 22 23
@
ANALYSIS TRANSIENT ALPHA=0.707106781186547 METHOD=COMPOSI
*
TIMESTEP NAME=DEFAULT
@CLEAR
$NSteps $dt
@
*
AUTOMATIC TIME-STEPPING MAXSUBD=$MaxATS ICOUR=ATS,
     COURAN=1.0E+20 ITMAXC=100000
*
ITERATION METHOD=NEWTON MAX-ITER=300 ITM-SPEC=1
*
ANALYSIS TRANSIENT ALPHA=1.00000000000000 METHOD=EULER
*
TOLERANCES FLUID-STRUCTURE CONVERGE=FD ITLIM=300,
     DTOTD=0.01 DTOTF=0.01 RLXFORCE=1 RLXDISPL=1,
     COUPLING=DIRECT
*
ELEMSAVE-STE NODESAVE=NO
@CLEAR
1 1 $NSteps $ElementStepSkip
@
NODESAVE-STE ELEMSAVE=NO
@CLEAR
1 1 $NSteps $NodeStepSkip
@
```

```
*** WRITE OUTPUT FILES
ADINA-F OPTIMIZE=SOLVER FILE='f.dat' FIXBOUND=YES,
     MIDNODE=NO OVERWRIT=YES FORMATTE=YES
*
DATABASE SAVE PERMFILE='f.idb' PROMPT=NO
*END SAVE=NO IMMEDIATE = NO
```

APPENDIX C. ENSIGHT COMMAND FILE

Ensight was used to measure glottal width and flow rate, as well as create animations of all computational models. The assistance of Simeon Smith in developing these command files is gratefully acknowledged.

```
VERSION 9.03
#
part: select_default
part: modify_begin
part: elt_representation 3D_feature_2D_full
part: modify_end
data: binary_files_are big_endian
data: format case
data: shift_time 1.000000 0.000000 0.000000
data: replace f.case
#
# Zoom To Correct Location
view_transf: axis y
view_transf: rotate 0.000000e+00 -9.000000e+01 0.000000e+00
view_transf: axis z
view_transf: rotate 0.000000e+00 0.000000e+00 -9.000000e+01
view_transf: action band_zoom
view_transf: look_at 3.891592e-01 -3.125907e-01 -6.769991e-02
view_transf: look_from 3.891592e-01 -3.125907e-01 2.607852e-03
view_transf: center_of_transform 0.000000e+00 0.000000e+00 0.000000e+00
view_transf: zclip_front 1.000000e-03
view_transf: action translate
view_transf: translate 3.201771e-03 1.242475e-03 0.000000e+00
view_transf: zoom 8.389896e-01
view_transf: zoom 8.376800e-01
view_transf: translate -2.812764e-05 -4.442018e-03 0.000000e+00
view_transf: zoom 8.292564e-01
view_transf: translate 6.997522e-04 9.130202e-04 0.000000e+00
view_transf: zoom 9.112983e-01
view_transf: translate 0.000000e+00 -1.147635e-04 0.000000e+00
#
# Calculate Variables
part: select_begin
 20
part: select_end
variables: evaluate zcoord = Coordinates[Z]
variables: evaluate zmax = Max(plist,zcoord)
variables: evaluate gap = 2*(8.5e-03-zmax)
viewport: select_begin
 1
viewport: select_end
part: select_begin
 1
part: select_end
tools: line ON
```

```
view_transf: function line
view_transf: line 1 0.000000e+00 1.700000e-02 0.000000e-03
view_transf: line 2 0.000000e+00 1.700000e-02 8.500000e-03
clip: begin
clip: domain intersect
clip: plane_extents infinite
clip: tool line
clip: line 1 0.0 0.017 0
clip: line 2 0.0 0.017 0.00850000046194
clip: end
clip: create
variables: activate velocity
part: select_begin
 21
part: select_end
variables: evaluate LineIntegral = IntegralLine(plist,velocity,[Y])
variables: evaluate FlowRate = LineIntegral*.017
tools: line OFF
part: modify_begin
part: visible OFF
part: modify_end
#
#Load data for Glottal Gap and Flowrate
query_ent_var: begin
query_ent_var: description
query_ent_var: query_type generated
query_ent_var: #_of_sample_pts 12000
query_ent_var: begin_simtime 0.000000e+00
query_ent_var: end_simtime 1.500e-01
query_ent_var: constrain min
query_ent_var: sample_by value
query_ent_var: variable_1 gap
query_ent_var: generate_over time
query_ent_var: variable_2 TIME
query_ent_var: end
query_ent_var: query

query_ent_var: begin
query_ent_var: description
query_ent_var: query_type generated
query_ent_var: #_of_sample_pts 12000
query_ent_var: begin_simtime 0.000000e+00
query_ent_var: end_simtime 1.500e-01
query_ent_var: constrain max
query_ent_var: sample_by value
```

```
query_ent_var: variable_1 FlowRate
query_ent_var: generate_over time
query_ent_var: variable_2 TIME
query_ent_var: end
query_ent_var: query
#
#Save Data Files for Glottal Gap and Flowrate
curve: select_begin
1
curve: select_end
curve: save xy_data FlowRate.txt

curve: select_begin
 0
curve: select_end
curve: save xy_data MinGlotGap.txt
#
#Create Animation
solution_time: begin_step 8000
anim_flipbook: begin_time_step 8000
anim_flipbook: end_time_step 12000
anim_flipbook: specify_time_as step
anim_flipbook: begin_simtime 1.000e-01
anim_flipbook: step_by 1.0000000e+01
anim_flipbook: load
anim_flipbook: play_forward
file: image_format avi
file: image_format_options Compression RAW BitRate 8000
anim_recorders: render_offscreen ON
file: image_numpasses 4
file: image_stereo current
file: image_screen_tiling 1 1
file: animation_file Animation
file: animation_window_size NTSC
file: animation_window_xy 704 480
file: animation_frames 400
file: animation_multiple_images OFF
file: animation_play_flipbook ON
file: animation_play_time OFF
file: animation_reset_flipbook ON
file: animation_reset_traces OFF
file: animation_reset_time OFF
file: save_animation
anim_flipbook: stop
```